MReadings: MR in RT

5th Edition ESTRO 2019

siemens.com/magnetom-world-rt

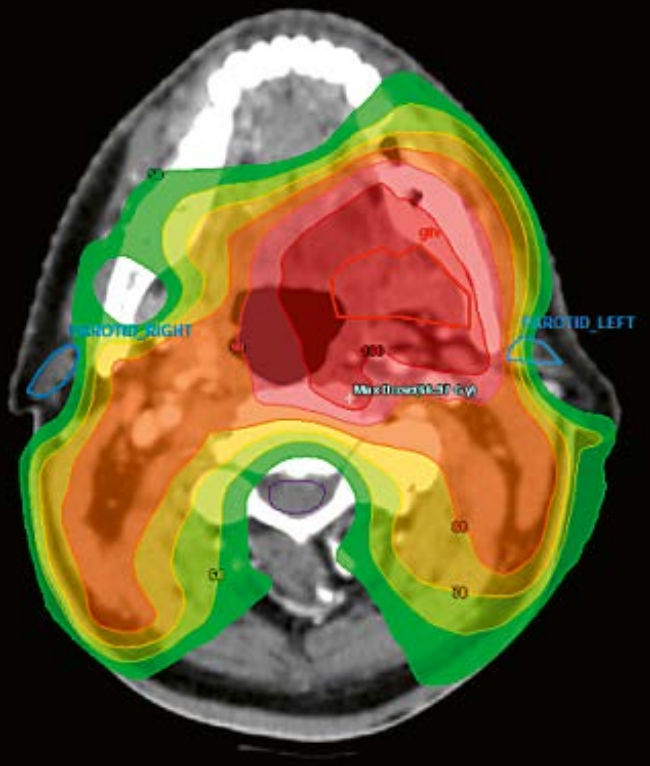

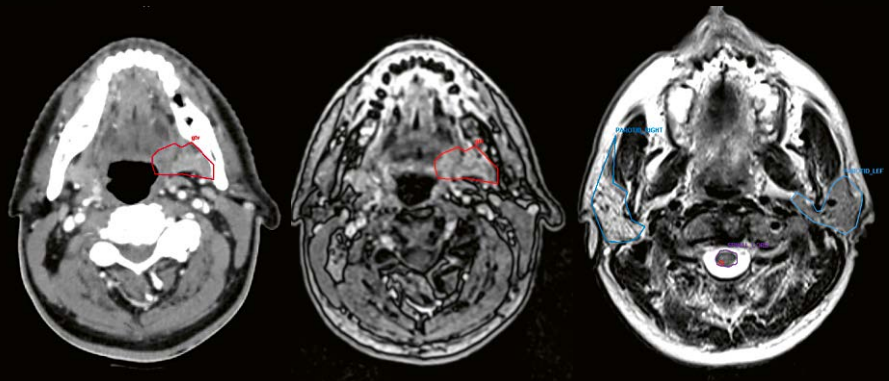

SIEMENS Healthineers

Professor Jürgen Debus, M.D., Ph.D. studied Medicine and Physics at the University of Heidelberg, Germany. Following residencies at the Germany Cancer Research Center (DKFZ) and at Massachusetts General Hospital in Boston, MA, USA, Debus held the position of attending and staff member in Radiation oncology at Heidelberg University. Between 1997 and 2003 he had a double appointment as head of the Department of Radiation Oncology, DKFZ and attending of the University hospital.

Since 2003 he is chairman of the Department of Radiation Oncology at the University Hospital Heidelberg.

Professor Debus has made interdisciplinary contributions to the development and clinical introduction of ion beam cancer therapy. His main focus is on the fields of clinical and experimental radiooncology, radiation medicine and nuclear medicine, where he has over 820 publications in peer-reviewed SCI-listed journals, 190 book contributions and is the editor of two textbooks.

MR-guided Radiotherapy: the Beginning of a New Era?

Over the last several decades, substantial technical innovations have paved the way for the delivery of highly precise and focused radiotherapy. These achievements can be primarily attributed to two sources: firstly, modern imaging technologies like computed tomography (CT), magnetic resonance (MR) imaging and positron emission tomography (PET) are increasingly incorporated in diagnostic evaluation and treatment planning, allowing for enhanced tumor delineation and secondly, the integration of imaging modalities directly into a linear accelerator have enabled daily monitoring of patient and tumor positioning as well as alterations in patient anatomy [1, 2].

Presently, CT-based image guidance has become standard-of-care, as CT imaging is routinely incorporated in nearly all radiotherapy units. However, low-dose CT imaging affords poor soft-tissue delineation and primarily allows for image guidance based on bony anatomy [3]. Conversely, MR offers excellent soft-tissue contrast allowing for precise target volume identification as well as monitoring of inter- and intrafractional changes in tumor positioning [4]. Given the technical challenges in integrating MR imaging into a linear accelerator, the first studies on MR-guided radiotherapy focused on offline solutions, with two different approaches proposed: either the patient was transported between the MRI and the linear accelerator or the MRI scanner was attached to rails on the ceiling to be moved out of the treatment room to ensure undisturbed operation of the linear accelerator [5–7]. At Heidelberg University Hospital and the German Cancer Research Center, we have prospectively treated patients with pelvic malignancies with offline, shuttle-based MR-guided radiotherapy and recently reported the efficacy, feasibility and patient compliance with this technique [8].

Nevertheless, all offline approaches are time-consuming effectively increasing the risk of intrafractional organ motion. Furthermore, the required patient re-positioning and associated positional inaccuracies challenge optimal radiotherapy delivery [6–8]. Naturally the radiation oncology community was eagerly awaiting the launch of the first hybrid machine incorporating a MRI scanner into the treatment delivery system [9]. Cobalt-60 teletherapy units were initially used for on-board MR imaging, but with recent advances and upgrades, linear accelerators are now increasingly utilized, with two hybrid devices currently available: the Viewray MRIdian Linac system (ViewRay, Oakwood Village, OH, USA), composed of a split-bore 0.35T MRI scanner, radiation gantry, and a 6 MV linear accelerator in the gap between the two magnet halves, and the Elekta MR-linac (Elekta AB, Stockholm, Sweden), composed of a 1.5T MRI scanner and a ring-based gantry containing a 7 MV standing wave linear accelerator [10–15].

The new MR-guided hybrid systems not only offer superior 3D imaging for precise tumor delineation as well as interfractional changes, but also provide 4D information via continuous monitoring of target volumes and surrounding critical structures for the treatment duration (cine MRI) [9, 13]. Compared to conventional radiotherapy techniques, safety margins and hence irradiated volume, can be decreased effectively reducing the risk of ensuing toxicity [12]. Encouraging initial results have been published for several tumor entities including pancreatic

carcinoma, early-stage low-risk breast cancer, and hepatic and adrenal metastases [16–19]. With some devices further offering gated dose delivery, neither the application of an internal target volume (ITV) nor invasive implantation of fiducial markers are needed for accurate motion management when using MR-guidance [9]. Respiratory gating and tumor tracking enable "real-time" anatomical feedback with the advantage of further reducing safety margins [20].

Beyond the aforementioned advances, the true potential of the new MR-guided hybrid devices lies in immediate, online adaptive treatment based on daily anatomical variation [18, 21]. MR-guided adaptive radiotherapy allows for the delivery of highly conformal treatments moulded to the current tumor position, enabling dose escalation to the primary target, with the potential for improved local control. Yet even without dose escalation, enhanced sparing of adjacent critical structures from dose spillage remains promising. Indeed, the initial studies identified primarily dosimetric advantages with online adaptation of MR-guided stereotactic radiotherapy of pancreatic, adrenal or ultracentral thoracic malignancies with additional clinical trial results highly awaited [16, 18, 22]. Radiation oncologists are now forced to reconsider the paradigms of total dose determination prior to treatment initiation and equal dose delivery for each fraction.

Beyond superior soft-tissue contrast, MRI also allows for incorporation of functional imaging, including non-invasive assessment of tissue perfusion, diffusion or cellular density [23, 24]. The potential availability of on-board 'functional' MRI sequences may allow for biologic, in addition to geometric, adaptation. For example, diffusion-weighted imaging (DWI) not only facilitates the identification of diffusion-altered tumor from surrounding healthy tissue, but also enables quantitative evaluation of suspicious lesions by using the apparent-diffusion coefficient (ADC), which correlates with cellularity and has been shown to be predictive for treatment responseto radiotherapy, as previously examined with rectal tumors [25, 26]. Hence, functional imaging might support early identification of nonresponders who may benefit from dose escalation. Future studies will answer whether daily on-board functional imaging is necessary or whether weekly offline imaging is sufficient for predicting treatment response. Currently, only 0.35T and 1.5T on-board MRI imaging is offered, misjudging the true potential of MR guidance. High-end diagnostic MRI scanner offer superior imaging quality for assessing tumor response and even potential treatment-related toxicity. A recent study illustrated the high benefit of 3T-MRI for predicting pathological treatment response following neoadjuvant radiochemotherapy for pancreatic cancer [27]. High-field or even ultra-high-field MRI further enables not only functional but also molecular imaging for even more precisely identifying tumor volumes, characterizing radioresistant tumor regions before radiation therapy and detecting recurrent disease following treatment [28]. Chemical exchange saturation transfer (CEST) MRI was recently reported to serve as a predictor of early progression in glioblastoma patients [29, 30].

A further highly promising scenario is MR-only planning bearing the potential of reducing not only radiation exposure as well as uncertainties introduced by CT-MRI registration but also additional work and costs. The major challenge for such an MR-only workflow is the development of so called pseudo-CT images for accurate dose calculation and planning. However, a number of techniques have been proposed for generating synthetic CTs from MRI data. Initial promising results for treatment planning of brain, prostate, head-and-neck, and pelvic tumors have already been published [31]. These studies illustrated that MR-only based radiotherapy might not only promise superior target delineation but also the potential for equivalent treatment planning. In future, the leading role of CT in radiotherapy might be replaced by MRI with its numerous advantages.

Despite the potential benefits of MR-guided radiotherapy, significant improvements are needed before widespread adoption and implementation. Available autosegmentation programs require significant manual adjustments, extending treatment times and increasing the risk of intrafractional motion; this is actually one reason why currently MR-guided radiotherapy primarily focus on hypofractionated stereotactic treatment of small lesions: due to the sharp dose gradient in stereotactic radiotherapy, re-contouring and re-optimization of daily plans can be quickly performed by only adapting those structures in close proximity to the target volume – a technique which can only partly be transferred to conventionally fractionated radiation of larger target volumes [11]. Furthermore, software tools for deformable dose accumulation are lacking, such as dose summation of different adapted fractions with varying organ and tumor volumes. Hence, the cumulative dose with dose maximum, minimum, and mean for every organ at risk cannot be provided, deterring any possibility of re-irradiation in the future.

Given that MR-guided adaptive radiotherapy requires significant time as well as an experienced team of professionals, clinical trials are needed to identify which patients will benefit most from adaptive treatment. However, direct comparisons between CT- and MR-guided adaptive radiotherapy using conventional fractionation may not accurately capture the true potential of MR-guided adaptive radiotherapy, given that MR-guided adaptive radiotherapy allows for high dose delivery under circumstances which would not otherwise be possible with conventional techniques [27].

Although there are many remaining challenges, MR-guided adaptive radiotherapy offers an unique chance for customized, daily individualized radiotherapy for further reducing side-effects in cancer therapy and improving tumor control and survival.

I hope you enjoy reading about the many new advances in MR in RT that we present to you in this magazine.

Jürgen Debus

Acknowledgment

I would like to thank PD Dr. Juliane Hörner-Rieber, who was instrumental in the preparation of this Editorial Comment.

References

1 Jaffray, D.A., Image-guided radiotherapy: from current concept to future perspectives. Nat Rev Clin Oncol, 2012. 9(12): p. 688-99.
2 Sterzing, F., et al., Image-Guided Radiotherapy. Dtsch Arztebl International, 2011. 108(16): p. 274-280.
3 Noel, C.E., et al., Comparison of onboard low-field magnetic resonance imaging versus onboard computed tomography for anatomy visualization in radiotherapy. Acta Oncol, 2015. 54(9): p. 1474-82.
4 Khoo, V.S. and D.L. Joon, New developments in MRI for target volume delineation in radiotherapy. Br J Radiol, 2006. 79 Spec No 1: p. S2-15.
5 Bostel, T., et al., MR-guidance – a clinical study to evaluate a shuttle- based MR-linac connection to provide MR-guided radiotherapy. Radiation Oncology, 2014. 9(1): p. 12.
6 Jaffray, D.A., et al., A Facility for Magnetic Resonance–Guided Radiation Therapy. Seminars in Radiation Oncology, 2014. 24(3): p. 193-195.
7 Karlsson, M., et al., Dedicated Magnetic Resonance Imaging in the Radiotherapy Clinic. International Journal of Radiation Oncology*Biology*Physics, 2009. 74(2): p. 644-651.
8 Bostel, T., et al., Prospective feasibility analysis of a novel off-line approach for MR-guided radiotherapy. Strahlentherapie und Onkologie, 2018. 194(5): p. 425-434.
9 Mutic, S. and J.F. Dempsey, The ViewRay System: Magnetic Resonance–Guided and Controlled Radiotherapy. Seminars in Radiation Oncology, 2014. 24(3): p. 196-199.
10 Acharya, S., et al., Online Magnetic Resonance Image Guided Adaptive Radiation Therapy: First Clinical Applications. Int J Radiat Oncol Biol Phys, 2016. 94(2): p. 394-403.
11 Bohoudi, O., et al., Fast and robust online adaptive planning in stereotactic MR-guided adaptive radiation therapy (SMART) for pancreatic cancer. Radiother Oncol, 2017. 125(3): p. 439-444.
12 Henke, L.E., et al., Magnetic Resonance Image-Guided Radiotherapy (MRIgRT): A 4.5-Year Clinical Experience. Clin Oncol (R Coll Radiol), 2018. 30(11): p. 720-727.
13 Raaymakers, B.W., et al., First patients treated with a 1.5 T MRI-Linac: clinical proof of concept of a high-precision, high-field MRI guided radiotherapy treatment. Phys Med Biol, 2017. 62(23): p. L41-L50.
14 VIEWRAY. VIEWRAY MRIdian MRI-guided Linac. 2019 [cited 2019 23.03.]; Available from: https://viewray.com/clinical-spotlight/scientific-presentations/.
15 Raaymakers, B.W., et al., Integrating a 1.5 T MRI scanner with a 6 MV accelerator: proof of concept. Phys Med Biol, 2009. 54(12): p. N229-37.
16 Bohoudi, O., et al., Identification of patients with locally advanced pancreatic cancer benefitting from plan adaptation in MR-guided radiation therapy. Radiotherapy and Oncology, 2019. 132: p. 16-22.
17 Acharya, S., et al., Magnetic Resonance Image Guided Radiation Therapy for External Beam Accelerated Partial-Breast Irradiation: Evaluation of Delivered Dose and Intrafractional Cavity Motion. Int J Radiat Oncol Biol Phys, 2016. 96(4): p. 785-792.
18 Palacios, M.A., et al., Role of Daily Plan Adaptation in MR-Guided Stereotactic Ablative Radiation Therapy for Adrenal Metastases. Int J Radiat Oncol Biol Phys, 2018. 102(2): p. 426-433.
19 Rosenberg, S.A., et al., A Multi-Institutional Experience of MR-Guided Liver Stereotactic Body Radiation Therapy. Advances in Radiation Oncology, 2019. 4(1): p. 142-149.
20 van Sörnsen de Koste, J.R., et al., MR-guided Gated Stereotactic Radiation Therapy Delivery for Lung, Adrenal, and Pancreatic Tumors: A Geometric Analysis. International Journal of Radiation Oncology*Biology*Physics, 2018. 102(4): p. 858-866.
21 Werensteijn-Honingh, A.M., et al., Feasibility of stereotactic radiotherapy using a 1.5T MR-linac: Multi-fraction treatment of pelvic lymph node oligometastases. Radiotherapy and Oncology, 2019. 134: p. 50-54.
22 Henke, L.E., et al., Stereotactic MR-Guided Online Adaptive Radiation Therapy (SMART) for Ultracentral Thorax Malignancies: Results of a Phase 1 Trial. Advances in Radiation Oncology, 2019. 4(1): p. 201-209.
23 Bonekamp, D., et al., Association of overall survival in patients with newly diagnosed glioblastoma with contrast-enhanced perfusion MRI: Comparison of intraindividually matched T1- and T2 (*)-based bolus techniques. J Magn Reson Imaging, 2015. 42(1): p. 87-96.
24 Donaldson, S.B., et al., Perfusion estimated with rapid dynamic contrast-enhanced magnetic resonance imaging correlates inversely with vascular endothelial growth factor expression and pimonidazole staining in head-and-neck cancer: a pilot study. Int J Radiat Oncol Biol Phys, 2011. 81(4): p. 1176-83.
25 Lambrecht, M., et al., Value of diffusion-weighted magnetic resonance imaging for prediction and early assessment of response to neoadjuvant radiochemotherapy in rectal cancer: preliminary results. Int J Radiat Oncol Biol Phys, 2012. 82(2): p. 863-70.
26 Surov, A., H.J. Meyer, and A. Wienke, Correlation between apparent diffusion coefficient (ADC) and cellularity is different in several tumors: a meta-analysis. Oncotarget, 2017. 8(35): p. 59492-59499.
27. Dalah, E., et al., Correlation of ADC With Pathological Treatment Response for Radiation Therapy of Pancreatic Cancer. Translational Oncology, 2018. 11(2): p. 391-398.
28 Jones, K.M., et al., Emerging Magnetic Resonance Imaging Technologies for Radiation Therapy Planning and Response Assessment. Int J Radiat Oncol Biol Phys, 2018. 101(5): p. 1046-1056.
29 Meissner, J.E., et al., Early Response Assessment of Glioma Patients to Definitive Chemoradiotherapy Using Chemical Exchange Saturation Transfer Imaging at 7 T. J Magn Reson Imaging, 2019.
30 Regnery, S., et al., Chemical exchange saturation transfer MRI serves as predictor of early progression in glioblastoma patients. Oncotarget, 2018. 9(47): p. 28772-28783.
31 Chandarana, H., et al., Emerging role of MRI in radiation therapy. J Magn Reson Imaging, 2018. 48(6): p. 1468-1478.
32 Hunt, A., et al., Adaptive Radiotherapy Enabled by MRI Guidance. Clinical Oncology, 2018. 30(11): p. 711-719.

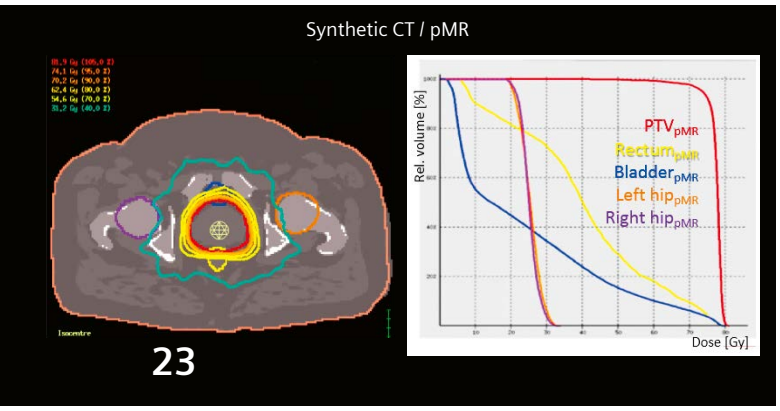

Synthetic CT Generation for the pelvic region based on Dixon-MR sequences

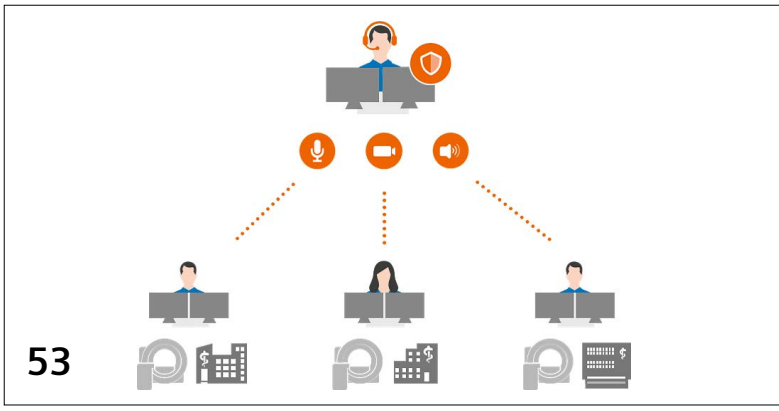

syngo Virtual Cockpit – remote scanning assistance and flexible workforce management

Editorial Comment

Radiation Therapy

Product News

Meet Siemens Healthineers

10 Years of Clinical Experience of MRI in Radiotherapy Treatment Planning: The Newcastle upon Tyne Story

Hazel McCallum, Ph.D.; Jonathan Wyatt, M.Sc.; Stephen Hedley, M.Sc.; Serena West, B.Sc.; Tim Dowling, B.Sc.; John Frew, F.R.C.R.; Rachel Pearson, F.R.C.R., Ph.D.; Christopher Walker, B.Sc

Northern Centre for Cancer Care, Newcastle upon Tyne Hospitals NHS Foundation Trust, Newcastle upon Tyne, UK

Introduction

The Northern Centre for Cancer Care installed its first MRI scanner dedicated for radiotherapy and oncology purposes in 2009, one of the first in the UK. Now with the hindsight of nearly ten years' experience, the evolution and development of MRI in radiotherapy planning in Newcastle upon Tyne will be described, from the first prostate patients planned with an MRI fused with a CT, extending to other treatment sites, to the first UK prostate patient to be treated with an MR-only pathway. In 2009, MRI was introduced as an important addition to the conventional CT planning process; it now forms an indispensable part of the radiotherapy service and paves the way for MR guided radiotherapy treatments with the introduction of MR-linacs.

Setting up the service

In 2007-08, when the hospital produced the specification for tender, there was only one wide-bore MRI scanner on the UK market, the Siemens MAGNETOM Espree 1.5T. An evaluation visit to Umea University Hospital, Sweden was a key influence, as the Newcastle team were able to observe an MRI scanner set-up for radiotherapy treatment planning, complete with laser bridge and in-house manufactured flat couch-top. Encouraged by the Umea University team, the purchase of a Siemens MAGNETOM 1.5T was confirmed in September 2008.

Multi-disciplinary collaboration was essential to the successful introduction of the service. Advice and guidance was provided by the Radiology Department throughout the planning, procurement installation and implementation stages. The appointment of an experienced MRI diagnostic radiographer was key, as their experience of sequence development as well as patient and staff safety provided some security in the early implementation phases.

Technical preparation

Commissioning for radiotherapy treatment planning
In 2009, there was little published data on performance standards for an MRI scanner for radiotherapy purposes. The radiotherapy department had access to a set of MagNet MRI QC phantoms, no longer commercially available and a large field of view geometric distortion phantom designed and built in Newcastle University [1].

An Evaluation Report on the Siemens MAGNETOM Espree, published by the NHS Purchasing and Supply Agency was used for much of the QC development and initial performance tolerances. Extensive experience of commissioning CT scanners and treatment imaging modalities was relied upon to develop additional tests which would consider radiotherapy aspects such as detailed geometric accuracy testing.

MRI commissioning tests

- Laser positional accuracy
- Couch level and scaling
- MRI compatibility of Immobilization devices
- Image quality
- Large FOV geometric distortion
- Geometric slice position and width
- Data transfer inter-operability
- Image fusion accuracy

MRI RT planning specific equipment
At the inception of our clinical service, there was no commercially available compatible flat couch top. We entered into a research collaboration with MediBord, Nottingham, UK to develop a bespoke flat couch top to fit with our scanner model and our preferred patient set-up. The couch top material is glass fibre which means the couch top is

extremely light, at less than 4 kg, and easy to maneuver. This is particularly important when the radiotherapy couch top needs to be replaced by the diagnostic couch top for clinical trials patient scanning or diagnostic scans for radiotherapy patients. The couch-top securing mechanism was designed to fit into the coil strap fittings on the Siemens MAGNETOM couch. The flat couch top was designed by NCCC staff and manufactured by Medibord. Figure 1 shows details of the couch top.

When acquiring diagnostic MR images, typically the surface coils are directly wrapped around the patient. This can compress the patient's skin, which is not appropriate for radiotherapy planning where an accurate image of the patient's external contour is essential.

To avoid any distortion of the patient skin contour, coil supports for pelvis and head and neck were designed and manufactured in-house by the Mechanical Workshop, Northern Medical Physics and Clinical Engineering. The pelvis coil support secures in position in the coil strap fittings, is manufactured from polyethylene terephthalate glycol (PTEG) and polyvinyl chloride (PVC) and is adjustable to suit a range of patient sizes. Hook and loop fastening is fixed to the PTEG surface to assist with securing the coils onto the support. The coil support for pelvic imaging is shown in figure 2.

The head and neck coil support is manufactured from PTEG and secured onto an in-house manufactured MRI compatible head board (Fig. 3).

1 **(1A)** Medibord RT flat couch top **(1B)** access to head coil fixtures **(1C)** retaining access to coil securing fixtures and utilizing these fixtures for securing the couch top in position.

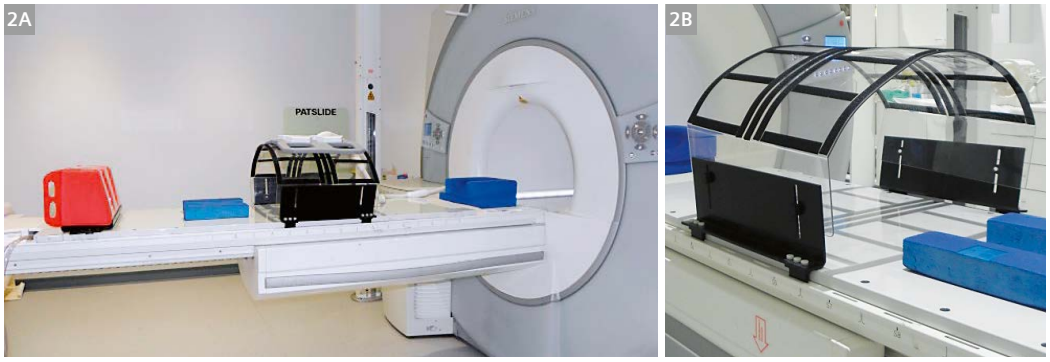

2 **(2A)** In-house manufactured coils support for pelvis imaging **(2B)** showing the couch securing mechanism and adjustable size.

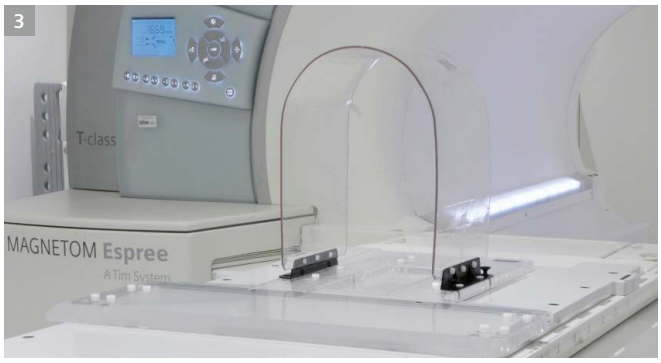

3 In-house manufactured coils support for brain and head and neck imaging.

MRI safety

From the outset, it was clear that education and adjustment was needed to safely introduce an MRI Suite in the center of a clinical radiotherapy treatment center. Considerations for access management to the MRI control area, were new concepts for radiotherapy staff who were more familiar with the model that any hazard was removed when the power was switched off. Management of projectile hazards was also of concern. The MRI Suite control room door is key-coded to enable controlled access to the MRI control room and so to the MRI examination room. Early incidents of wiped credit cards and stopped watches served to underline the new working practices required.

Clinical preparation

Development of radiotherapy specific MRI protocols was based heavily on those developed in Umea University, who provided extensive informal mentoring support in the set-up of our service.

Prostate

The first patient cohort to receive MRI RT planning acquisitions was prostate patients. Two acquisition sequences were used: a 3D T2-weighted Sampling Perfection with Application optimized Contrasts using different flip angle Evolution (SPACE) sequence which was optimized to image the entire patient outline with a small voxel size (1.2 x 1.2 x 1.7 mm^3) and a high bandwidth to minimize geometric distortion, and a small FOV T2-weighted Turbo Spin Echo (TSE) sequence. The SPACE sequences has since been further optimized and the TSE sequence replaced with a Multi-Echo Data Image Contribution (MEDIC) sequence which is acquired over a smaller field of view to assist with the definition of the in-slice boundary of the prostate capsule.

A typical patient set-up is shown in figure 4, with details of the current acquisition protocols.

4 Typical patient set-up for prostate MRI acquisition and MRI acquisition parameters.

Prostate delineation protocols were developed with the help of Radiologist input. This inter-disciplinary team identified a difference in imaging task between diagnosis and delineation.

The experience of a radiologist identified the regions of disease within the prostate, but did not need to identify the boundary of the prostate gland, whereas a clinical oncologist needs to accurately delineate the boundary of the prostate gland. Cross disciplinary learning produced guidelines on prostate delineation based on MRI when fused with a planning CT. Methods of managing differences in patient anatomy between the MRI and CT scanning sessions were developed. There are inevitable patient set-up differences, both in posture and internal anatomy position. Rigid registration can take account of postural differences, but cannot completely compensate for differences in internal anatomy caused by changes in bowel and bladder filling. As the CT scan is used as the basis of the treatment plan and the reference image set for image guided radiotherapy, any differences in anatomy between CT and MRI tend to be compensated for by reverting to the CT anatomy as the gold standard. This inevitably compromises the added benefit of the MRI acquisition and results in an 'MRI guided CT delineation' for prostate GTV with OARs delineated on the CT scan. This means that the excellent MRI soft tissue image quality is not always able to be used to its full potential, providing experiential evidence of the benefit of an MR-only patient pathway. A typical CT-MRI image registration for a prostate patient, and the resultant dose distribution are shown in figure 5.

The clinical service was quickly extended to gynecological EBRT sites in January 2010. It was found that the same T2 3D SPACE acquisition protocol was suitable for cervix and uterus visualization. The acquisition sequences have now further developed and include two 2D sequences to assist with delineation, as shown in Table 1.

Sequence name	SPACE tse_vfl	MEDIC
Echo time	211 ms	22 ms
Repetition time	1500 ms	674 ms
Flip angle	150°	28°
Bandwidth	601 Hz/px	190 Hz/px
Orientation	Axial	Axial
Dimension	3D	2D
Field of View	450 x 447.3 mm^2	260 x 260 mm^2
Number of slices	120	34
Voxel size	1.4 x 1.4 x 1.5 mm^3	1.3 x 1.0 x 3.0 mm^3

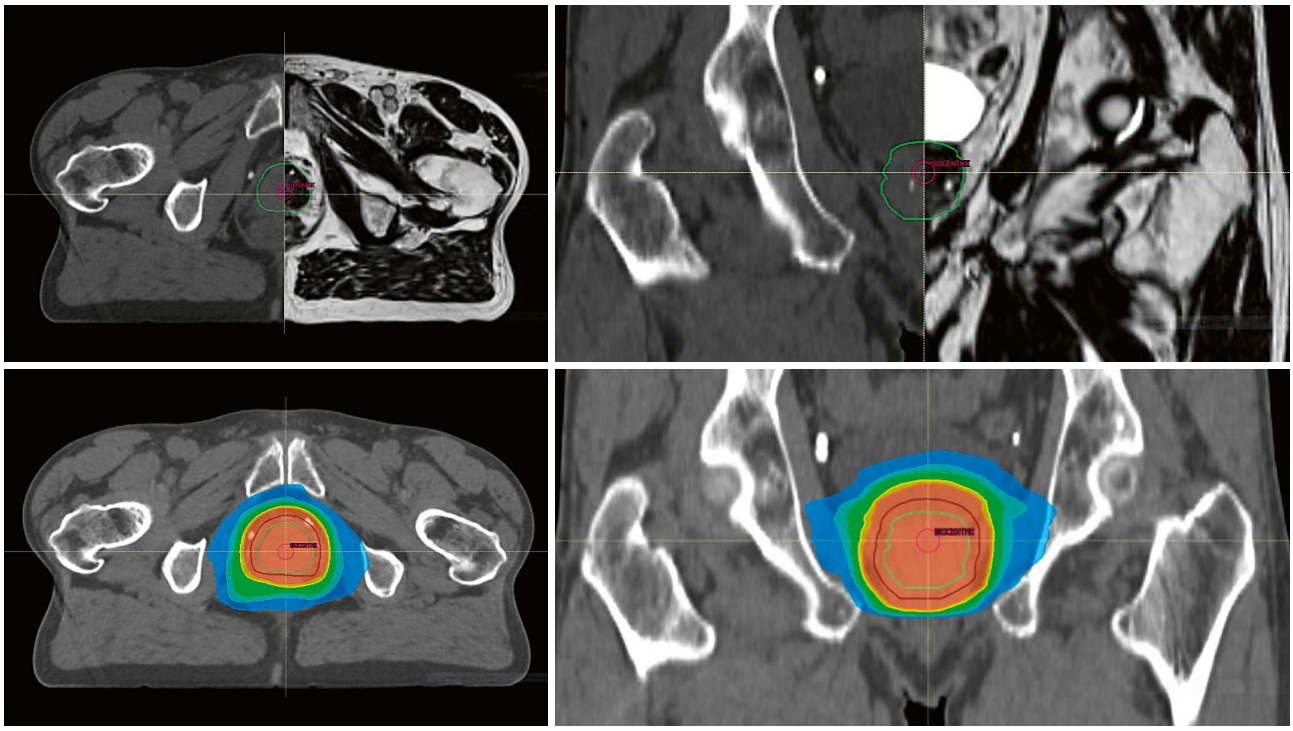

5 CT-MRI image fusion with delineation and VMAT dose distribution.

Sequence name	SPACE tse_vfl	TSE	TSE
Echo time	165 ms	102 ms	101 ms
Repetition time	2000 ms	9840 ms	6300 ms
Flip angle	150°	150°	150°
Bandwidth	651 Hz/px	140 Hz/px	150 Hz/px
Orientation	Axial	Sagittal	Axial
Dimension	3D	2D	2D
Field of View	320 x 320 mm^2	290 x 280 mm^2	260 x 260 mm^2
Number of slices	144	28	45
Voxel size	1.3 x 1.3 x 1.5 mm^3	1.1 x 1.1 x 4.0 mm^3	1.0 x 1.0 x 4.0 mm^3

Table 1: MRI acquisitions for treatment planning of gynecological tumors.

Brain

MRI imaging for selected brain tumors was introduced in January 2011. Patients are scanned without the immobilization device so that the head coil can be used.

A T1 axial 3D sequence is used for delineation of the GTV. Typical patient images and the MRI sequence parameters are shown in figure 6.

Head and neck

The introduction of MRI imaging for oro and hypopharyngeal tumors began in April 2011. Two sequences were developed to assist with GTV delineation and nodal and organ at risk delineation. A T1 VIBE post contrast acquisition was used to delineate GTV and a T2 sequence to delineate lymph nodes and organs at risk. Figure 7, shows a typical patient set-up and coil arrangement utilizing the in-house manufactured coil support. A second flex coil may be positioned over the patient's shoulders if required. The MRI acquisition parameters are also shown in figure 7 and typical patient images and dose distribution shown in figure 8.

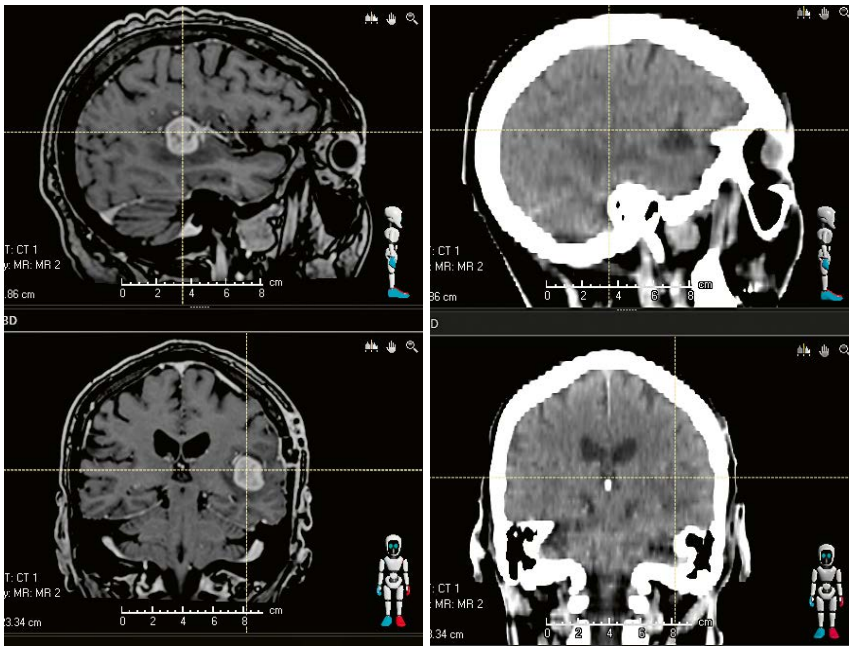

Sequence name	fl3d_vibe
Echo time	2.39 ms
Repetition time	9.00 ms
Flip angle	12°
Bandwidth	210 Hz/px
Orientation	Axial
Dimension	3D
Field of View	250 x 250 mm²
Number of slices	192
Voxel size	1.1 x 1.0 x 1.0 mm³

6 Soft tissue detail on MRI [LHS] and CT [Center] with MRI parameters shown on RHS.

7 A typical head and neck coil arrangement and MRI acquisition parameters.

Sequence name	fl3d_vibe	TSE
Echo time	2.39 ms	89 ms
Repetition time	9.00 ms	6000 ms
Flip angle	12°	150°
Bandwidth	210 Hz/px	159 Hz/px
Orientation	Axial	Axial
Dimension	3D	2D
Field of View	250 x 250 mm²	310 x 271.25 mm²
Number of slices	224	70
Voxel size	1.1 x 1.0 x 1.0 mm³	1.1 x 0.8 x 3.0 mm³

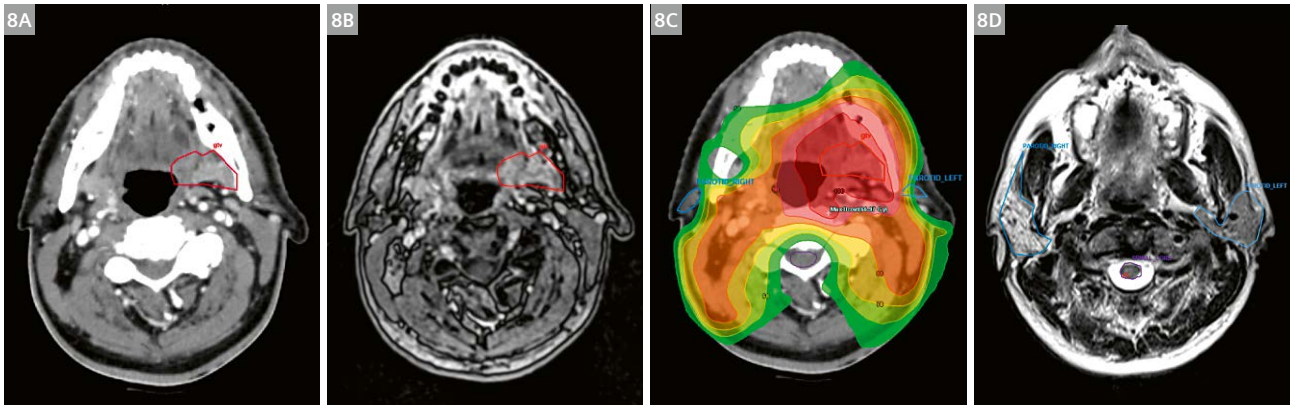

8 Typical image set **(8A)** CT, **(8B)** T1w VIBE **(8C)** dose distribution **(8D)** T2w TSE.

Rectum

Routine MR imaging for rectal cancer patients was introduced in April 2018. With MRI planning scans for anus patients then following in September, 2018. Patient set-up is similar to that for prostate patients.

The MRI acquisition parameters are shown for rectum patients in Table 2 and for anus patients in Table 3. A typical example of CT-MRI image registration for planning of a rectal cancer is shown in figure 9.

Sequence name	SPACE tse_vfl	TSE	TSE
Echo time	211 ms	102 ms	101 ms
Repetition time	1500 ms	9840 ms	6300 ms
Flip angle	150°	150°	150°
Bandwidth	601 Hz/px	140 Hz/px	150 Hz/px
Orientation	Axial	Sagittal	Axial
Dimension	3D	2D	2D
Field of View	450 x 447.3 mm^2	280 x 280 mm^2	260 x 260 mm^2
Number of slices	144	28	45
Voxel size	1.4 x 1.4 x 1.5 mm^3	1.1 x 1.1 x 4.0 mm^3	1.0 x 1.0 x 4.0 mm^3

Table 2: MRI acquisitions for treatment planning of rectal tumors.

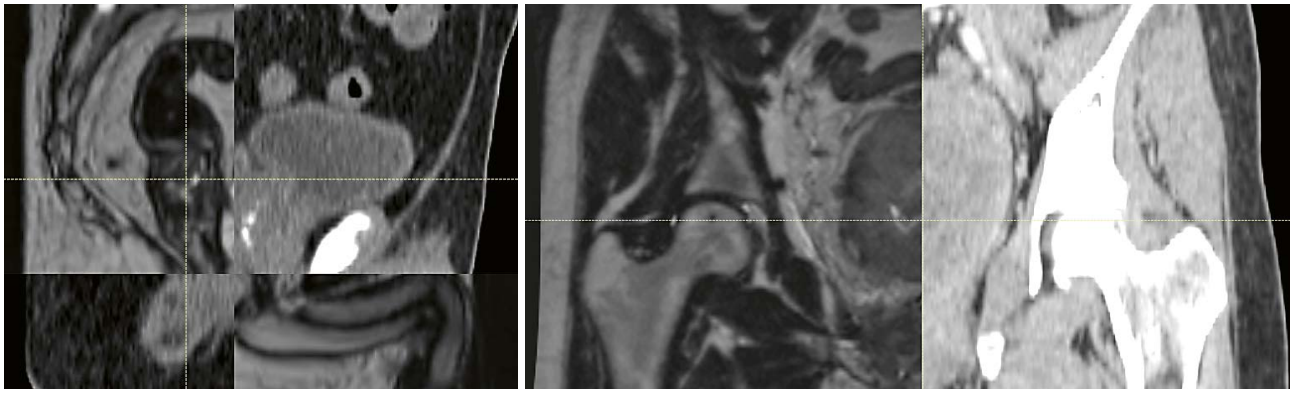

9 MRI-CT fusion for rectum and anus.

Sequence name	SPACE tse_vfl	TSE	TSE
Echo time	165 ms	102 ms	101 ms
Repetition time	2000 ms	9840 ms	6300 ms
Flip angle	150°	150°	150°
Bandwidth	651 Hz/px	140 Hz/px	150 Hz/px
Orientation	Axial	Sagittal	Axial
Dimension	3D	2D	2D
Field of View	320 x 320 mm^2	280 x 280 mm^2	260 x 260 mm^2
Number of slices	144	28	45
Voxel size	1.3 x 1.3 x 1.5 mm^3	1.1 x 1.1 x 4.0 mm^3	1.0 x 1.0 x 4.0 mm^3

Table 3: MRI acquisitions for treatment planning of anal tumors.

SRS Brain

Newcastle is one of 17 Cancer Centers in England commissioned by NHS England to deliver Stereotactic RadioSurgery (SRS) and has been treating SRS patients since June 2015. Rapid access to planning MRI scans is essential to delivery of this service, particularly for patients travelling large distances. A range of MRI sequences are acquired, often tailored to the specific clinical presentation and vitally supported by neuroradiologists. Figure 10 shows a range of SRS brain tumors with the MRI acquisition image and the treatment dose distribution.

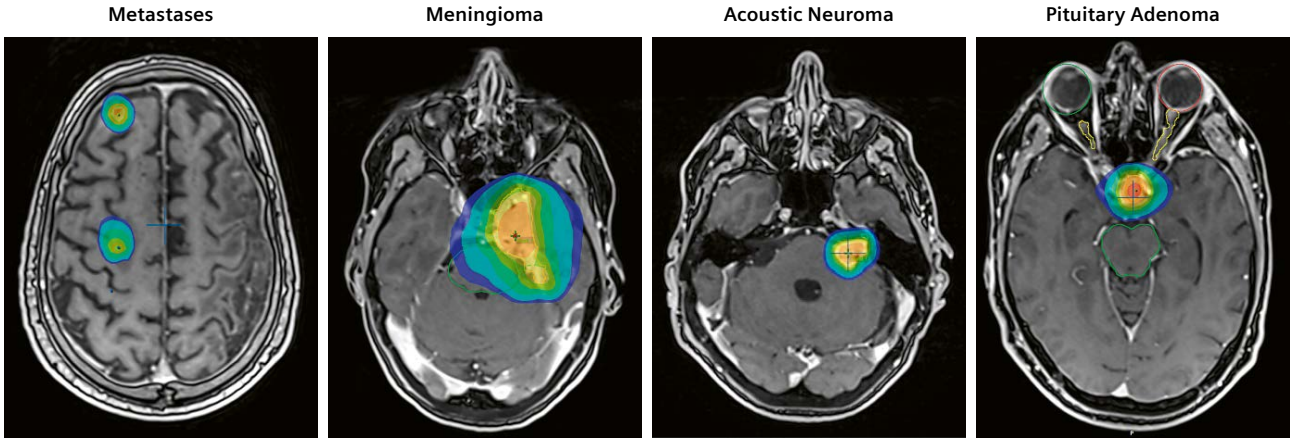

10 SRS brain treatments showing a range of treatment sites with the dose distribution.

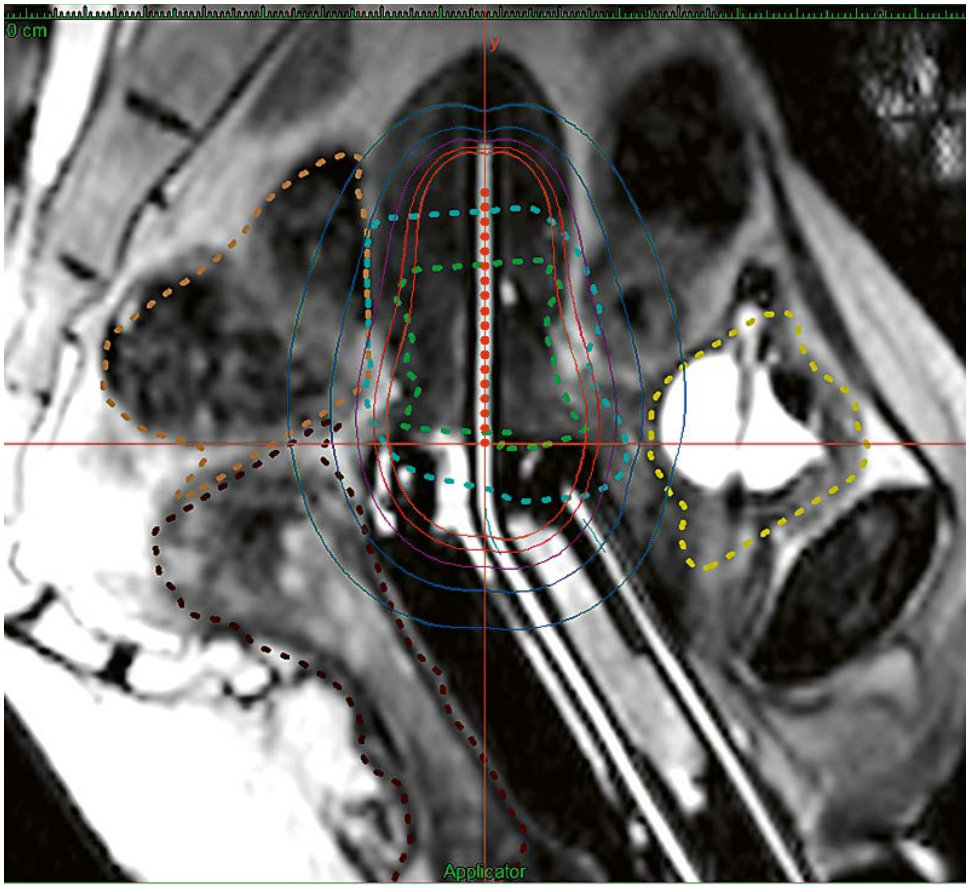

11 MRI planning image showing a cervical ring brachytherapy treatment. The dashed lines show the clinical delineations and the solid lines the brachytherapy dose distribution.

Brachytherapy
MRI acquisitions for brachytherapy post-planning for prostate I-125 implants began in February 2010, with MRI-only planning for cervix brachytherapy being implemented in September, 2011. MRI-only planning for vaginal vault brachytherapy treatments was introduced in July, 2012 when MRI was also introduced as a position check for vaginal vault applicator insertions for patients with intermediate and high risk endometrial cancer. Figure 11 shows a brachytherapy treatment for cervical cancer.

MRI-only planning
Our growing experience in CT-MR fusion for radiotherapy delineations emphasized the compromises that were necessary to account for differences in patient position and preparation between the CT and MRI imaging sessions. This was resulting in a limitation of the benefit of MRI as the CT image set was used as the standard where there were anatomical discrepancies between the CT and MRI. Feedback from Clinical Oncologists described increasing frustration at the compromises that were being imposed by limitations in the technique. NCCC has been investigating the technical development of an MR-only patient pathway since 2016 with research partners in Australia, UK and Sweden. Conventional CT-MR based radiotherapy planning utilizes the superior soft tissue provided by the MRI for target and OAR delineation, and the CT image to account for different types of tissue in the dose calculation. An MR-only pathway requires an appropriate dataset for dose calculation, a synthetic CT, and the NCCC research group have investigated the accuracy of available algorithms [2].

MR also suffers from geometric distortion, which is of some concern in radiotherapy planning image sets. A dedicated large field of view distortion phantom and automated analysis software was evaluated [3] and is now used in monthly quality assurance. Radiotherapy specific Quality Control programmes have been developed to ensure adequate geometric fidelity and demonstrate consistent performance of the clinical MR scanner. MR-only pathways are available in some European radiotherapy centers using X-ray IGRT treatment machines, but there is an important difference in the treatment pathway between these centers and NCCC. Prior to radiotherapy treatment being delivered at each visit, an imaging session is performed on the treatment machine to ensure that the patient is set-up and aligned as accurately as possible. In the existing clinical centers in Europe, this is achieved using fiducial markers, whereas image matching using soft tissue anatomy is used in Newcastle, sparing the patient the procedure required to insert fiducial markers. This means that the MRI image used to develop the treatment plan can be used as a reference image for the on-treatment image verification.

Our research experience coupled with our clinical experience means we felt confident in making the step from research to routine for MR-only planning for prostate patients. Our first MR-only prostate patients were treated in January 2019. Figure 12 shows the clinical dose distribution on the synthetic CT and the dose difference between the clinical plan and the QA plan calculated on the back-up CT.

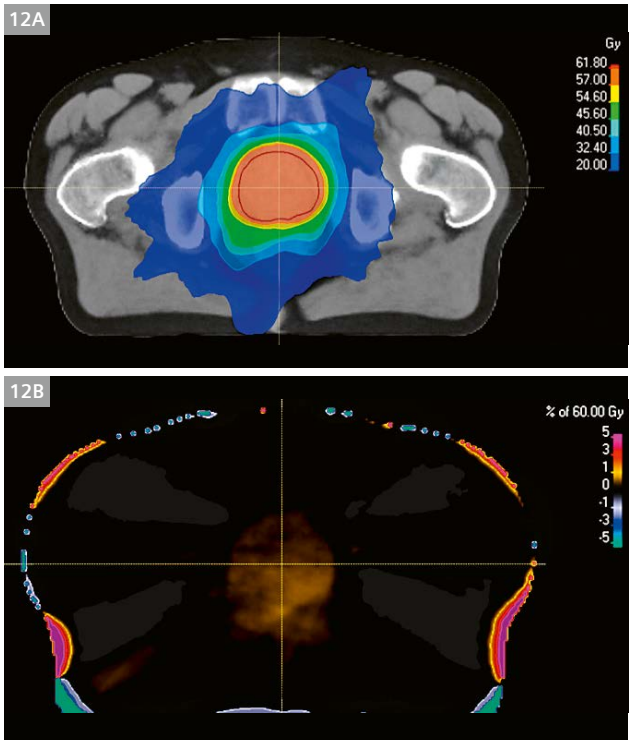

12 First MR-only prostate patient – dose distribution **(12A)** and dose difference to CT **(12B)**.

Planning for the future

As the replacement date of our radiotherapy MRI approached, MR acquisition activity was not enough to justify a second purchase and it was important to capture the clinical opinion of the role of MR in radiotherapy planning. A survey of Consultant Clinical Oncologists in NCCC was performed where participants were asked to score a range of statements on a five point scale for the treatment sites which were routine at the time of the survey [4]. The five point scale is shown on the next page.

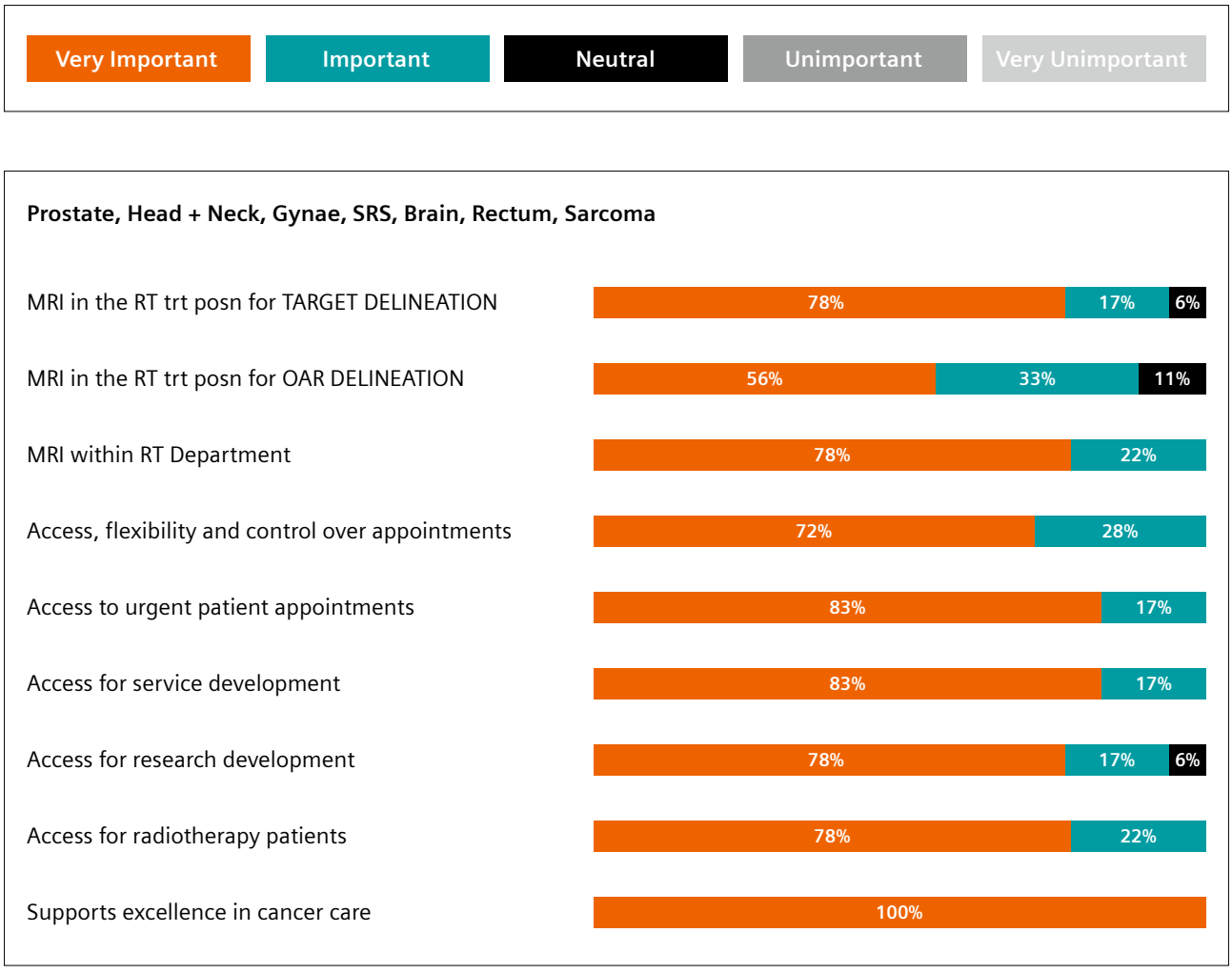

13 Responses for external beam treatment sites where a planning MRI is acquired.

The response rate was 73% and figure 13 shows the results for external beam treatment sites which include a planning MRI.

The survey showed an overwhelmingly positive response for sites which currently receive planning MRI scans. When asked how important it as to acquire MRI scans in the treatment position for target and OAR delineation, no ***Unimportant*** or ***Very Unimportant*** responses were received. The ***Neutral*** responses referred to Brain cases, where it was felt that although MRI is ***Very Important***, the patient position is less so, as rigid registration within the skull offers clinically acceptable results. There was also very strong support for the planning MRI scanner to be located within the radiotherapy department.

Summary

NCCC were one of the first UK cancer centers to install a dedicated MRI scanner for radiotherapy planning, in 2009. The clinical workload and clinical scope has significantly increased over the first 10 years so that over 35% of radical patients in Newcastle now receive an MRI to improve their planning pathway. Practices and equipment have developed greatly over the past ten years and manufacturers now offer commercial coil bridges and supports, however our experience with in-house developments may be useful on further developing commercial products. There was overwhelming clinical support to replace our radiotherapy MRI scanner and we are now looking forward to extending our MR-only pathway for prostate patients to other treatment sites, cementing MRI as indispensable to the radiotherapy pathway. The image (right) shows the NCCC MR in RT Team.

Acknowledgments

The authors would like to acknowledge the contribution of Jill McKenna to the development and introduction of the NCCC MRI service.

References

1 EC Harron, MJ Firbank, J McKenna, HM McCallum R Mohanraj. Evaluation of MRI distortion correction for use in radiotherapy treatment planning. Clinical Oncology 23(3), 2011.
2 Jonathan Wyatt, Jason A Dowling, Charles G Kelly, Jill McKenna, Emily Johnstone, Richard Speight, Ann Henry, Peter B Greer and Hazel M McCallum. Investigating the generalisation of an atlas-based synthetic-CT algorithm to another center and MR scanner for prostate MR-only radiotherapy. Physics in Medicine and Biology, 62(24), 2017.
3 Jonathan Wyatt, Stephen Hedley, Emily Johnstone, Richard Speight, Charles Kelly, Ann Henry, Susan Short, Louise Murray, David Sebag-Montefiore, Hazel McCallum. Evaluating the repeatability and set-up sensitivity of a large field of view distortion phantom and software for magnetic resonance-only radiotherapy. Physics and Imaging in Radiation Oncology, 6, 2018.
4 HM McCallum, JJ Wyatt, J McKenna, CG Kelly, CP Walker. A compelling case for MRI in RT? The Newcastle experience. Poster presentation at Institute of Physics and Engineering in Medicine: MR in the planning, delivery and monitoring of radiotherapy conference, Edinburgh, March 2017.

Contact

Dr. H. M. McCallum
Consultant Clinical Scientist
Radiotherapy Physics
Northern Centre for Cancer Care,
Freeman Hospital
Newcastle upon Tyne, NE7 7DN
UK
Tel.: +44 (0)191 213 8112
hazel.mccallum@nuth.nhs.uk

Dr. Rachel Pearson
Consultant Clinical Scientist
Radiotherapy Physics
Northern Centre for Cancer Care,
Freeman Hospital
Newcastle upon Tyne, NE7 7DN
UK
Tel.: +44 (0)191 213 8521
rachel.pearson@nuth.nhs.uk

The NCCC MRI Team [left to right] **Timothy Dowling** and **Steve Harris**, Senior MRI Imaging Radiographers; **Rachel Pearson**, Consultant Clinical Oncologist; **Rachel Brooks**, Research and Development Clinical Specialist Radiographer; **Iraje Ahmed**, MRI Imaging Radiographer; **Elizabeth Raven**, Superintendent Treat-'ment Radiographer; **Hazel McCallum**, Consultant Clinical Scientist; **Karen Pilling**, Clinical Lead Superintendent Radiographer; **Serena West**, Imaging Superintendent Radiographer; **Jonathan Wyatt**, Clinical Scientist.

The Importance of Collaboration between Clinical Radiology and Radiation Oncology in the Era of Precision Radiation Therapy

Amish Lakhani, MBBS MA (Cantab) FRCR[1]; Yat Man Tsang, BSc MSc PhD[2]; Roberto Alonzi, BSc MBBS MRCP FRCR MD[3]; Anwar R. Padhani, MBBS FRCP FRCR[1]

[1]Consultant Radiologist, Paul Strickland Scanner Centre, Mount Vernon Hospital, Northwood, Middlesex, UK
[2]Consultant Radiographer – Specialised Service Delivery, Mount Vernon Hospital, Northwood, Middlesex, UK
[3]Consultant Clinical Oncologist, Mount Vernon Hospital, Northwood, Middlesex, UK

Introduction

Radiation therapy is an essential component in the management of many cancer patients. It can be used for primary treatment, local control, and palliation in over 50% of cancer patients [1]. Radiation therapy has been shown to be an integral part of the treatment regime in 40% of patients who are cured of cancer, therefore making this treatment modality extremely cost-effective [2].

Key to the success of radiation therapy is the ability of the radiation oncologist to accurately delineate the tumor to maximize delivery of the radiation dose to the cancer whilst minimizing dose toxicity to the adjacent normal tissues. This has become increasingly possible with technological advances in highly conformal radiation therapy delivery methods such as intensity-modulated radiotherapy (IMRT) and stereotactic body radiation therapy (SBRT). Paralleling the advances in radiotherapy delivery methods are the technological advances in imaging with the development of next-generation techniques such as magnetic resonance imaging (MRI) with quantitative functional biomarkers, and positron emission tomography/computed tomography (PET/CT) with novel tracers. These advances in imaging have improved the sensitivity and specificity of identifying tumor location and extent [3]. In this article we highlight examples of these advancements and demonstrate how collaboration between the clinical radiology and radiation oncology departments enhances treatment effectiveness.

Imaging in the cancer patient's pathway

Imaging is an integral component in almost every step of the cancer patient's pathway from detection and localization of cancer all the way to monitoring for recurrence once treatment is completed (Fig. 1). Using prostate cancer as an example, we will demonstrate how technological advancements in imaging are able to image the tumor microenvironment and normal tissues, and how we can use this to aid accurate and successful radiation treatments.

Multiparametric MRI (mpMRI) of the prostate is now routinely used in patients with suspected prostate cancer [4]. With mpMRI we can utilize multiple MRI sequences to depict different biological properties: Morphological T1 and

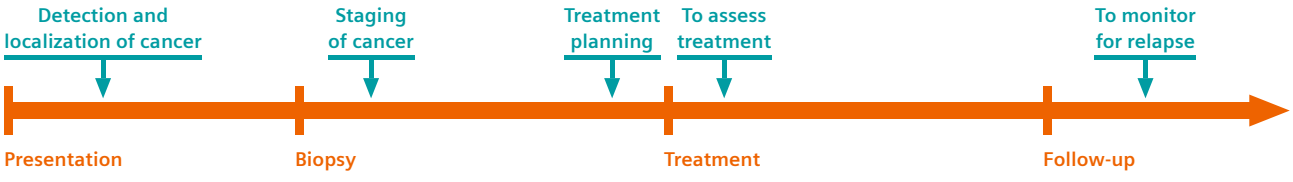

1 Imaging (green arrows) is integral throughout the cancer patient's pathway (orange arrow).

T2-weighted sequences give us information on anatomy; diffusion-weighted imaging (DWI) informs us of cellular density and necrosis; spectroscopy identifies cell proliferation and replacement of normal glandular tissues; and dynamic contrast enhancement (DCE) gives us information on perfusion and vascular permeability. Utilizing these properties it is possible to accurately detect, localize, and locally stage prostate cancer. mpMRI is also important to guide and/or direct biopsy via fusion techniques, and MRI may also be used to perform an in-bore biopsy if required.

If a patient is diagnosed with prostate cancer localized to the pelvis, pelvic radiotherapy may be a suitable treatment option even in the presence of oligometastases. Even though mpMRI has been shown to yield high detection rates of clinically significant prostate cancer (csPC) [5], multiple studies have shown it can underestimate the volume and extent of intra-prostatic disease in patients with known prostate cancer [6]. This is why it is important to include the entire prostate gland in the gross tumor volume (GTV) when planning radiotherapy. However, we can also utilize the confidence of mpMRI in identifying the more aggressive index lesions which can be given a focal boost of radiation treatment (Fig. 2). In this example, the mpMRI clearly shows the dominant right-sided index lesion on the anatomical and DWI, allowing this patient to undergo biologically optimized radiotherapy; the planning computer optimization software was programmed to maximize the radiation dose to the dominant index lesion with a focal boost, and to limit the dose to the rest of the gland to a defined ceiling.

In another case example (Fig. 3), following a multi-disciplinary team (MDT) discussion, it was decided that a patient with organ-confined prostate cancer would be treated with highly conformal SBRT. At the MDT, the reporting radiologist described the prostate volume, index lesion location, and confirmed that the tumor was organ-confined. The radiation oncologist chose the optimal treatment plan. It is important for the radiologist to carefully assess the risk of gross extra-prostatic extension of tumor. Whilst the tumor may seem organ-confined, if there is increased tumor-capsule contact length, there is an increasing risk of microscopic extra-prostatic extension [7]. In fact, 20–50% of clinically organ-confined tumors ultimately have extra-prostatic extension (usually microscopic) at prostatectomy [8]. If this is a concern and the radiation oncologist is made aware, treatment margins at the site of the tumor can be extended and treatment margins elsewhere around the gland can be tighter, thereby helping to minimize potential side effects of including adjacent normal tissues in the radiotherapy field. An interventional radiologist inserted fiducial markers to aid with dynamic target tracking. Imaging with MRI was again subsequently employed to visualize the fiducial markers and prostate outline after insertion for radiotherapy planning purposes.

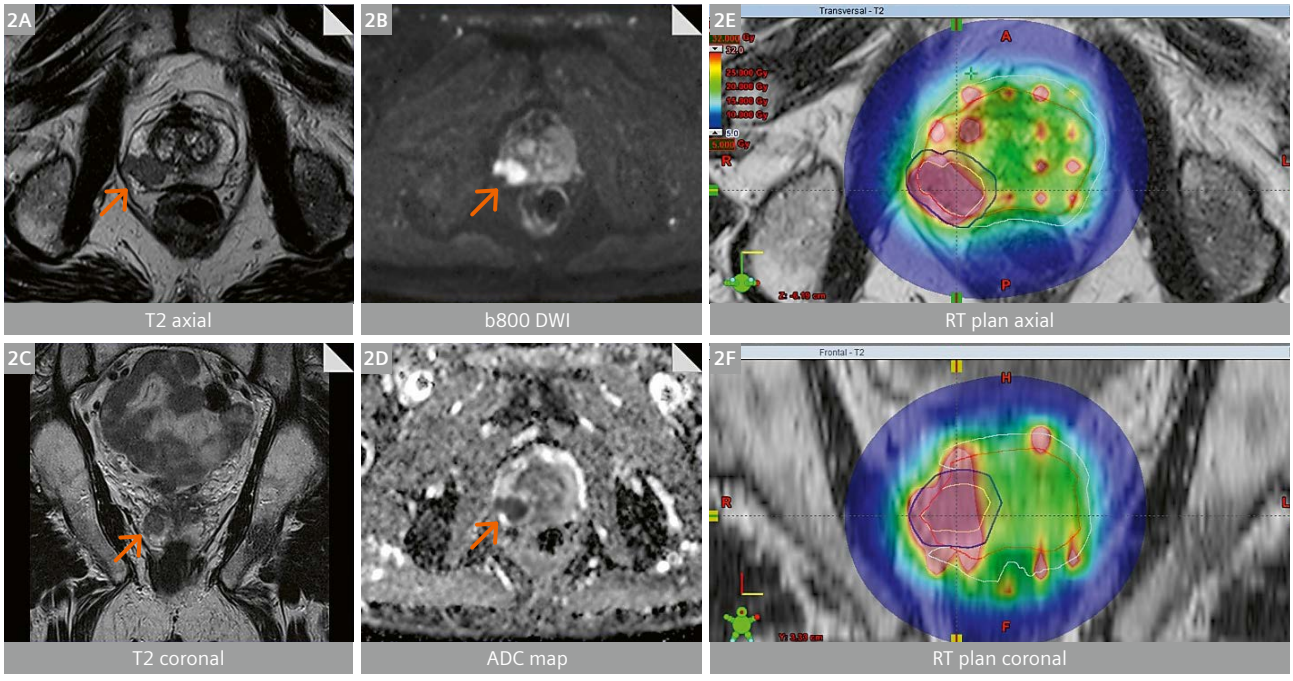

2 A 75-year-old man with raised PSA (18 ng/mL). Imaging with mpMRI **(2A-D)** and bone scan found a suspicious prostatic lesion in the right peripheral zone (arrows) with staging of T3a N0 M0 (extra-prostatic extension but no involved lymph nodes or distant sites of metastatic disease). The patient underwent an MR-directed and systematic biopsy which showed 5/12 positive biopsies (all right-sided) with a maximum Gleason score of 4+3. Brachytherapy catheters were inserted under general anesthetic and the patient received high-dose brachytherapy to the entire gland with a focal boost to the dominant right-sided index lesion **(2E, F)**.

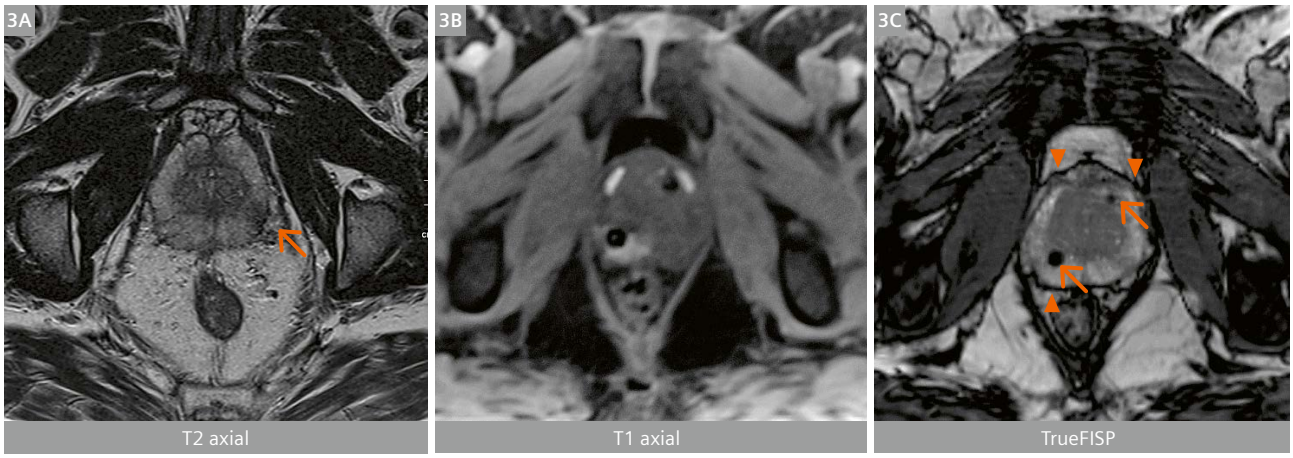

3 A 62-year-old man with raised PSA (9 ng/mL) underwent an mpMRI which demonstrated organ-confined index lesion (arrow) in the left peripheral zone **(3A)**. The patient was discussed at the MDT, and SBRT was decided. Fiducial markers were inserted by an interventional radiologist, and a radiotherapy planning MRI was performed. T1-weighted axial imaging **(3B)** showed hemorrhage post fiducial marker insertion, and a TrueFISP sequence **(3C)** clearly delineates the prostatic outline (arrowheads) and the location of the fiducial markers (arrows) to aid with radiation treatment planning.

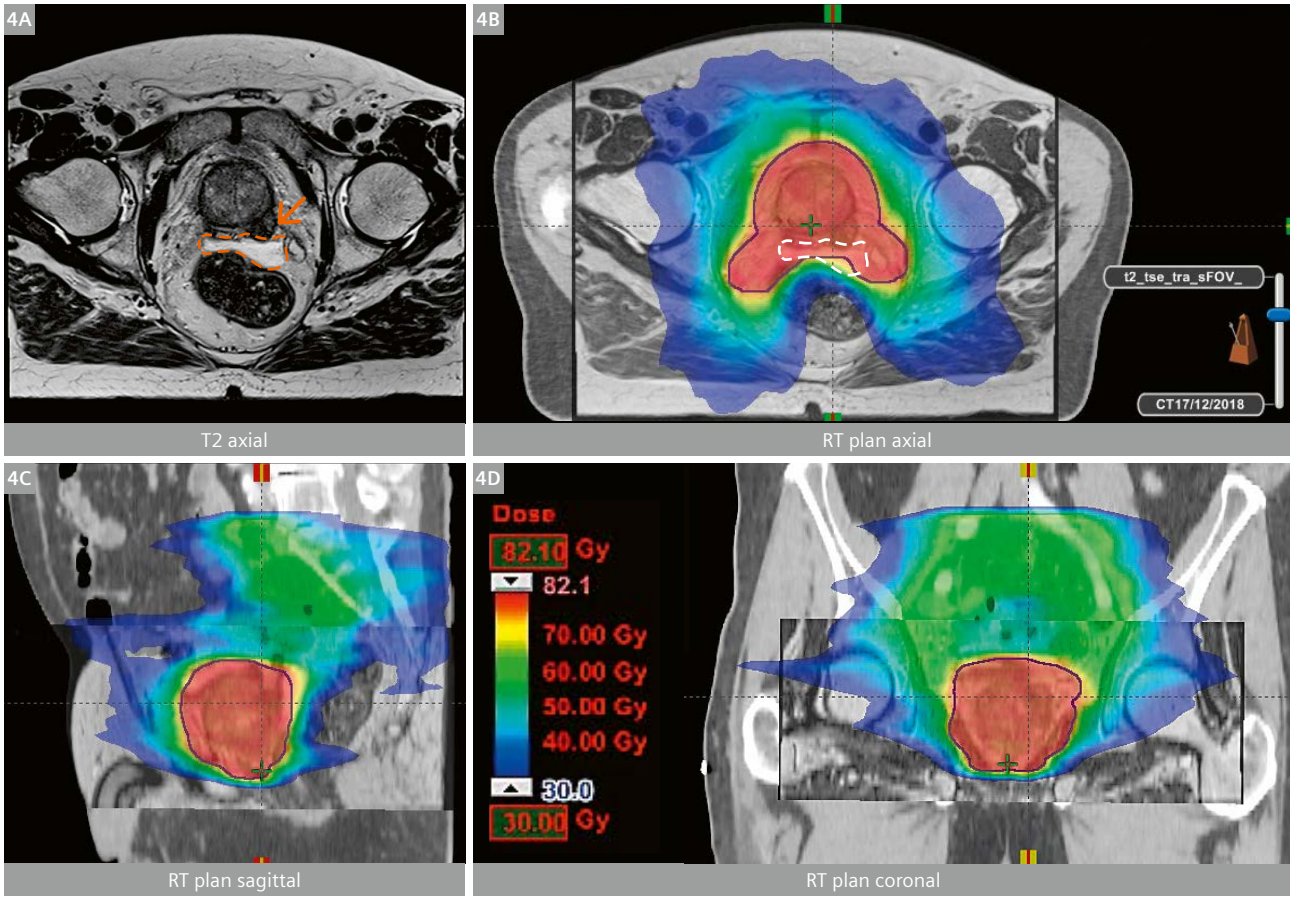

4 A 73-year-old man diagnosed with prostate cancer with iliac nodal involvement was referred for external beam radiotherapy (EBRT). **(4A)** The T2-weighted axial sequence demonstrates an index lesion in the left posterior peripheral zone (arrow), which was initially abutting the rectum. A rectal spacer (dashed outline) was inserted between the prostate gland and rectum, and the patient underwent radiation therapy planning scans **(4B-D)**. These show how the rectal spacer allows for minimal dose to the rectum without compromising the dose intensity to the prostate gland.

With collaboration between radiation oncology and clinical radiology, reporting radiologists can tailor reports to give pertinent positive and negative findings that would be relevant for a patient undergoing radiation therapy. Figure 4 shows a case where the clinical radiologist noted that the posterior prostatic lesion was abutting the rectum and therefore the patient would be at higher risk of rectal toxicity if external beam radiation therapy was selected. This was flagged in the report and at the MDT, and the patient subsequently had a biodegradable balloon spacer inserted between the prostate and the rectum to allow the radiation oncologist to accurately treat the posterior prostatic tumor while reducing the risk of rectal toxicity. This patient was successfully treated with radiotherapy without developing rectal toxicity. Three years after treatment, the patient developed biochemical recurrence and pain in the bony pelvis, so he underwent a pelvic MRI with morphological sequences only (Figs. 5A, B), which demonstrated a suspicious lesion within the S1 vertebral body extending to both sacral alar. Radiation therapy was considered and a CT-based radiotherapy treatment plan was performed. However, the MDT agreed that next-generation imaging with whole-body (WB) MRI using WB-DWI should be performed prior to radiation treatment (Figs. 5D, E) to exclude other sites of metastatic disease. Although no other sites of metastatic disease were identified, the DWI sequences demonstrated that the signal abnormality previously depicted in the posterior part of the vertebral body represented active hypercellular disease, whereas the signal change in both sacral alar was due to bilateral sacral insufficiency fractures, which are a well-recognized side effect of hormonal therapy, which the

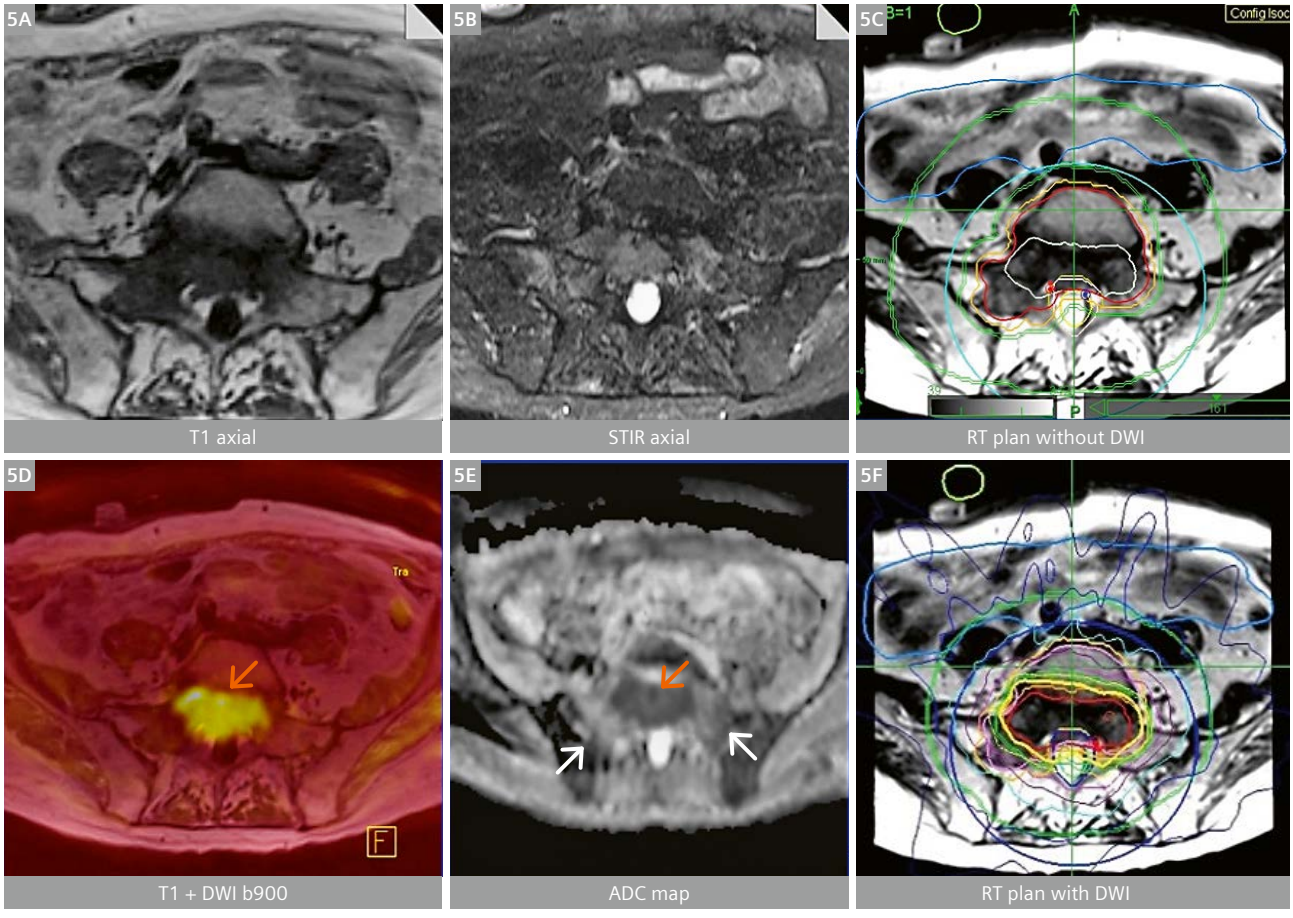

5 The patient in Figure 4 presented three years later with increasing pelvic pain. An MRI of the pelvis with morphological T1W **(5A)** and STIR **(5B)** sequences was performed. This demonstrated a suspicious lesion in the posterior part of the S1 vertebral body extending to both sacral alar. A radiotherapy plan was created **(5C)** using the information from this standard pelvic MRI. After MDT discussion, it was decided that the patient should undergo a WB-MRI with DWI to rule out other sites of metastatic disease. Other metastatic sites were excluded, but the functional data gleaned from this advanced study demonstrated active disease posteriorly in the S1 vertebral body as high signal on the b900 DWI sequence **(5D)** and low signal on the corresponding ADC map **(5E)**, indicating active hypercellular disease (orange arrows). However, the signal changes in both sacral alar demonstrated high signal (white arrows) on the ADC map **(5E)**, indicating T2-shine-through due to edema from bilateral sacral insufficiency fractures, presumably secondary to previous hormonal therapy administered three years prior. The inclusion of the functional data from the WB-MRI led to a significant alteration of the radiotherapy plan **(5F)** and minimized dose to non-metastatic regions.

patient had previously received. This significantly altered the CT-based radiation therapy field and inappropriate dose administration to non-malignant tissues was avoided due to valuable information gleaned from advanced imaging techniques.

In our final example, we discuss a case of how highly conformal SBRT was successfully used repeatedly in a prostate cancer patient with oligorecurrent disease to postpone the use of androgen deprivation therapy (ADT) (Figs. 6, 7). The patient had previously undergone a radical prostatectomy followed by pelvic radiotherapy because of pathological extra-prostatic disease on post-operative histology. The patient presented one-year post pelvic EBRT with biochemical recurrence. Knowledge of previous radiation therapy and potential side effects is crucial for the clinical radiologist as the pelvic MRI demonstrated a suspicious lymph node just above the previous radiation therapy field visible as bone marrow atrophy (Fig. 6). Next-generation imaging with WB-MRI which includes WB-DWI confirmed no other sites of distant metastatic disease and, following the MDT, the patient was selected for SBRT. A follow-up WB-MRI with DWI and drop in PSA confirmed successful treatment. Figure 7 demonstrates how the patient was followed with next-generation imaging techniques and PSA surveillance, and developed further oligometastatic disease which was treated with ablative radiation therapy techniques on three occasions over the subsequent years. Thus, the close collaboration between clinical radiology and radiation oncology colleagues with understanding and use of the technological advances in each other's fields successfully allowed the postponement of ADT use and therefore avoided the onset of potential side effects such as osteoporosis and metabolic syndrome [9].

Alternative radiation therapy techniques

Next-generation imaging techniques such as WB-MRI with DWI can also be extremely valuable in assessing a patient's suitability for different radiotherapy treatments. Radium-223 (^{223}Ra) is a calcium-mimetic alpha-particle

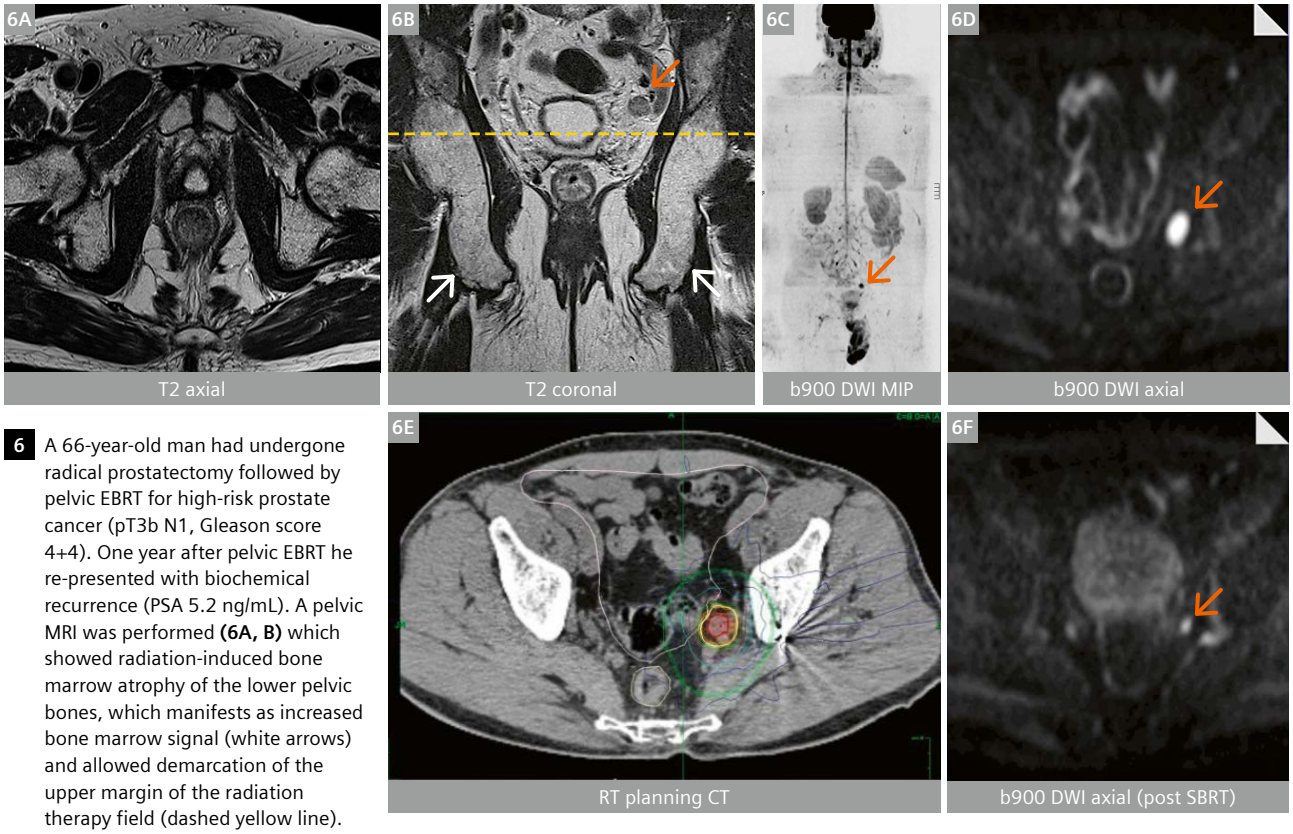

6 A 66-year-old man had undergone radical prostatectomy followed by pelvic EBRT for high-risk prostate cancer (pT3b N1, Gleason score 4+4). One year after pelvic EBRT he re-presented with biochemical recurrence (PSA 5.2 ng/mL). A pelvic MRI was performed **(6A, B)** which showed radiation-induced bone marrow atrophy of the lower pelvic bones, which manifests as increased bone marrow signal (white arrows) and allowed demarcation of the upper margin of the radiation therapy field (dashed yellow line). There was no suggestion of local recurrence at the prostatectomy bed. However just above the previous radiotherapy field there was a rounded left internal iliac lymph node (orange arrow) highly suspicious for a site of disease.

A WB-MRI with DWI was performed (**6C**: b900 DWI MIP, **6D**: b900 DWI axial) which confirmed that this was the only site of active disease (arrow) and therefore, the patient underwent SBRT following fiducial marker insertion (**6E**: planning CT). A follow-up WB-MRI three months post treatment (**6F**: b900 DWI axial) demonstrated successful ablative treatment with SBRT, which was in concordance with a reduction in PSA.

emitter which is taken up preferentially in areas of high bone turnover, particularly at sites of active bone metastases [10]. Thus, ^{223}Ra is a suitable treatment option in prostate cancer patients with bone metastatic disease and no soft tissue deposits >3 cm. WB-MRI with DWI and PET/CT with novel tracers such as gallium- and fluoride-labelled prostate-specific membrane antigen (PSMA) have been shown to have higher specificity and sensitivity to detect bone and soft tissue metastatic disease compared to conventional imaging techniques such as CT and bone scans [12, 13]. Therefore, these more advanced imaging techniques can be vital in accurate patient selection for these alternative radiation therapy techniques.

Conclusions and future directions

As advanced radiation therapy and imaging techniques are becoming more widely adopted, clinical radiologists and radiation oncologists should be aware of novel imaging and treatment developments in each other's specialties. To deliver the promise of precision radiation therapy for improved patient outcomes and decreased side effects, increased precision of imaging is needed. This is enabled with multiparametric functional imaging methods where quantitative imaging biomarkers can be mapped onto radiation planning imaging to show tumor probability maps and areas of heterogeneity. Imaging is also used to assess the effectiveness of radiation therapies and their potential side-effects.

The use of next-generation imaging techniques will be key to facilitate the use of novel treatment developments such as theranostics, which combines specific targeted pharmacotherapies based on specific targeted diagnostic tests such as ^{177}Lutetium-PSMA treatment [13]. Close collaboration between clinical radiology and radiation oncology departments will assist in these high-precision treatment advancements to allow personalized medicine for cancer patients.

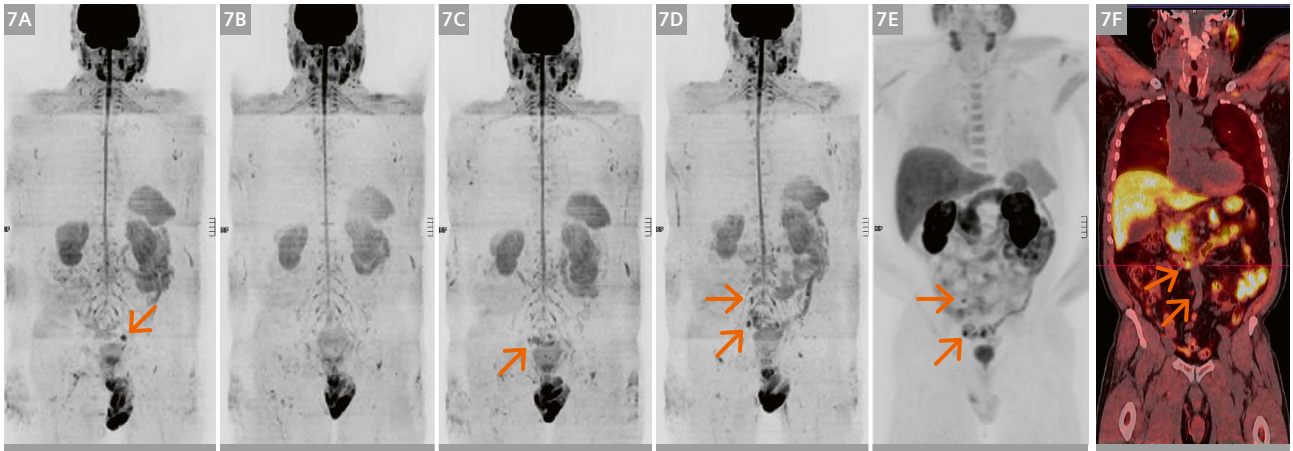

7 This series of images demonstrates how next-generation imaging techniques were used to enable advanced radiation therapy techniques for the patient from Figure 6 to postpone the use of ADT.

(7A) The WB-DW MRI MIP 12 months after prostatectomy and pelvic EBRT demonstrated a solitary left internal iliac lymph node (arrow) above the radiotherapy field which was treated with SBRT.

(7B) WB-MRI three months after SBRT shows successful treatment of the left internal iliac lymph node with a corresponding reduction in PSA.

(7C) WB-MRI performed seven months later due to a rise in PSA demonstrated a subtle focus in the right internal iliac region (arrow), which was reported as indeterminate but warranted close surveillance.

(7D) WB-MRI follow-up performed three months later showed an increase in size of the previous indeterminate right internal iliac lymph node and a new right common iliac lymph node in keeping with two nodal metastases (arrows).

(7E) A concurrent choline-PET/CT study confirmed these findings (arrows), which also correlated with the PSA rise. Two further SBRT treatments were performed and subsequent WB-MRI and choline-PET/CT studies showed no sites of active disease, and the PSA dropped to 0.02 ng/mL.

(7F) Two years after the previous SBRT treatments, the patient's PSA rose to 0.6 ng/mL and a choline-PET/CT study detected two new avid retroperitoneal lymph nodes (arrows), which were also treated with SBRT.

One year following the third SBRT treatments, there was new biochemical failure and imaging did not reveal any unequivocal sites of disease. After discussion with the patient, treatment with ADT was finally commenced after being postponed by over four years due to these advancements in imaging and radiation therapy techniques.

References

1 R. Atun, D. A. Jaffray, M. B. Barton, F. Bray, M. Baumann, B. Vikram, T. P. Hanna, F. M. Knaul, Y. Lievens, T. Y. M. Lui, M. Milosevic, B. O'Sullivan, D. L. Rodin, E. Rosenblatt, J. Van Dyk, M. L. Yap, E. Zubizarreta, and M. Gospodarowicz, "Expanding global access to radiotherapy," Lancet Oncol. 2015; 16(10):1153-86.
2 R. Baskar, K. A. Lee, R. Yeo, and K. W. Yeoh, "Cancer and radiation therapy: Current advances and future directions," Int. J. Med. Sci. 2012;9(3):193-9.
3 A. R. Padhani, F. E. Lecouvet, N. Tunariu, D. M. Koh, F. De Keyzer, D. J. Collins, E. Sala, S. Fanti, H. A. Vargas, G. Petralia, H. P. Schlemmer, B. Tombal, and J. de Bono, "Rationale for Modernising Imaging in Advanced Prostate Cancer," Eur. Urol. Focus. 2017;3(2-3):223-239.
4 H. U. Ahmed, A. El-Shater Bosaily, L. C. Brown, R. Gabe, R. Kaplan, M. K. Parmar, Y. Collaco-Moraes, K. Ward, R. G. Hindley, A. Freeman, A. P. Kirkham, R. Oldroyd, C. Parker, and M. Emberton, "Diagnostic accuracy of multi-parametric MRI and TRUS biopsy in prostate cancer (PROMIS): a paired validating confirmatory study," Lancet. 2017;389(10071):815-822.
5 N. L. Hansen, T. Barrett, C. Kesch, L. Pepdjonovic, D. Bonekamp, R. O'Sullivan, F. Distler, A. Warren, C. Samel, B. Hadaschik, J. Grummet, and C. Kastner, "Multicentre evaluation of magnetic resonance imaging supported transperineal prostate biopsy in biopsy-naïve men with suspicion of prostate cancer," BJU Int. 2018,122(1):40-49.
6 S. Borofsky, A. K. George, S. Gaur, M. Bernardo, M. D. Greer, F. V. Mertan, M. Taffel, V. Moreno, M. J. Merino, B. J. Wood, P. A. Pinto, P. L. Choyke, B. Turkbey, "What Are We Missing? False-negative Cancers at Multiparametric MR Imaging of the Prostate," Radiology. 2018,286(14):186-195.
7 E. Baco, E. Rud, L. Vlatkovic, A. Svindland, H. B. Eggesbø, A. J. Hung, T. Matsugasumi, J.-C. Bernhard, I. S. Gill, and O. Ukimura, "Predictive Value of Magnetic Resonance Imaging Determined Tumor Contact Length for Extracapsular Extension of Prostate Cancer," J Urol. 2015 Feb;193(2):466-72.
8 A. Gallina, F. K. Chun, N. Suardi, J. A. Eastham, P. Perrotte, M. Graefen, G. Hutterer, H. Huland, E. A. Klein, A. Reuther, F. Montorsi, A. Briganti, S. F. Shariat, C. G. Roehrborn, A. De Taille, L. Salomon, and P. I. Karakiewicz, "Comparison of stage migration patterns between Europe and the USA: an analysis of 11 350 men treated with radical prostatectomy for prostate cancer," BJU Int. 2008 Jun;101(12):1513-8.
9 P. Sountoulides and T. Rountos, "Adverse Effects of Androgen Deprivation Therapy for Prostate Cancer: Prevention and Management," ISRN Urol. 2013 Jul 25;2013:240108. doi: 10.1155/2013/240108.
10 S. Dadhania, R. Alonzi, S. Douglas, A. Gogbashian, R. O. B. Hughes, D. Dalili, N. Vasdev, J. I. M. Adshead, and T. I. M. Lane, "Single-centre Experience of Use of Radium 223 with Clinical Outcomes Based on Number of Cycles and Bone Marrow Toxicity," Anticancer Res. 2018 Sep;38(9):5423-5427.
11 G. Shen, H. Deng, S. Hu, and Z. Jia, "Comparison of choline-PET / CT, MRI, SPECT, and bone scintigraphy in the diagnosis of bone metastases in patients with prostate cancer: a meta-analysis," Skeletal Radiol. 2014 Nov;43(11):1503-13.
12 M. Eiber, T. Maurer, M. Souvatzoglou, A. J. Beer, A. Ruffani, B. Haller, F. Graner, K. Hubert, U. Haberhorn, M. Eisenhut, H. Wester, J. E. Gschwend, and M. Schwaiger, "Evaluation of Hybrid 68 Ga-PSMA Ligand PET/CT in 248 Patients with Biochemical Recurrence After Radical Prostatectomy," J Nucl Med. 2015 May;56(5):668-74.
13 L. Emmett, K. Willowson, J. Violet, J. Shin, A. Blanksby, and J. Lee, "Lutetium 177 PSMA radionuclide therapy for men with prostate cancer: a review of the current literature and discussion of practical aspects of therapy," J Med Radiat Sci. 2017 Mar;64(1):52-60.

Contact

Amish Lakhani, MBBS MA (Cantab) FRCR
Paul Strickland Scanner Centre
Mount Vernon Hospital
Northwood
Middlesex HA6 2RN
UK
amish.lakhani@stricklandscanner.org.uk

We are looking forward to hearing from you

The essence of *MReadings: MR in RT* is education and best practice sharing by MAGNETOM users. Along with the MAGNETOM World Internet site it is a platform to share experience around the globe.

In times of online media and digitalization we would value your feedback to ensure that the magazine continues to fit your interests and professional needs.

Please take a moment to complete a brief reader survey at
www.siemens.com/magnetom-world-rt

Synthetic CT Generation for the Pelvic Region Based on Dixon-MR Sequences: Workflow, Dosimetric Quality and Daily Patient Positioning

Daniela Thorwarth[1]; Corinna Warschburger[1]; David Mönnich[1]; Ulrich Grosse[2]; Matthias Kündel[2]; Konstantin Nikolaou[2]; Daniel Zips[3]; Daniel Wegener[3]; Arndt-Christian Müller[3]

[1]Section for Biomedical Physics, Department of Radiation Oncology, University Hospital Tübingen, Germany
[2]Department of Diagnostic and Interventional Radiology, University Hospital Tübingen, Germany
[3]Department of Radiation Oncology, University Hospital Tübingen, Germany

Introduction

Over the past couple of decades, the adoption of MR imaging in support of Radiation Therapy treatment planning has increased dramatically. As an example, MRI utilization in RT treatment planning in the United States increased from 6% to 24% between 2006 and 2017 [1]. This growing trend can be contributed in part to the superior soft tissue contrast of MRI compared to CT imaging. This can allow to potentially have much more precise delineation of not only a patient's tumor, but also of surrounding organs at risk (OAR). Additionally, MR offers functional imaging to derive more information on tumor activity and therapy response.

However, the inherent limitation of MRI for RT planning compared to CT is that it has not been able to provide the electron density information which is needed for dose calculation in a treatment planning system (TPS). For this reason, and because CT provides good delineation of bony structures and the highest geometric accuracy in its imaging, CT remains utilized in almost 100% of RT planning [1].

1 Patient positioning example for MR sim for pelvis imaging including flat couch top overlay and dedicated coil holder (Qfix, Avondale, PA, USA) for body coil.

As such, more and more institutions are adopting a workflow which includes both traditional CT simulation for dose calculation but also MR simulation for superior and more precise delineation of tumors and surrounding OAR.

A combined MR and CT workflow has the potential to provide higher accuracy in both target volume and OAR definition. From CT we obtain accurate dose calculations from attenuation tissue properties and generation of reference images (DRR) used for patient positioning and beam placement, and from MR, good soft tissue contrast as well as functional imaging. However, challenges of such a combined MR and CT workflow are also introduced. These challenges may include, for example, accurate image registration between MR and CT, patient scheduling, and financial issues such as reimbursement.

Because of these challenges, institutions have been searching for ways to implement an MR-only workflow for their patient's treatment planning. While research has been ongoing for a few years, commercially available features enabling an MR-only workflow have only recently become available. We describe a method that allows us to adopt an MR-only workflow. Synthetic CT is commercially available as part of the *syngo*.via RT Image Suite[1] and is available for both brain as well as male and female pelvis.

MR-only radiotherapy workflow

Patient preparation and MR imaging

Pelvic patients scheduled for MR simulation need to be examined in RT treatment position, i.e. a flat table top for the MR scanner is required in addition to a dedicated coil holder to fix the flexible radiofrequency (RF) body coil without deforming the patient contour, as depicted in Figure 1 Furthermore, all necessary positioning devices,

[1]*For 3T MAGNETOM Vida and 1.5T MAGNETOM Sola with software version syngo MR NXA11A or later.*

such as knee fix, feet holder, etc. need to be available in MR-compatible fashion in order to position the patient accurately. Reference point markings need to be done using MR-visible markers and a MR-compatible laser bridge.

For the generation of a Synthetic CT (sCT), Siemens Healthineers offers dedicated Dixon sequences resulting in water, fat, in- and out-of-phase images which can then later be used to calculate Synthetic CT. To acquire the Dixon scans, the transversal field of view should encompass the entire patient outline and needs to be centered right above the hips in z-direction in order to cover lumbar vertebra L3. Furthermore, additional scans in diagnostic quality should be acquired in order to allow accurate target volume delineation, such as e.g. T2-weighted 3D turbo spin echo (TSE), diffusion weighted (DW) MRI and eventually T1-weighted or other MR sequences, depending on the patient case.

Generation of Synthetic CT data

After successful acquisition of the Dixon scans, the four different data sets are imported into the *syngo*.via RT Image Suite (RTiS). Here, a dedicated tool for data management is foreseen to calculate the CT based on the four Dixon-MR data sets. The resulting sCT data set is available in CT-dicom format and contains four different density compartments: fatty tissue, water-equivalent tissue, air and bone / dense bone (Fig.6). The data set is directly fused to the anatomical MR-data which have been acquired during the same session, i.e. contours generated on the anatomical MR can directly be saved on the sCT for later dose planning and calculation.

Clinical Synthetic CT images for pelvis

In a testing phase a total of n = 13 prostate cancer patients were asked to undergo MR simulation in addition to conventional CT simulation in order to evaluate sCT image quality, to investigate the dosimetric effects of using sCT data for RT dose calculation and to evaluate the usability of sCT data for daily positioning verification of the patient at a RT machine equipped with cone beam CT (CBCT). Three patients were imaged with the MAGNETOM Skyra[2] 3T scanner, five patients were imaged with the MAGNETOM Aera[2] 1.5T scanner, and five patients were imaged with the MAGNETOM Vida 3T scanner.

Figure 2 displays the four different Dixon-MR sequences from which the respective sCT is derived for an exemplary patient case.

In Figure 3, the Synthetic CT is compared to the real planning CT taken for this patient on the same day.

Contouring of tumor regions and organs at risk is done based on the anatomical T2w MRI data set after MR sim. The RT structure set is saved together with the sCT which facilitates transfer of the data to the RT planning system and subsequent treatment planning.

[1] *Work in progress: the application is currently under development and is not for sale in the U.S. and in other countries. Its future availability cannot be ensured.*

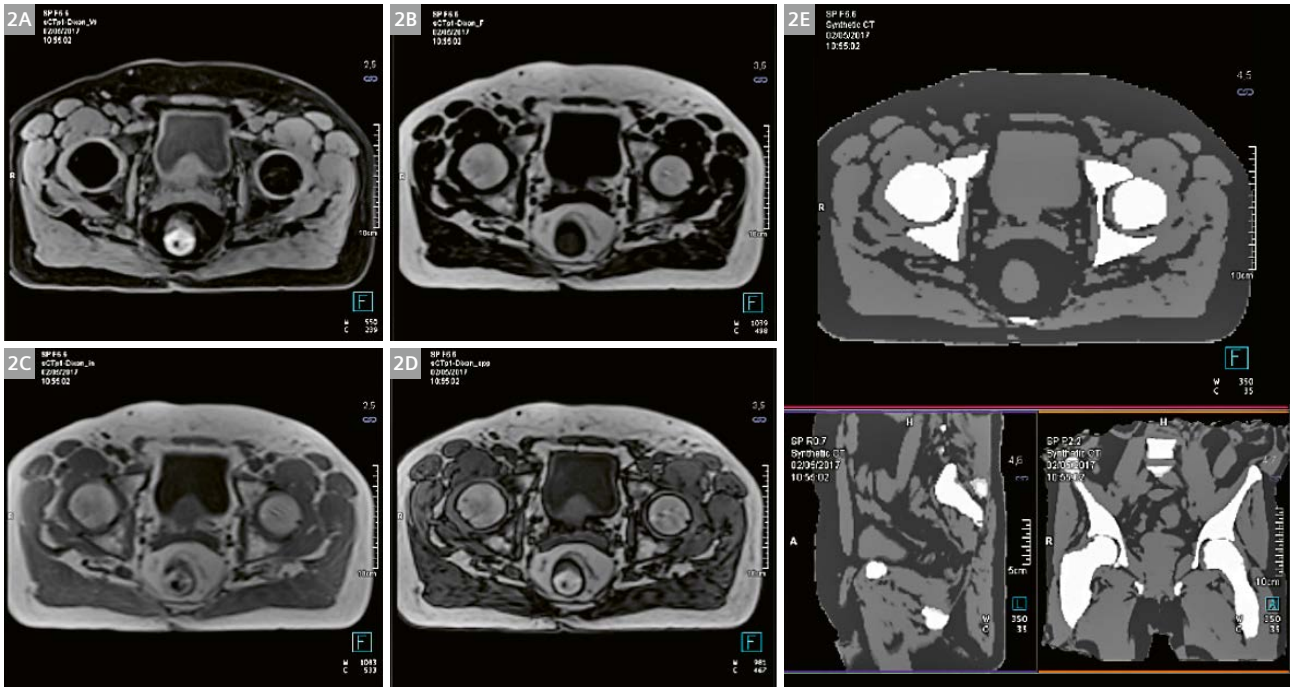

2 Four reference MR images acquired with the Dixon scan protocol **(2A)** water, **(2B)** fat, **(2C)** in-phase and **(2D)** out-of-phase Dixon data. **(2E)** Displays the Synthetic CT data set reconstructed from data sets (2A-D).

Evaluation of Synthetic CT dose calculation accuracy

For all patients included into this study, the accuracy of dose calculation based on the sCT was evaluated by comparing the 3D dose distribution to the planning CT. For treatment planning, the Tübingen in-house planning system for intensity modulated radiotherapy (IMRT) was used. For all patients, planning CT data including planning target volume (PTV_{pCT}) and organ at risk (OAR_{pCT}) contours were available. After dedicated planning MR (pMR) examinations, sCT were calculated and a second set of PTV_{pMR} and OAR_{pMR} contours were created based on the anatomical T2w MRI. Then, an IMRT plan was optimized for the planning CT. The final plan was then recalculated on the sCT using Monte Carlo dose calculation with a maximum uncertainty of 1%. Dose volume histograms (DVH) were compared for PTV_{pCT}/PTV_{pMR} and OAR_{pCT}/OAR_{pMR}, respectively. Furthermore, the 3D dose distributions which were obtained using the planning CT and the sCT were compared using a gamma analysis with a gamma criterion of Γ = 3%/3 mm. In a last step of this analysis, the sCTs were exported to the treatment machine (Elekta AB, Sweden equipped with CBCT) in order to evaluate the accuracy of using sCT data for daily positioning verification.

Figure 5 shows dose distributions for the same plan calculated on the original planning CT and the MR-based sCT. Depending on the actual patient positioning during planning CT and subsequent MR simulation, overall very good agreement between the original dose distribution and the dose recalculated on the sCT was observed in this study.

Figure 6 displays the DVH analysis for one patient, comparing for DVHs for the contours defined on the

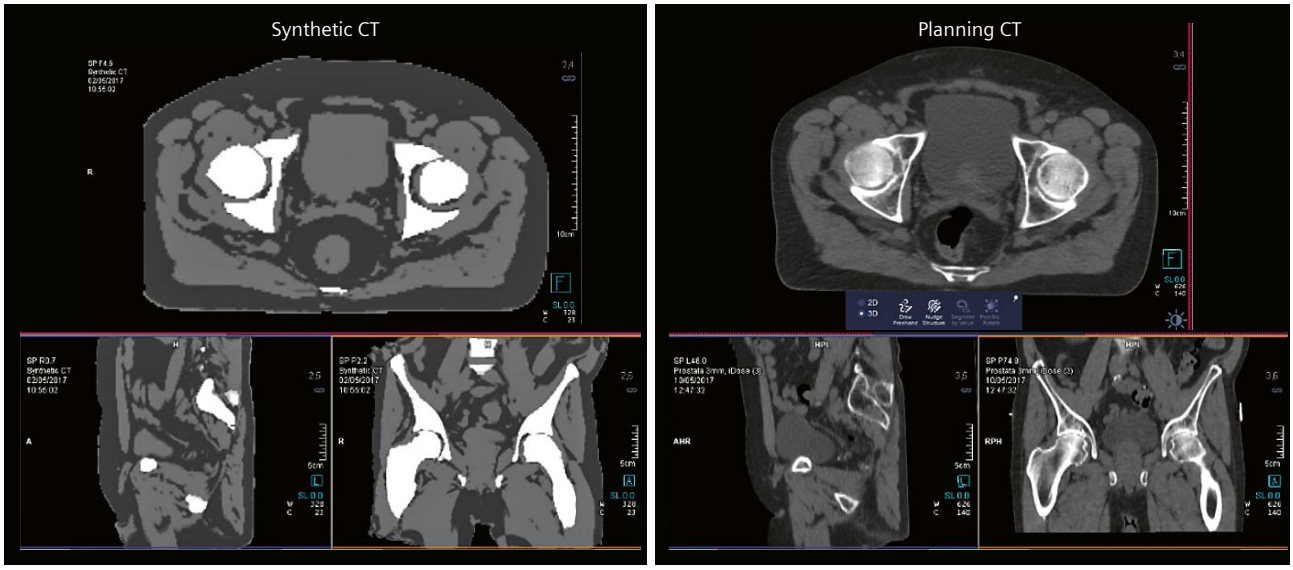

3 Synthetic CT (left) compared to conventional planning CT (right) of the same patient.

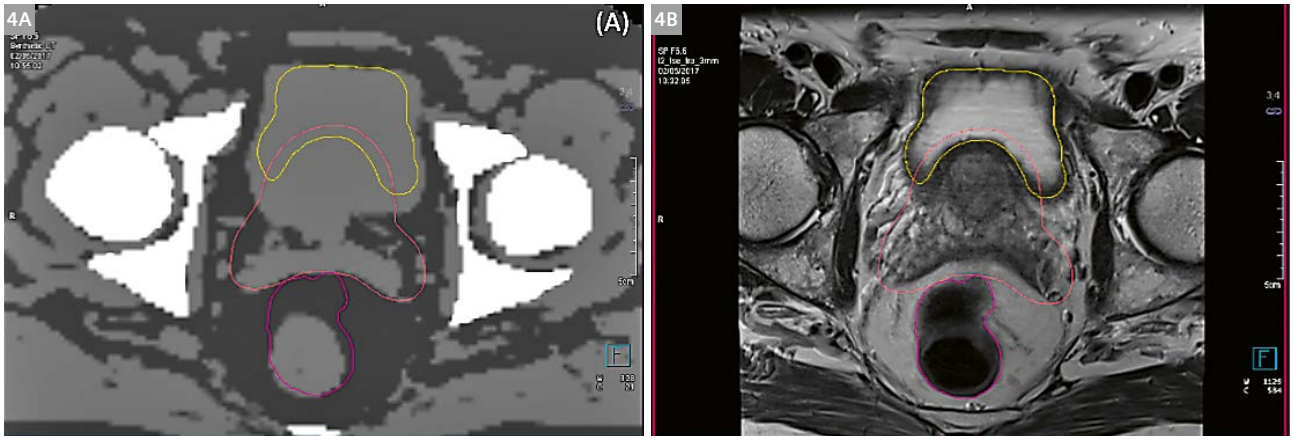

4 Synthetic CT **(4A)** with radiotherapy contours for planning target volume (PTV) in orange, rectum in pink and bladder in yellow which were created using an anatomical T2w TSE MRI **(4B)**.

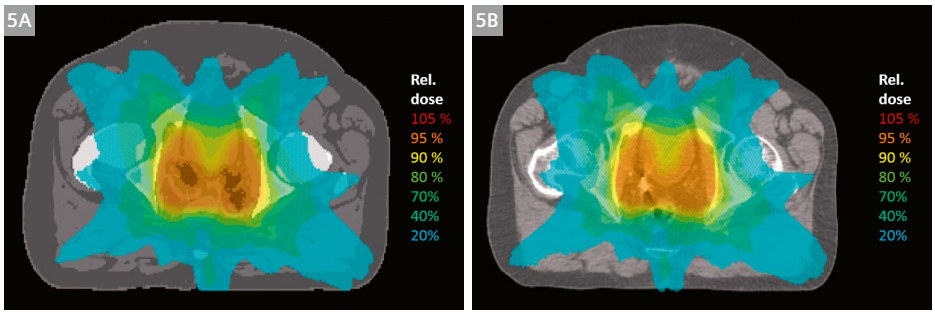

5 Relative dose distribution recalculated on the sCT **(5A)**, compared to the original dose distribution calculated on the planning CT **(5B)**.

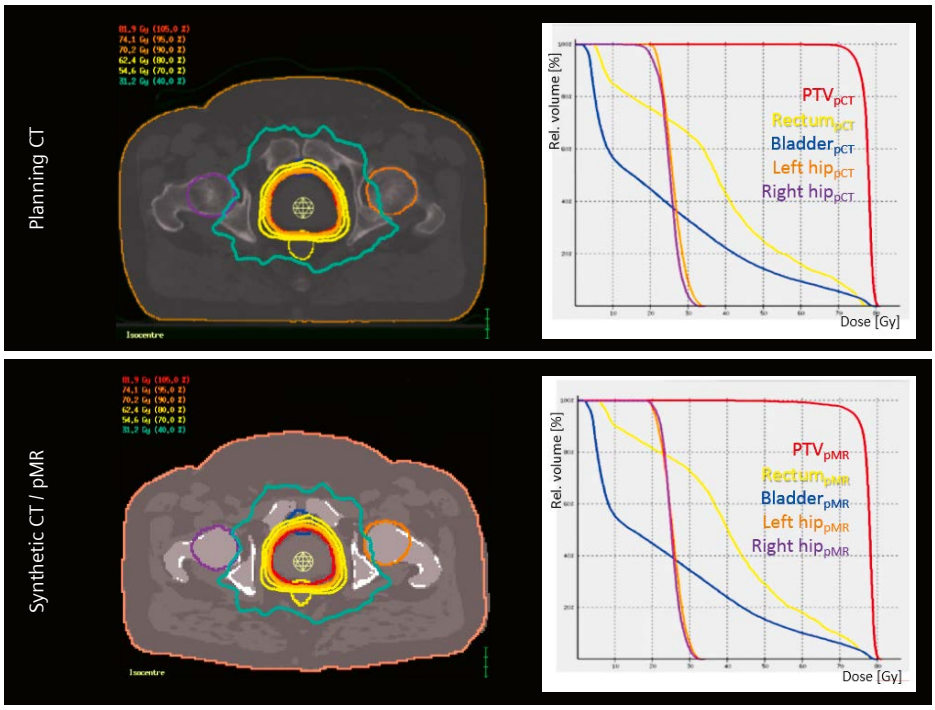

6 Planning CT with original dose distribution and DVHs for volumes created on the pCT (upper row). Synthetic CT with contours defined on the planning MR and corresponding DVHs for recalculated dose based on sCT (lower row).

planning CT (pCT) and the original dose distribution with the DVHs of volumes defined on the planning MR (pMR) and the dose recalculated with the sCT.

The gamma analysis shown in Figure 7 nicely shows the high level of agreement when comparing the original dose distribution with the dose recalculated on the sCT. Overall, a mean agreement of 98.7 % (range: 98.0 – 99.9 %) was found in this study.

In a last analysis step, the accuracy of using sCT for daily CBCT position verification was checked for this patient population by comparing sCT-CBCT registration results to pCT-CBCT registrations. Daily positioning accuracy was calculated to six degrees of freedom (three translational and three rotational axes). Each translation/rotation vector was calculated using either the pCT or the sCT as a reference scan. In total, mean differences of 3.4 mm / 1.5 mm / 4.8 mm in x-, y- and z-direction respectively (range: 0 – 10.6 mm) were observed as well as mean differences in the rotational degrees of freedom of 1.8° (range: 0 – 5.18°).

Figure 8 shows a comparison of using the original planning CT vs. the sCT as a reference image to be matched with the daily CBCT in the XVI matching tool (Elekta AB, Sweden).

Discussion

In this study involving 13 patients with cancer treatments planned in the pelvic region, the sCT workflow proposed by Siemens Healthineers was tested and evaluated in terms of dosimetric accuracy, image quality and suitability of sCT to be used for daily positioning verification at the RT treatment machine.

Overall, the MR simulation workflow is straight forward and ready to be used in academic departments as well as for clinical routine. Dedicated sequences are available to be applied during the MR examination. An essential prerequisite for accurate reconstruction of the Synthetic CT is the selection of a correct field of view for the Dixon sequences. The sCT data consist of four different density compartments, which results in a dosimetric accu-

racy of 1 – 2%. However, the evaluation of the dosimetric accuracy depends strongly on the positioning of the patient. If small discrepancies exist between patient positioning during pCT and pMR, this will result in dosimetric differences. However, in the pelvic region, sCT seems to present accurate dose calculation accuracy for clinical radiotherapy treatments. Furthermore, MR simulation which comes together with sCT reconstruction is providing excellent soft tissue contrast and thus allows for more accurate target volume delineation.

Reference

1 Lorna Young et al., IMV Radiation Therapy Market Summary Report. Oct 2018.

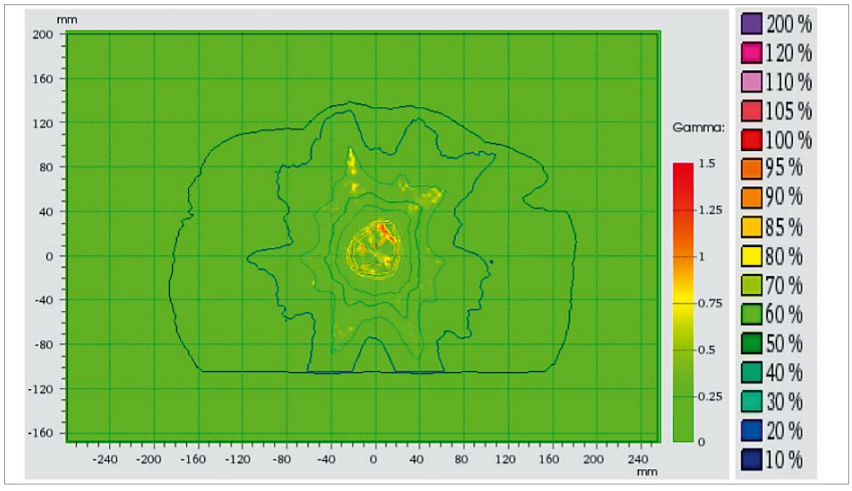

7 Gamma map of a representative section of one patient case, generated with the software tool VeriSoft (PTW Freiburg, Germany). Here, an agreement according to the gamma criterion 3%/3 mm is reached in 99.6 % of all voxels.

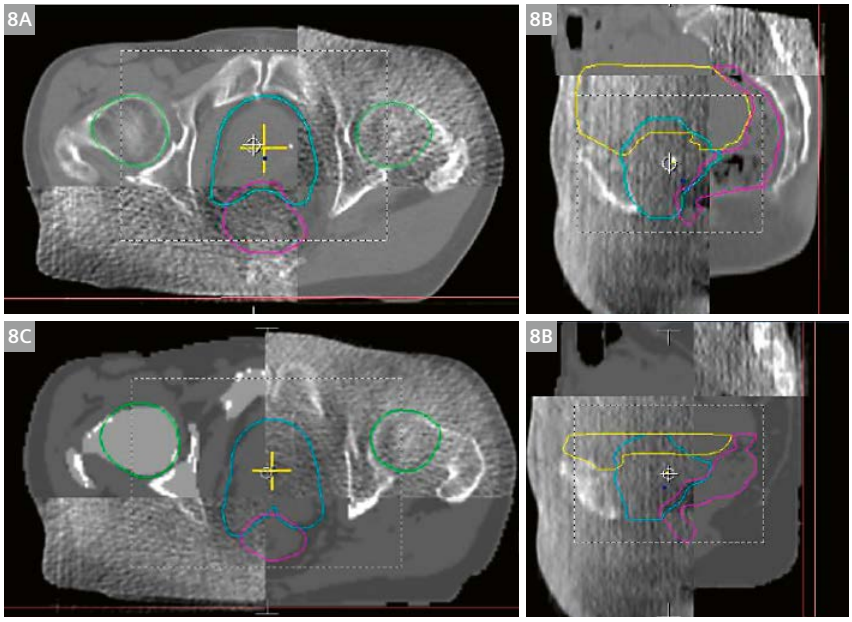

8 Comparison of using original planning CT data for daily position verification with respect to the CBCT **(8A, B)** vs. using the sCT data set as a reference image for daily position verification **(8C, D)**.

Contact

Daniela Thorwarth
Section of Biomedical Physics
University Hospital for Radiation Oncology
University of Tübingen
Hoppe-Seyler-Strasse 3
72076 Tübingen
Germany
daniela.thorwarth@med.uni-tuebingen.de

Initial Clinical Experience Utilizing 4D-MRI for Radiation Treatment Planning

Eric S. Paulson[1–3]; Nikolai J. Mickevicius[1,3]

[1]Department of Radiation Oncology, Medical College of Wisconsin, Milwaukee, WI, USA
[2]Department of Radiology, Medical College of Wisconsin, Milwaukee, WI, USA
[3]Department of Biophysics, Medical College of Wisconsin, Milwaukee, WI, USA

Introduction

Knowledge of target and organ at risk (OAR) motion trajectories is essential in radiation therapy. Motion can result in a smearing of planned dose distributions, particularly when steep dose gradients are employed to reduce radiation doses to proximal OARs [1]. This can result in an inevitable disconnect between planned and actual doses delivered to targets and OARs over the course of treatment.

Motion management in radiation therapy involves two components: 1) generation of high-fidelity static images of targets and OARs along with models of respiratory motion for use in treatment planning, 2) real-time intrafraction motion monitoring for exception gating and/or tracking during treatment delivery [1]. Currently, the clinical standard-of-care to address the former relies on four-dimensional (4D) computed tomography (CT) images of the patient [2]. However, the poor soft tissue contrast can challenge accurate target and OAR delineation in some cancer sites with CT [3] and, thus, the accuracy of motion models obtained with this approach. Consequently, larger margins are often prescribed to prevent underdosing of tumor targets [1, 4].

Due to its non-ionizing and high soft tissue contrast properties, magnetic resonance imaging (MRI) is an ideal 4D-imaging platform. A multitude of 4D-MRI strategies have been explored in the literature, utilizing prospective and retrospective acquisitions of multi-slice 2D or 3D excitations with Cartesian and non-Cartesian readouts and a variety of motion surrogates [5–15]. Recently, self-navigated, under-sampled, retrospectively sorted 3D volumetric acquisitions have been introduced for 4D-MRI. Although long acquisition and reconstruction times (up to 8 minutes and several hours, respectively) have been reported with some of these methods, the 3D radial stack-of-stars method [12–15] offers great potential to minimize acquisition and reconstruction times while maintaining image quality. In addition, the method facilitates ease of extracting motion surrogates and is robust against motion artifacts from the inherent properties of radial *k*-space trajectories. We discuss here our initial clinical experience performing and utilizing 4D-MRI for radiation treatment planning.

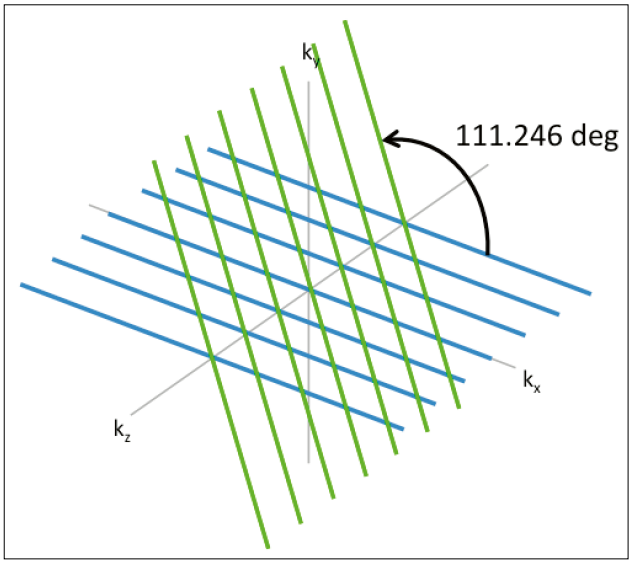

1 Hybrid 3D golden angle radial stack of stars trajectory. All partitions defining a spoke-plane are acquired before incrementing the spoke angle.

Methods

Patients undergoing MR simulation for radiotherapy of abdominal or thoracic cancers were imaged with 4D-MRI after providing informed written consent under guidelines established by the IRB at our Institution. Following CT simulation, patients were transferred to a 3T MAGNETOM Verio scanner (Siemens Healthcare, Erlangen, Germany) and set up in treatment position on a flat table overlay. Two 6-channel flexible array coils were wrapped around the anterior of the patient and suspended on expandable RF coil bridges. Combined with the spine array, between 21 and 24 receive coils were used for imaging. Per standard MR simulation protocols at our Institution, glucagon (1 mg, Novo Nordisk, Bagsværd, Denmark) was administered intravenously in abdominal cancer patients to reduce peristalsis. Post-contrast imaging was performed following administration of Eovist (10 mL, Bayer Healthcare, Berlin, Germany) for cholangiocarcinoma patients, or Multihance (0.1 mmol/kg, Bracco Imaging, Milano, Italy).

4D-MRI acquisition

A hybrid, slab-selective, 3D radial VIBE sequence of our own design was implemented for 4D-MRI. The sequence supports switchable FLASH, FISP, TrueFISP, and PSIF modes for T1 and mixed T2/T1-weighted contrasts. A 3-point Dixon readout, integrated into the sequence, is available for FLASH and FISP modes. Cartesian encoding of partitions is performed along the slab-select direction (k_z) for a given spoke angle, forming a spoke-plane. After acquisition of the prescribed partitions within the spoke-plane, the spoke angle is incremented by the golden angle (pi*golden ratio = 111.246°) and another spoke-plane is acquired (Fig. 1). This process is repeated for the entire scan duration. In this manner, a unique spoke is sampled throughout the entire duration of the acquisition, eliminating the need to complex average overlapping spokes after the *k*-space data are retrospectively sorted into respiratory phases. Typical 4D-MRI scan parameters included: axial prescription, field-of-view: 330 mm, base resolution: 192, readout bandwidth: 200 kHz, TE/TR: 1.3/3.5 msec, flip angle: 10°, slab thickness: 240 mm, total acquisition time: 2 minutes.

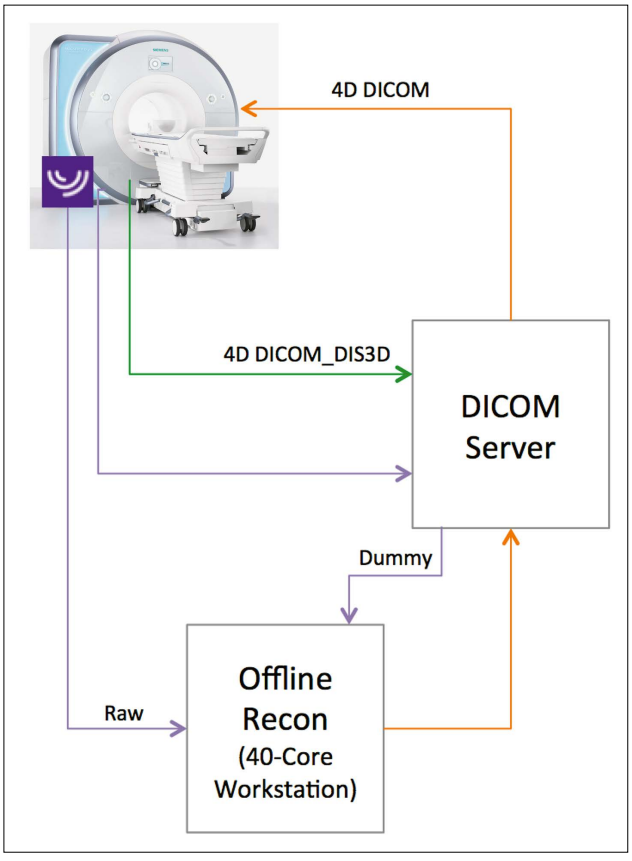

2 Flow diagram for offline 4D-MRI reconstruction. See text for details.

4D-MRI reconstruction pipeline

Figure 2 displays a flow diagram of the 4D-MRI reconstruction pipeline. The raw *k*-space data were transferred offline to a 40-core, 2.3 GHz Linux workstation using the Yarra RDS client (https://yarra.rocks/doc/client/RDS). In addition, DICOM images from a quick dummy scan, acquired over the same geometrical prescription, were exported to the workstation to facilitate gradient nonlinearity correction. The reconstructed 4D-MR images were converted to DICOM with header information transferred from the dummy scan headers. The 4D-MRI DICOM images were then piped back to the scanner where 3D gradient nonlinearity distortion correction was performed online (orange arrows in Fig. 2). Finally, the distortion corrected 4D-MR images were sent to a clinical delineation software package for use during radiation treatment planning (green arrows in Fig. 2).

4D-MRI reconstruction

4D-MR images were reconstructed in Matlab (The Mathworks, Natick, MA, USA) using the non-uniform fast Fourier transform (NUFFT) toolbox [16]. Projections along the slab-select direction were generated by taking the 1D Fourier transform of the acquired *k*-space signal passing through the axis of rotation (kx = ky = 0). One-dimensional motion surrogate signals from all receive coils were generated by plotting the center of mass of each projection, or the cross-correlation coefficient of a given projection against a reference projection as a function of time. These signals were then bandpass filtered between 0.1 and 0.5 Hz to remove DC offset and high frequency fluctuations (e.g., cardiac motion). Principal component analysis was

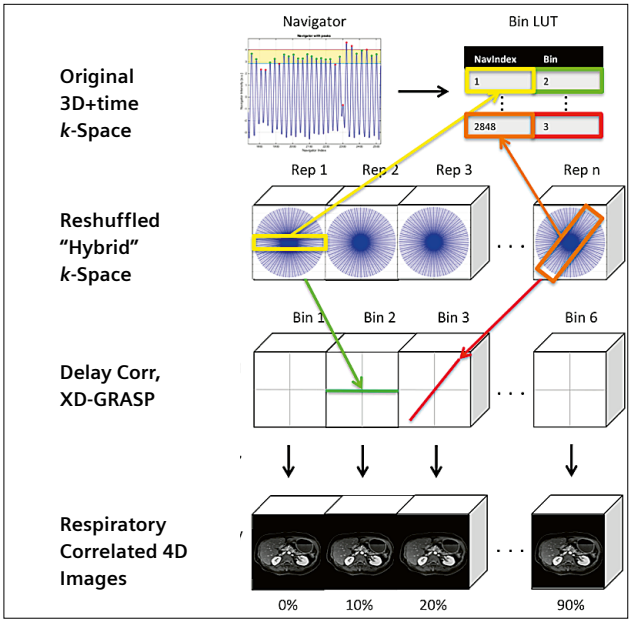

3 Flow diagram of 4D-MRI reconstruction. See text for details.

performed to obtain a single motion surrogate signal using information from all receive coils. This derived navigator signal, analogous to external motion surrogate signals acquired using reflector-camera or respiratory bellows during 4D-CT acquisitions, arises from changes in total signal power during respiration. Constrained amplitude-based sorting was then applied to retrospectively reshuffle each acquired spoke-plane into a hybrid *k*-space of six-to-eight respiratory phase bins. Correction for gradient and receive chain group delays was performed using an iterative approach [17]. The XD-GRASP algorithm [14, 18], a compressed sensing method exploiting temporal sparsity, was then applied to improve image quality. This process is shown graphically in Figure 3. The Cartesian sampling of the radial stack of stars trajectory was exploited to reduce image reconstruction time by parallelizing over partitions once an initial 1D Fourier transform along the slab-select direction was performed [15].

4D-MRI radiation treatment planning

4D-MR images were loaded into clinical delineation software side-by-side with conventional 4D-CT images sorted based on reflector-camera surrogate. Maximum target motion extents and trajectories were compared between 4D-MRI and 4D-CT. Internal target volumes were constructed on the 4D-CT images and reviewed for agreement on the 4D-MR images.

Results

All patients successfully completed the 2-minute 4D-MRI acquisition. Total reconstruction time was approximately 8 minutes, demonstrating the advantage of the 4D radial stack-of-stars approach in permitting the reconstruction to be parallelized over partitions. Unlike conventional 4D-CT or other 4D-MRI methods relying on peripheral motion surrogates, no gain resetting or signal saturation was observed in the self-navigated radial stack of stars 4D-MRI motion waveforms used to guide the *k*-space data reshuffling.

Figure 4 displays one respiratory frame of 4D-CT, and T1-weighted 4D-MR images of a cholangiocarcinoma patient obtained prior to and 20 minutes post-Eovist administration. Consistent with prior studies [14, 15], the XD-GRASP algo-rithm was effective at reducing under-sampling artifacts in the reshuffled pre- and post-contrast 4D-MRI data. The tumor region is more readily discernable on pre and post-Eovist 4D-MR images compared to 4D-CT images. The post-Eovist 4D-MR images also demonstrate a clear demarcation between functioning and dysfunctioning hepatocytes.

Figure 5 displays one respiratory frame of 4D-CT and post-Multihance T1-weighted 4D-MR images in a patient with liver metastasis. The liver met is more easily visualized on the 4D-MR images compared to 4D-CT (yellow arrow). In addition, the 4D-MR images do not demonstrate stitching artifacts present on the 4D-CT (evident at the lung-liver interface in the sagittal plane).

Figure 6 displays axial, water-only and fat-only T1-weighted 4D-MR images at inspiratory and expiratory phases for a pancreas cancer patient, obtained using a 4D-MRI Dixon FLASH acquisition. The reconstruction algorithm was effective at separating fat, water, and motion phases.

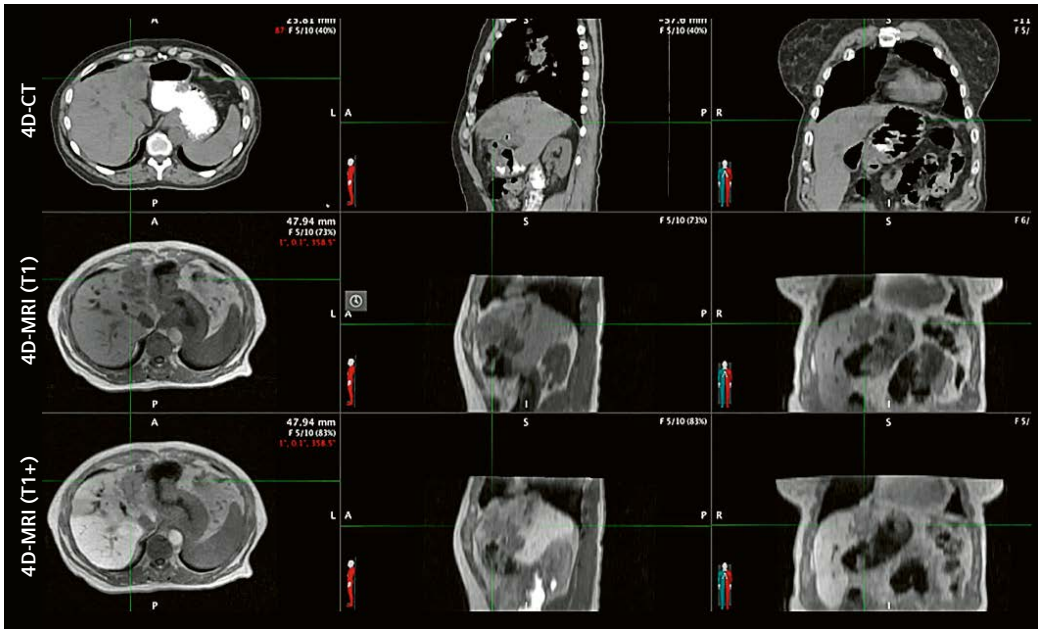

4 Comparison of 4D-CT (top row) and T1-weighted pre- (middle row) and 20 minute post-Eovist (bottom row) 4D-MR images in a cholangio-carcinoma patient.

Figure 7 displays one respiratory frame of a mixed T2/T1-weighted 4D-MR image obtained in a healthy volunteer using a 4D-MRI PSIF acquisition. Compared to TrueFISP, the PSIF image does not demonstrate banding artifacts but does display increased T2 contrast (evident from the bright cerebrospinal fluid signal).

Figure 8 demonstrates the feasibility of using 4D-MRI as a vehicle. In this case, respiratory-triggered T2 images are transformed to a time-averaged, mid-position 4D-MR image [19]. This process permits image contrasts to be acquired at a phase of the respiratory cycle more favorable for acquisition and then be transformed to a potentially different respiratory phase more favorable for treatment delivery.

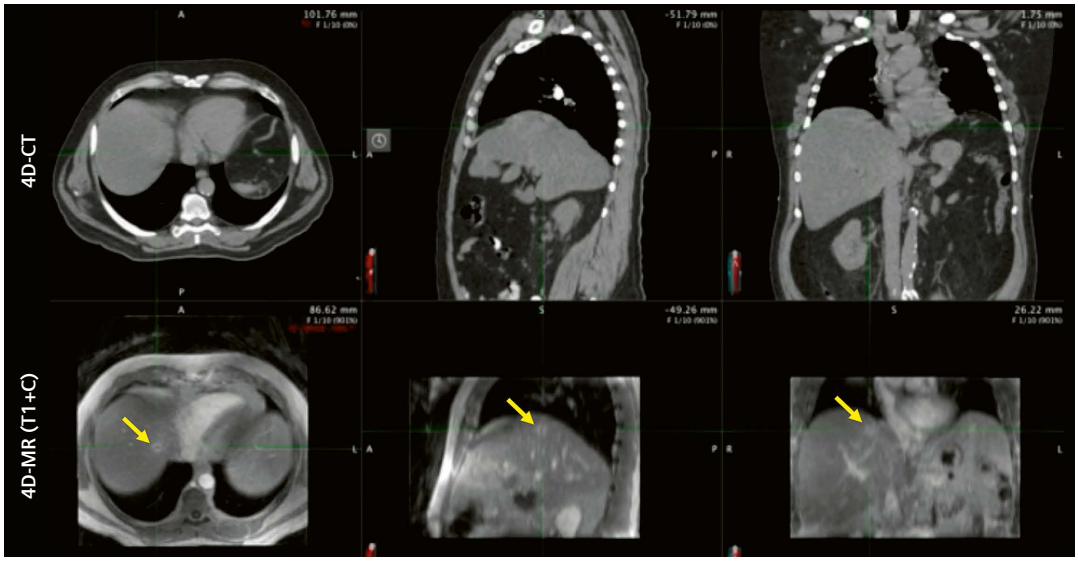

5 End expiratory 4D-CT (top) and post-Multihance T1-weighted 4D-MR (bottom) images of a liver metastasis patient. The enhancing liver met is more readily visible on the 4D-MR images (yellow arrow).

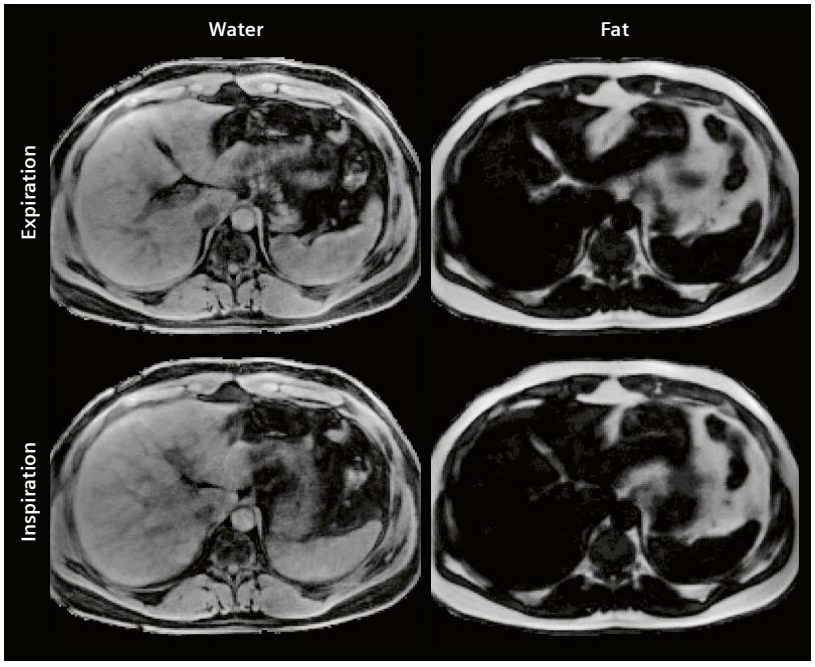

6 Water-only and fat-only inspiratory and expiratory 4D-MR images of a pancreas cancer patient obtained using a 4D Dixon FLASH acquisition.

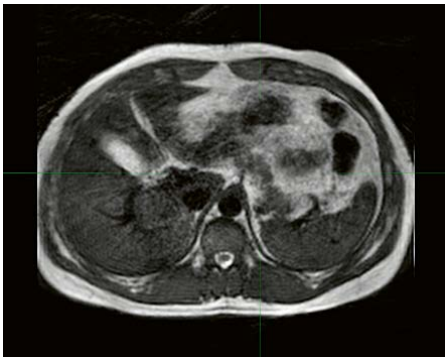

7 Mixed T2/T1-weighted 4D-MR image of a healthy volunteer acquired using a 4D-MR PSIF acquisition. The increased T2 weighting is evident by the bright CSF signal.

Discussion

The 4D-MRI method discussed here utilizes the self-navigating properties of radial *k*-space trajectories to generate respiratory-correlated 4D-MR images. The change in intensity producing the self-navigating signal arises from a change in total signal power in the excited volume during respiration. The method eliminates the need for external respiratory surrogates (bellows, reflector camera, body surface area, etc), and improves image contrast and reduces sorting errors compared to 4D-CT. The spin system steady state is maintained by consecutively exciting the same slab with each shot, and increased efficiency is obtained by eliminating the need to interlace 1D pencil beam or 2D image navigators. In a prior motion phantom study, the displacement estimates obtained with the 4D-MRI method used here were within 1 mm [15].

We have made several observations during our initial clinical experience of performing and utilizing 4D-MRI for treatment planning:

- 4D-MRI may increase clinical efficiency compared to 4D-CT, depending on the technology available in a particular clinic. The increased efficiencies arise from reduction in setup time for ancillary 4D equipment (respiratory bellows/reflector-camera), (re-)positioning of the equipment, faster acquisition times, and elimination of manual sorting.
- Stitching artifacts that may be present on 4D-CT images are greatly reduced on 4D-MR images. However, in extreme cases of inconsistent breathing patients, respiratory motion inconsistencies can result in a slight blur on 4D-MR images.

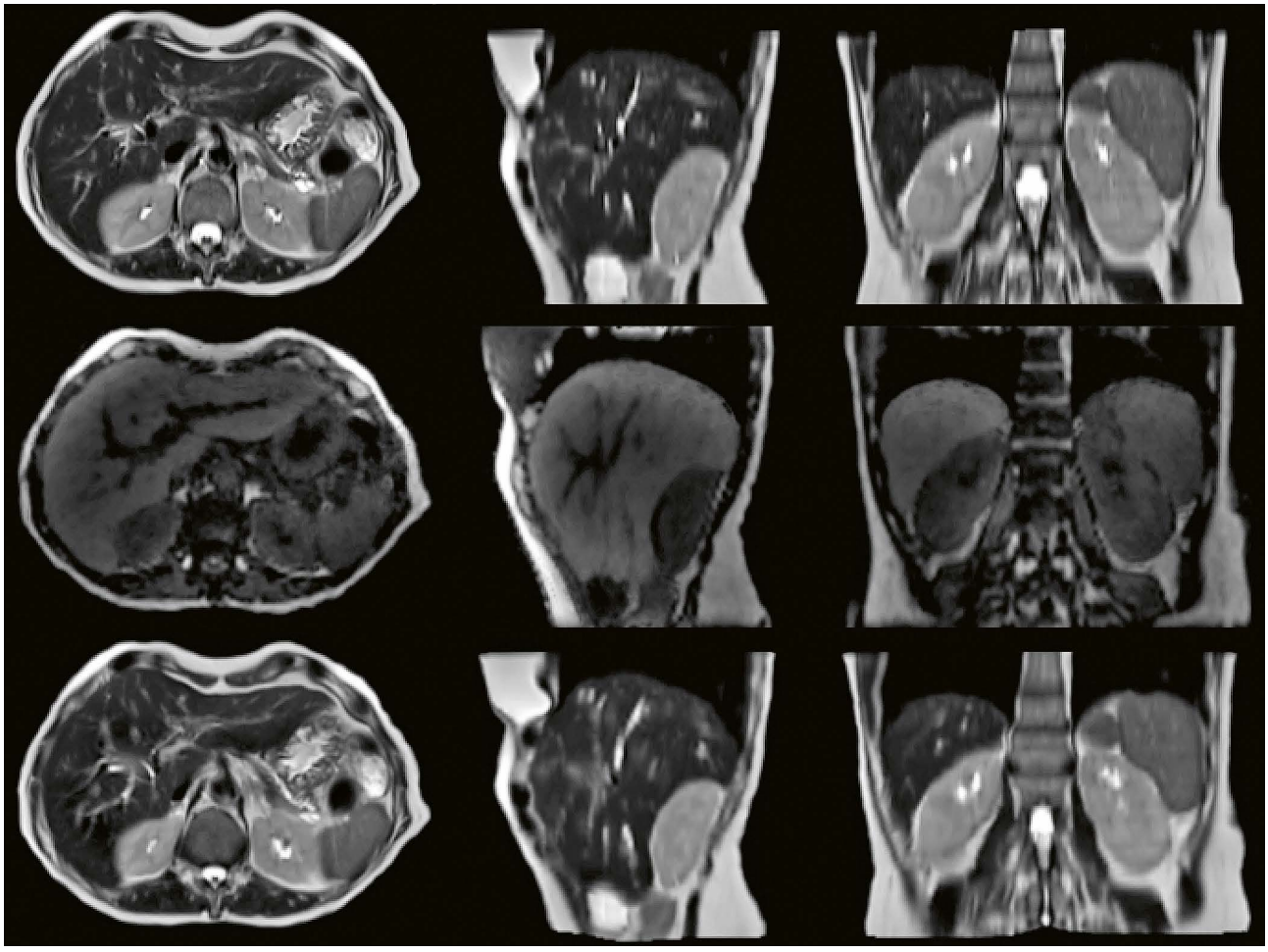

8 Demonstration of using 4D-MRI as a vehicle. Respiratory-triggered T2 TSE images acquired at end expiration (top row) are transformed to a mid-position anatomical state (middle row) using 4D-MRI and deformable image registration. This process permits image contrasts to be obtained at one respiratory phase more favorable for acquisition, and then transformed to another phase more favorable for treatment delivery (bottom row).

- Similar to 4D-CT, the motion waveform derived from the 4D-MR acquisition, and its Fourier transform, can be used to judge whether a given patient may be a candidate for respiratory-gated treatment delivery.
- VIBE interpolation can contribute to blurring along the slab-select direction, which can be reduced by increasing the number of partitions acquired within the slab. Slice partial Fourier can be employed to maintain a high navigator sampling rate in these cases.
- Metal[1] and plastic stents do not appear to significantly obscure 4D-MR image quality.
- Administration of exogenous contrast agents can obscure some structures on non-fat-suppressed T1-weighted 4D-MRI. However, this can be rectified by switching to a 4D-MRI Dixon FLASH acquisition.

The optimal image contrast and timing of the 4D-MRI acquisition within the MR simulation exam may be disease specific. The present 4D-MRI method permits switchable FLASH, FISP, TrueFISP, and PSIF modes, permitting tailoring of 4D image contrast on a tumor-specific basis. Additional studies are planned to determine the optimal 4D-MRI contrast and timing for each cancer site.

References

1 Keall PJ, Mageras GS, Balter JM, Emery RS, Forster KM, Jiang SB, Kapatoes JM, Low DA, Murphy MJ, Murray BR, Ramsey CR, Van Herk MB, Vedam SS, Wong JW, Yorke E. The management of respiratory motion in radiation oncology report of AAPM task group 76. Med Phys 2006; 33:3874-3900.

2 Goldstein SD, Ford EC, Duhon M, McNutt T, Wong J, Herman JM. Use of respiratory-correlated four-dimensional computed tomography to determine acceptable treatment margins for locally advanced pancreatic adenocarcinoma. Int J Radiat Oncol Biol Phys 2010: 597-602.

3 Njeh CF. Tumor delineation: The weakest link in the search for accuracy in radiotherapy. J Med Phys 2008; 33:136-140.

4 Blackall JM, Ahmad S, Miquel ME, McClelland JR, Landau DB, Hawkes DJ. MRI-based measurements of respiratory motion variability and assessment of imaging strategies for radiotherapy planning. Phys Med Biol 2006; 51:4147-4169.

5 Von Siebenthal M, Szekely G, Gamper U, Boesiger P, Lomax A, Cattin Ph. 4D MR imaging of respiratory organ motion and its variability. Phys Med Biol 2007; 52:1547-1564.

6 Tokuda J, Morikawa S, Haque HA, Tsukamoto T, Matsumiya K, Liao H, Masamune K, Dohi T. Adaptive 4D MR Imaging using Navigator-Based Respiratory Signal for MRI-Guided Therapy. Mag Reson Med 2008; 59:1051-1061.

7 Cai J, Chang Z, Wang Z, Segars WP, Yin FF. Four-dimensional magnetic resonance imaging (4D-MRI) using image-based respiratory surrogate: A feasibility study. Med Phys 2011; 38:6384-6394.

8 Hu Y, Caruthers SD, Low DA, Parikh PJ, Mutic S. Respiratory amplitude guided 4-dimensional magnetic resonance imaging. Int J Radiat Oncol Biol Phys 2013; 86:198-204.

9 Tryggestad E, Flammang A, Han-Oh S, Hales R, Herman J, McNutt T, Roland T, Shea SM, Wong J. Respiration-based sorting of dynamic MRI to derive representative 4D-MRI for radiotherapy planning. Med Phys 2013; 40:051909-1 – 051909-12.

10 Celicanin Z, Bieri O, Preiswerk F, Cattin P, Scheffler K, Santini F. Simultaneous Acquisition of Image and Navigator Slices using CAIPIRINHA for 4D MRI. Mag Res Med 2015; 73:669-676.

11 Du D, Caruthers SD, Glide-Hurst C, Low DA, Li HH, Mutic S, and Hu Y. High-Quality T2- Weighted 4-Dimensional Magnetic Resonance Imaging for Radiation Therapy Applications. Int J Radiat Oncol 2015; 92:430–437.

12 Stemkens B, Tijssen RHN, de Senneville BD, Heerkens HD, van Vulpen M, Lagendijk JJW, and van den Berg CAT. Optimizing 4-dimensional magnetic resonance imaging data sampling for respiratory motion analysis of pancreatic tumors. Int J Radiat Oncol Biol Phys 2015; 91:571–8.

13 Deng Z, Pang J, Yang W, Yue Y, Sharif B, Tuli R, Li D, Fraass B, and Fan Z. Four- dimensional MRI using three-dimensional radial sampling with respiratory self-gating to characterize temporal phase-resolved respiratory motion in the abdomen. Magn Reson Med 2015;

14 Feng L, Axel L, Chandarana H, Block KT, Sodickson DK, Otazo R. XD-GRASP: Golden-angle radial MRI with reconstruction of extra motion-state dimensions using compressed sensing. Magn Reson Med 2016; 75:775–88.

15 Mickevicius NJ, Paulson ES. Investigation of undersampling and reconstruction algorithm dependence on respiratory correlated 4D-MRI for online MR-guided radiation therapy. Phys Med Biol 2016; (in press)

16 Fessler JA, Sutton BP. Nonuniform fast Fourier transforms using min-max interpolation. IEEE Trans Sig Proc 2013; 51:560-574.

17 Krämer M, Biermann J, Reichenbach JR. Intrinsic correction of system delays for radial magnetic resonance imaging. Magn Reson Imag 2015; 33:491–6

18 Benkert T, Feng L, Sodickson DK, Chandarana H, Block KT. Free-breathing volumetric fat/water separation by combining radial sampling, compressed sensing, and parallel imaging. Magn Reson Med 2016; (in press)

19 Wolthaus JW, Sonke JJ, van Herk M, Belderbos JS, Rossi MM, Lebesque JV, Damen EM. Comparison of different strategies to use four-dimensional computed tomography in treatment planning for lung cancer patients. Int J Radiat Oncol Biol Phys 2008; 70:1229-38.

[1]The MRI restrictions (if any) of the metal implant must be considered prior to patient undergoing MRI exam. MR imaging of patients with metallic implants brings specific risks. However, certain implants are approved by the governing regulatory bodies to be MR conditionally safe. For such implants, the previously mentioned warning may not be applicable. Please contact the implant manufacturer for the specific conditional information. The conditions for MR safety are the responsibility of the implant manufacturer, not of Siemens.

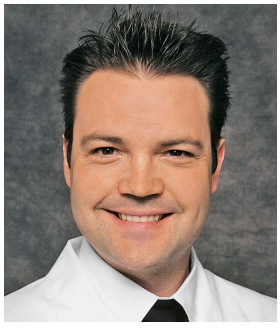

Contact

Eric Paulson
Ph.D., DABR Assistant Professor and Senior Medical Physicist
Radiation Oncology, Radiology, and Biophysics
Medical College of Wisconsin
Radiation Oncology
8701 Watertown Plank Road
Milwaukee, WI 53223
USA
epaulson@mcw.edu

First Experience of 4D-MRI for Abdominal Radiotherapy Planning

Andrew Oar[1,2]; Gary Liney[1,2,3,4]; Robba Rai[1,2,3]; Shrikant Deshpande[1,3,4]; Li Pan[5]; Meredith Johnston[1]; Michael Jameson[1,2,3,4]; Shivani Kumar[1]; Mark Lee[1,2]

[1] Liverpool and Macarthur Cancer Therapy Centre, Sydney, Australia
[2] South West Sydney Clinical School, University of New South Wales, Sydney, Australia
[3] Ingham Institute for Applied Medical Research, Sydney, Australia
[4] Centre for Medical Radiation Physics, University of Wollongong, NSW, Australia
[5] Siemens Healthineers, Baltimore, MD, USA

Introduction

Four-dimensional (4D) computed tomography (CT) is widely used in radiation therapy (RT) and remains the current standard for motion evaluation during RT planning. The use of 4D-CT allows the delineation of an internal target volume (ITV)[ICRU RPT62]. Unfortunately, 4D-CT uses additional radiation exposure to the 3D planning CT, and has limitations in soft tissue contrast. Magnetic resonance imaging (MRI) offers superior soft tissue definition to CT and therefore has potential significant advantages when implemented during the radiotherapy process. The integration of MRI into the radiotherapy planning and treatment pathway has been rapid with developments in MRI-simulation [1] and real-time MR guidance [2].

Attempts to replace 4D-CT with an MRI counterpart have been made for over a decade. Until recently, imaging physiological motion using MRI has involved unacceptable trade-offs between spatial and temporal resolution [3]. The majority of published literature has utilized 2D cine [4] sequences, which have been acquired in two orthogonal planes or in combination with a 3D volume as a surrogate for real-time 3D acquisition. Nonetheless efforts have been made utilizing 2D cine for adaptive radiotherapy planning [5]. Respiratory based sorting is another method with variable success [6]. Poor respiratory correlation can be problematic and incomplete binning can lead to gaps in data, which can be overcome by increasing scan time or utilizing a two-pass method [4, 7]. A combination of 2D-MRI and phase binning has yielded conflicting results [8] with noticeable phase mismatch and significant cycle-to-cycle motion variation. Both tumor deformation and motion out of plane is problematic with these methods. A much better approach is to acquire time-resolved 3D volume acquisitions, and this is now possible with sufficient resolution and image quality to be of clinical interest.

Here we present our initial findings using a prototype 4D-MRI technique based on a T1-weighted (T1w) 3D gradient echo (VIBE) sequence[1]. This uses a continuous radial acquisition and retrospective binning of respiratory phases, to generate 3D high-resolution images from different parts of the respiratory cycle (Siemens Healthcare, Erlangen, Germany). 4D-MRI combined with the recent interest in replicating dosimetry calculations in MRI may further abrogate the need for CT-simulation.

[1] *WIP, the product is currently under development and is not for sale in the US and in other countries. Its future availability cannot be ensured.*

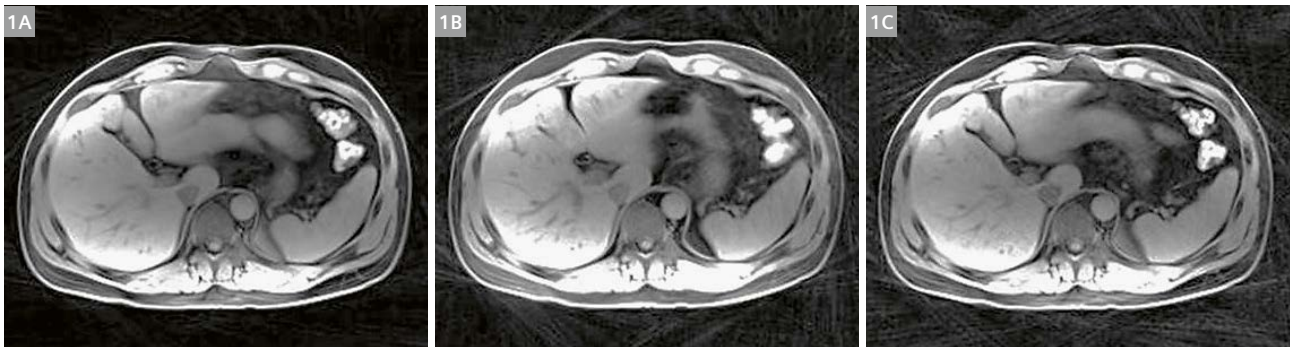

1 The radial streak artifact seen with three **(1A)**, five **(1B)** and ten **(1C)** bins. All images using 2000 radial views.

Initial experience

MRI was performed utilizing a customized vacuum bag (BlueBAG, Elekta, Stockholm, Sweden) for immobilization and a flat wing board (MTWB09 Wingboard, CIVCO Medical Solutions, Orange City, IA, USA) with arms above the head. All MR imaging was performed on the departmental radiotherapy dedicated 3T wide-bore MRI (MAGNETOM Skyra, Siemens Healthcare, Erlangen, Germany) on a flat-bed insert (CIVCO Medical Solutions, Orange City, IA, USA) with a 32-channel posterior in-table coil and 18-channel flexible array coil. Sequences included T2 HASTE gated with phase navigation, breath-hold T1 VIBE and multiphasic (arterial, venous and transitional phases) breath-hold T1 VIBE enhanced with 0.1 ml/kg Gadobutrol (Gadovist, Bayer, Leverkusen, Germany). Additionally all volunteers and patients underwent the prototype T1-3D gradient echo with radial self-gating (Siemens Healthcare, Erlangen, Germany) 4D-MRI sequence. *k*-space sampling is performed using a stack-of-stars trajectory with golden angle increment [9]. The sequence uses data from the centre of *k*-space to extract a surrogate respiration trace, which permits self-gating.

The sequence was first optimized on two healthy volunteers to qualitatively compare image quality of the liver and evaluate the trade-off between acquisition time and artifacts. Changes in protocol were investigated to examine the effects on image quality including number of radial views (1500, 2000 and 3300) and uniform bins (3, 5 and 10). Image quality was assessed by two radiation oncologists and an experienced MRI radiographer (ML, AO, RR). When comparing the number of uniform bins, it was observed that for three bins there were fewer radial streak artefacts with overall good image quality, however the degree of motion of the liver was not completely captured. In contrast, ten bins captured a greater degree of motion but suffered from a greater degree of radial streak artefacts that impacted the ability to delineate organ borders for RT planning (see Fig. 1). However, five respiratory bins reproduced the liver motion whilst maintaining optimal image quality for contouring, and therefore five bins was selected for patient image acquisition. Two thousand radial views provided the best trade-off between time and radial streak artifacts. The acquisition time using these parameters was approximately five minutes. Increasing the number of radial views beyond this increased the acquisition time, which is not ideal for this patient cohort, without demonstrable benefits in image quality.

The efficacy of 4D-MRI with and without abdominal compression has been tested in ten volunteers (see Fig. 2). Figure 2 demonstrates that a high image quality can be

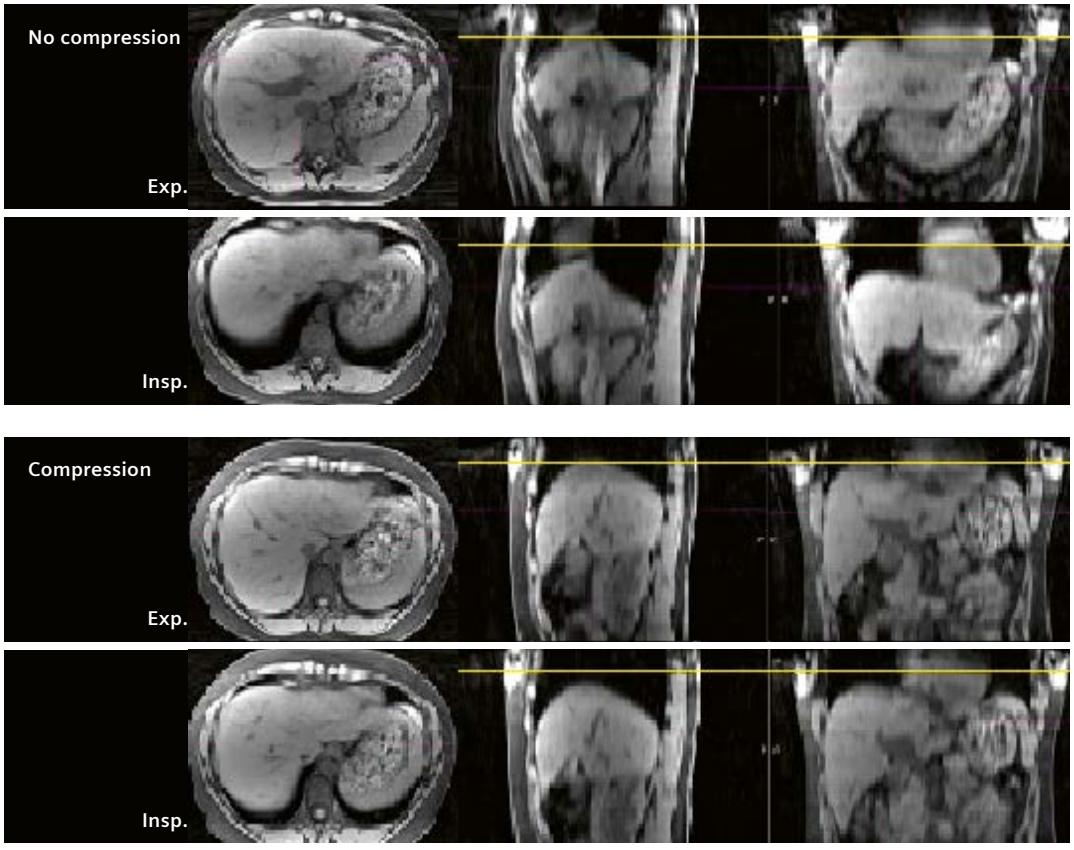

2 Feasibility of 4D-MRI and abdominal compression has been shown in ten healthy volunteers.

Exp.: Expiration

Insp.: Inspiration

Level of diaphragm in expiration is represented by yellow line. These images were acquired in axial plane.

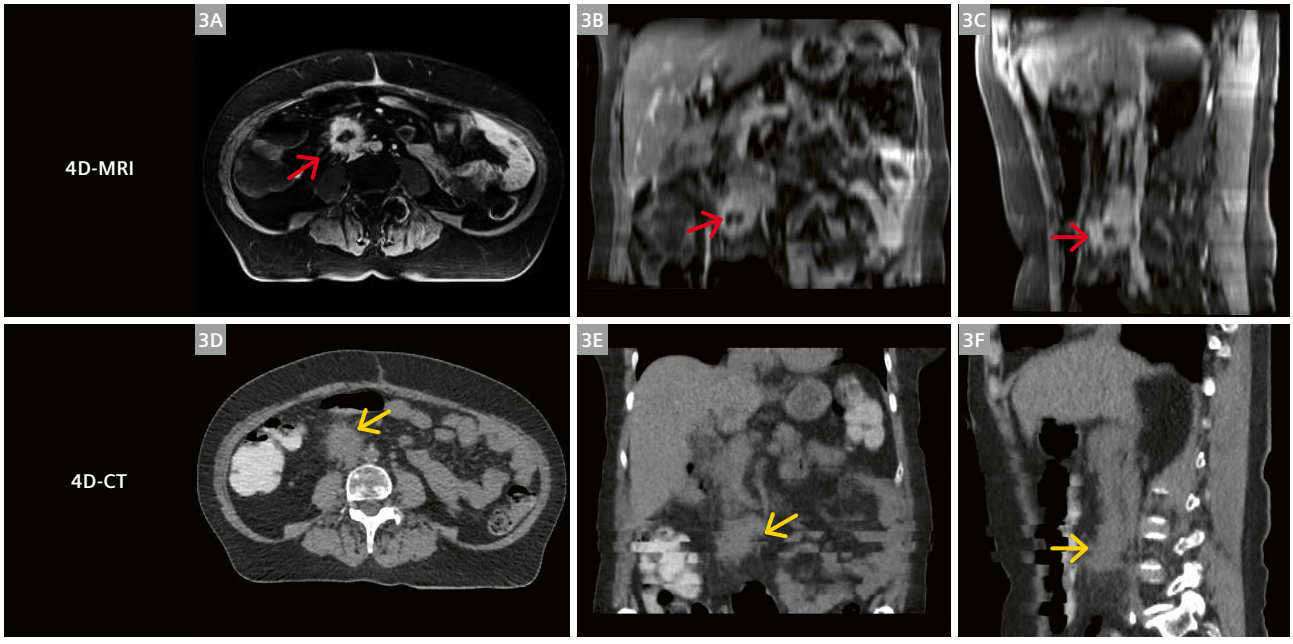

3 Comparison of 4D-MRI and 4D-CT in a patient with solitary nodal recurrence of colorectal cancer receiving high dose radiotherapy. In this case 4D-CT failed due to step artifacts (yellow arrows) over the area of interest. Gadolinium enhanced 4D-MRI provided excellent soft tissue delineation (red arrows) and accurate motion visualization.

maintained whilst obtaining physiological motion information both with and without abdominal compression. For the volunteer study, the amplitude of movement of liver and volume of lung below the T10 vertebral level has been recorded for both compression and no compression. Volunteer study results are pending for publication.

This prototype 4D-MRI sequence has demonstrated encouraging results and as a self-gating technique it is very promising. Superior soft tissue delineation and reduced radiation exposure may mean 4D-MRI is a suitable replacement for 4D-CT. Figure 3 demonstrates a sample case where 4D-CT suffered from artifacts due to inconsistent breathing rate throughout image acquisition and poor signal from the respiratory trace. In this case the step artifacts impacted the delineation of the tumor volume, introducing uncertainty for treatment. 4D-MRI in comparison provided greater soft tissue contrast (Fig. 3A) with minimal artifacts allowing greater confidence in contouring the tumor volume. The clinical outcome of the first ten patients is pending for presentation and publication.

Future direction

Local area health research and ethics board approval has been obtained for direct comparison of 4D-CT to 4D-MRI in patients receiving upper abdominal radiotherapy. Recruitment to this study is ongoing with ten patients recruited to date. 4D-CT will be directly compared to 4D-MRI in parameters such as amplitude of movement and image quality. Artifact, noise, and tumor edge detection will be graded on a four-point scale as seen in Table 1 for both 4D-CT and 4D-MRI. This scoring system has been utilized previously [10]. Tumors will be contoured on maximal inspiratory and expiratory images and directly compared to 4D-CT. Clinical data from this research project has been presented at ESTRO 37.

Gadoxetate sodium (Primovist, Bayer, Leverkusen, Germany) has shown exceptional diagnostic potential in patients with both primary and metastatic liver tumors [11, 12]. The slow excretion of Primovist by hepatocytes is likely to facilitate superior contrast information during 4D-MRI scanning. We intend to explore Primovist in patients with primary and secondary liver tumors during 4D-MRI and we hypothesise that despite the longer acquisition time of 4D-MRI, the benefits of contrast can be maintained.

MRI linear accelerators are likely to play an increasing role within the radiotherapy treatment paradigm. Adaptive 4D-MR guidance is now clinically achievable [5, 13]. As the quality of 4D-MR imaging improves, and the integration of MR into radiotherapy delivery systems is refined, clinician's confidence regarding real-time tumor position and movement may be further enhanced. Those patients where volumetric acquired 4D-MRI at simulation is seen to accurately represent movement of the region of interest may be the greatest beneficiaries of an MRI linear accelerator. With further refinement and rapidly growing MRI linear accelerator interest, online volumetric acquired 4D-MRI is

Score	1	2	3	4
Tumor edge detection	Tumor edge clearly defined	Tumor edge slightly blurred, not impairing definition of tumor boundary	Considerable blurring of tumor edge impacting on accurate definition of tumor boundary	Significant blurring of tumor edge, definition of tumor boundary not achievable
Artifacts	No artifacts	Little artifact not impairing image quality	Considerable artifact impacting evaluation of anatomical structures	Extreme artifacts obscuring delineation of anatomical structures
Image noise	Minimal noise	Little noise not impairing diagnostic image quality	Considerable noise impacts the evaluation of anatomical structures	Extreme noise obscuring delineation of anatomical structures
Overall image quality	Very good image quality	Fair image quality not impairing the delineation of structures	Impaired image quality that may lead to incorrect delineation	Structures not definable

Table 1: Scoring system for tumor edge detection, artifact, image noise and overall image quality.

clinically feasible. Volumetric 4D-MRI will significantly alter radiotherapy treatment delivery in liver, bowel, pancreas, heart, lymph node and prostate where real-time accuracy of soft tissues is pivotal.

Acknowledgments

The authors wish to thank Dr. Benjamin Schmitt at Siemens Healthineers for the development of this volumetric acquired 4D-MRI sequence (Siemens Healthcare, Erlangen, Germany) and ongoing input into this research project.

The statements by Siemens' customers presented here are based on results that were achieved in the customer's unique setting. Since there is no 'typical' hospital and many variables exist (e.g., hospital size, case mix, level of IT adoption), there can be no guarantee that other customers will achieve the same results.

References:

1 Liney, G.P. and M.A. Moerland. Magnetic resonance imaging acquisition techniques for radiotherapy planning. Seminars in radiation oncology. 2014. Elsevier.
2 Raaymakers, B., et al., First patients treated with a 1.5T MRI-Linac: clinical proof of concept of a high-precision, high-field MRI guided radiotherapy treatment. Physics in Medicine & Biology, 2017. 62(23): p. L41.
3 von Siebenthal, M., et al., 4D MR imaging of respiratory organ motion and its variability. Physics in medicine and biology, 2007. 52(6): p. 1547.
4 Tryggestad, E., et al., Respiration-based sorting of dynamic MRI to derive representative 4D-MRI for radiotherapy planning. Medical Physics, 2013. 40(5): p. 051909-n/a.
5 Kontaxis, C., et al., Towards fast online intrafraction replanning for free-breathing stereotactic body radiation therapy with the MR-linac. Phys Med Biol, 2017. 62(18): p. 7233-7248.
6 Du, D., et al., High-quality T2-weighted 4-dimensional magnetic resonance imaging for radiation therapy applications. International Journal of Radiation Oncology* Biology* Physics, 2015. 92(2): p. 430-437.
7 Liu, Y., et al., T2 weighted four dimensional magnetic resonance imaging with result driven phase sorting. Medical physics, 2015. 42(8): p. 4460-4471.
8 Park, S., et al., Simultaneous tumor and surrogate motion tracking with dynamic MRI for radiation therapy planning. Phys Med Biol, 2017.
9 Winkelmann, S., et al., An optimal radial profile order based on the Golden Ratio for time-resolved MRI. IEEE transactions on medical imaging, 2007. 26(1): p. 68-76.
10 Kumar, S., et al., Feasibility of free breathing Lung MRI for Radiotherapy using non-Cartesian k-space acquisition schemes. The British journal of radiology, 2017. 90(1080): p. 20170037.
11 Hammerstingl, R., et al., Diagnostic efficacy of gadoxetic acid (Primovist)-enhanced MRI and spiral CT for a therapeutic strategy: comparison with intraoperative and histopathologic findings in focal liver lesions. European radiology, 2008. 18(3): p. 457.
12 Ichikawa, T., et al., Detection and characterization of focal liver lesions: a Japanese phase III, multicenter comparison between gadoxetic acid disodium-enhanced magnetic resonance imaging and contrast-enhanced computed tomography predominantly in patients with hepatocellular carcinoma and chronic liver disease. Investigative radiology, 2010. 45(3): p. 133-141.
13 PRNewswire, Early Clinical Data Suggests Nearly 2X Prolonged Median Survival for Inoperable, Locally Advanced Pancreatic Cancer with MRIdian MR-Guided Radiation Therapy. 2017.

Contact

Dr. Andrew J. Oar
Liverpool Cancer Therapy Centre
Locked Bag 7103
Liverpool BC 1871, NSW, Australia
andrew.oar@health.nsw.gov.au

Cardiotoxicity in Cancer Therapy – the Role of Cardiovascular Magnetic Resonance

Christian P. Houbois[1,2]; Paaladinesh Thavendiranathan, MD SM[1,3,4]; Bernd J. Wintersperger, MD EBCR FAHA[1,2]

[1] Department of Medical Imaging, Peter Munk Cardiac Centre, University Health Network, Toronto, Canada
[2] Department of Medical Imaging, University of Toronto, Toronto, Canada
[3] Division of Cardiology, Peter Munk Cardiac Centre, University Health Network, Toronto, Canada
[4] Department of Medicine, University of Toronto, Toronto, Canada

Introduction

Cardiovascular magnetic resonance (CMR) imaging has become a mainstay in the assessment of various cardiac pathologies including ischemic and non-ischemic cardiomyopathies. Beyond the sole aspect of functional deterioration, CMR has convincingly demonstrated to provide further information on the underlying cause contributing sufficient information to narrow the differential diagnosis. Furthermore, insight into the myocardial composition may shed light into the risk prediction of certain diseases and may also allow monitoring of therapeutic interventions and their effects on the heart.

In recent years, the link between tumor therapies and cardiac disease has gained substantial attention and is currently focus of multiple ongoing large-scale studies. With the continuous improvement of survival rates of patients with various malignancies, potential detrimental effects on cardiac function and outcome including increased morbidity and mortality has become the center of such investigations. Outside study settings, major centers with large oncology and cardiac programs have started to establish Cardio-Oncology clinics, in order to help guide oncologists in their treatment planning in patients with pre-existing cardiac disease as well as taking care of patients with potential tumor therapy regimen related cardiovascular effects and potential development of heart failure (HF).

Tumor therapy and heart failure

Todays' therapy regimens in patients with malignant neoplasms may be based on surgical approaches, local or extended radiation therapy (RT) as well as systemic tumor therapies or a combination thereof. While surgical approaches and RT generally affect structures within the application field, systemic therapies may not only result in anti-tumor effects but may also affect otherwise normal body tissue, including the heart. Such negative effects of tumor-related therapy on the heart are generically referred to as cardiotoxicity. The known impact of anthracycline (AC) related tumor therapy possibly resulting in HF may often also be referred to as anthracycline induced heart failure (AIHF).

While modern personalized medicine approaches result in the continuous development of new anti-tumor drugs amongst different drug classes, AC still remain a mainstay of modern tumor therapy regimens. They are commonly used in treatment of breast malignancies, sarcomas and also hematologic malignancies. It is estimated that up to 60% of childhood cancer survivors have been exposed to AC therapy regimens and/or chest radiation [1; 2].

Up to ~20% of patients undergoing AC based tumor therapy (with or without combination therapy) may experience AC related cardiotoxicity with the development of HF. The incidence generally increases with increasing cumulative AC dosing. Specifically designed studies employing short interval imaging (echocardiography) based monitoring of the ventricular function, the vast majority (up to 98%)

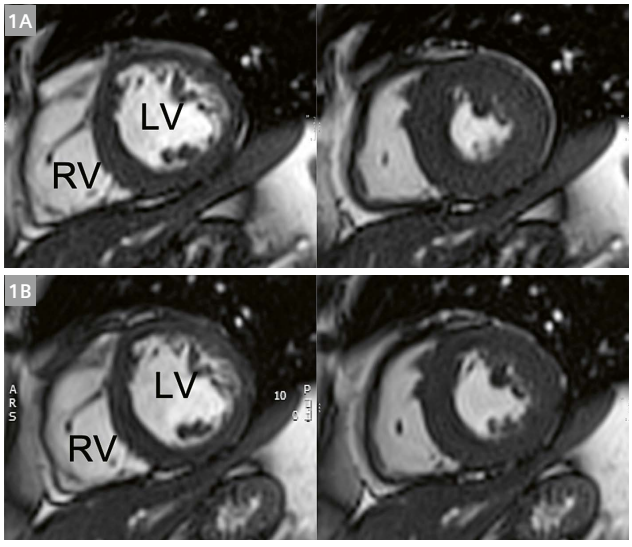

1 Standard cine imaging in a patient with breast cancer **(1A)** prior to chemotherapy and **(1B)** one year after the end of anthracycline/trastuzumab combination therapy. Images demonstrate almost identical slice positioning (Cardiac Dot Engine) in diastole (left), but already visually a clear reduction in global ejection fraction is seen in systolie (right). The ejection fraction had dropped by ≥ 10% to < 50%.

LV = left ventricle; RV = right ventricle

of cardiotoxicity related HF developed either during the systemic cancer therapy or within one year after the end of therapy [3] (Fig. 1). Among patients experiencing such detrimental effects, the vast majority of patients will not entirely recover their cardiac function despite initiation of HF therapy [3]. The risk of cardiac events in this population is significantly increased and in case of confirmed AIHF, mortality may exceed 50% within two years.

Anthracyclines (e.g. doxorubicin, epirubicin) have been known from early use to potentially cause HF and still remain the drug class most commonly related to HF. However, also other drug classes may result in negative cardiovascular effects or may increase the risk of HF in combination with AC based therapy schemes. These classes include monoclonal anti-bodies (MAB) such as trastuzumab, tyrosine kinase inhibitors (TKI) as well as immune checkpoint inhibitors (ICI).

Meanwhile, guidelines have been developed helping to identify patient populations who are specifically at risk for cardiotoxicity related HF [4]. In general, the risk is specifically depending on the dosage of AC therapy, but also the amount of potentially applied additional radiation, potential cardiovascular risk factors as well as the combination of certain drug classes (e.g. anthracycline-trastuzumab combination therapy) [4].

Of specific interest is also the class of aforementioned ICI's, a group of agents that has generally demonstrated lower rates of cardiotoxicity, but that may specifically cause autoimmune myocarditis in rare instances resulting in high complication rates [5].

Cardiovascular magnetic resonance and cardiotoxicity

The breadth of techniques available in CMR for assessment of cardiac function, myocardial deformation and myocardial tissue characterization makes it a potentially ideal tool for assessment and monitoring of patients with increased risk of developing cancer therapy related cardiotoxicity.

Functional cardiac imaging

Today's definitions of cardiotoxicity are almost exclusively based on the assessment of the left ventricular (LV) ejection fraction (EF). As such, the known high accuracy and precision of CMR in the assessment of cardiac volume and function is perfectly suited to guide clinicians according to current definitions of cardiotoxicity [6]. With little variation, published criteria of cardiotoxicity follow a change in LVEF with main cut-offs at a drop of ≥ 10% to under 50% or 55%/53% respectively (Fig. 1) [7–9]. More subtle changes in LVEF (≥ 5%) should be considered as possibly related to cardiotoxicity in patients with symptoms of heart failure (HF) [8]. However, it is important to keep in mind that such thresholds are generally based on echocardiography or multigated acquisition (MUGA) radionuclide ventriculography, modalities that generally suffer from a higher inter-scan and inter-observer variability. Although there is no separate cut-off criterion based on CMR, recent study data suggests that MUGA results may potentially result in misclassification of patients [10].

In any of the above LVEF based definitions of cardiotoxicity, proper baseline assessment and follow scans are required; single time assessment of the cardiac function would not allow adequate judgement. In addition to standard imaging approaches, CMR may play an increasingly important role in the monitoring of such patients. Various clinical experiences report cases where echocardiography based functional assessment would have missed a significant drop in LVEF.

However, from decades of imaging experience it is known that LVEF changes may only occur as a delayed relation to local changes. Therefore, assessment of myocardial deformation may provide a more sensitive and earlier insight into myocardial changes. In the field of echocardiography, the application of speckle tracking echocardiography (STE) has pushed the use of strain imaging towards clinical use including assessment of cardiotoxicity. CMR offers various techniques for myocardial deformation imaging including myocardial tagging, sensitivity encoding (SENC) and displacement encoding with stimulated echoes (DENSE). However, such techniques have never been established on a larger scale in clinical routine CMR.

Most recently, developments of techniques that allow assessment of myocardial strain in routinely acquired cine balanced steady state free precession (bSSFP) data sets have opened a whole new avenue of myocardial deformation assessment. The different available techniques rely either on feature tracking algorithms or employ motion correction techniques for calculation of deformation in cine bSSFP [11–15]. Especially, prototype deformation map-based techniques such as TrufiStrain[1] (Siemens Medical Imaging Technologies, Princeton, US) demonstrated promising and highly reproducible results compared to accepted standard of reference such as myocardial tagging (Figures 2–4) [12; 14]. In the application of cardiotoxicity evaluation, CMR based strain has also demonstrated great promise aiming at early detection of changes.

Tissue characterization

Qualitative tissue characterization techniques such as T2-weighted imaging or Late Gadolinium Enhancement (LGE) imaging have long played a role in the assessment of various cardiomyopathies and inflammatory changes such as myocarditis [16, 17]. However, the use of LGE imaging in assessment of cardiotoxicity appears limited. As an

[1] *WIP, the product is currently under development and is not for sale in the US and in other countries. Its future availability cannot be ensured.*

exception, LGE may play a role in assessment of possible autoimmune myocarditis/pericarditis which may occur during ICI therapy and is considered a bad prognostic marker (Fig. 5).

As a potential new marker of cardiotoxicity related tissue level changes, cardiac relaxometry techniques such as T1 mapping, T2 mapping as well as derived markers such as extracellular volume fraction (ECV) have been proposed and evaluated in various experimental and clinical studies predominately focused on the effects of anthracycline therapy.

In animal studies, the repeated application of anthracycline doses lead to a continuous increase in native T1 values over the course of 12–14 weeks while other studies have demonstrated that T2 values are increased in the early phase (~4–6 weeks) suggesting myocardial edema [18, 19]. However, the later study also demonstrated that despite elevated T2 values in early stages, ECV was not elevated until later stages. A possible explanation of elevated T2 and normal ECV might be the occurrence of intracellular edema.

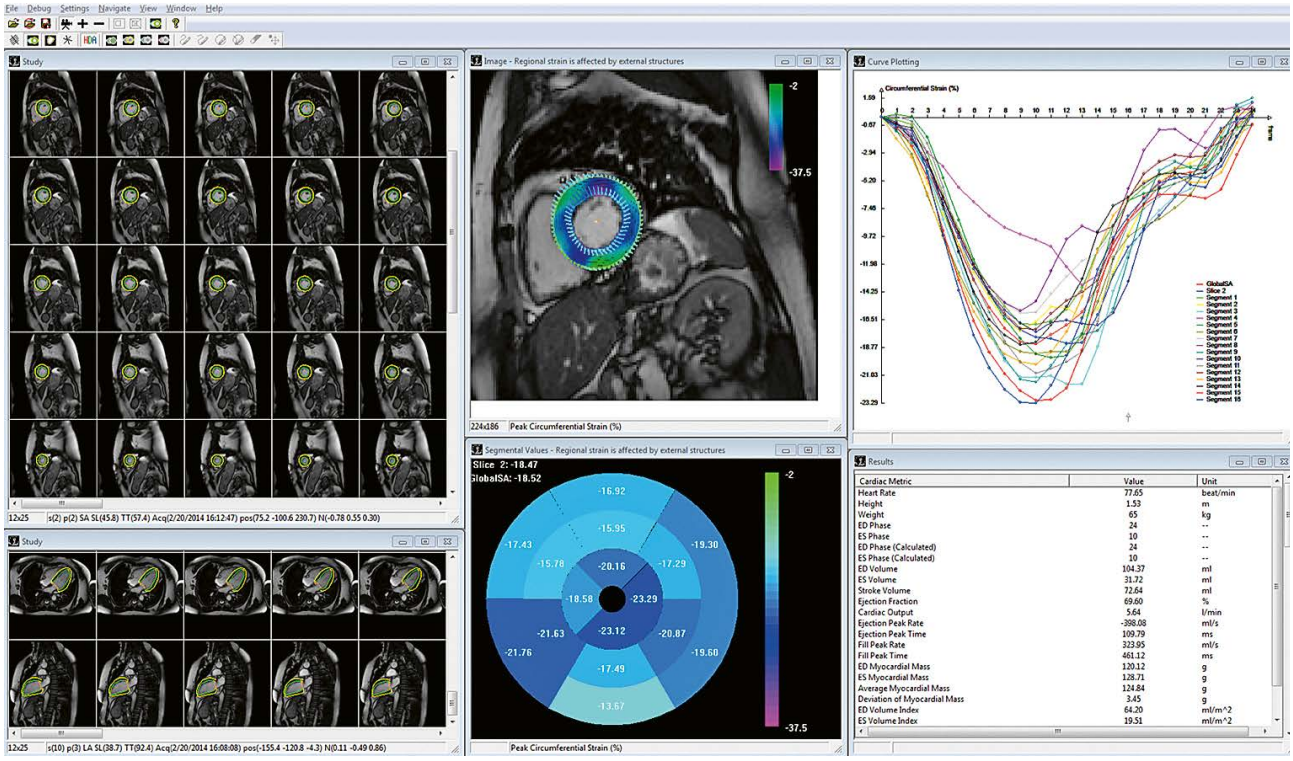

2 Standard screen overview of TrufiStrain[1], a prototype software for cine derived strain analysis. The left part of the layout demonstrates the fully automated (short axis) and semiautomated (long axis) segmentation of the endo- and epicardial contours. The center part highlights a visual overlay of strain data onto cine data as well as a bullseye plot of AHA segment strain results. On the right, a visual display of the strain curves (circumferential in this case) for all 16 AHA segments as well as the entire slice with additional results of automated functional analysis at the bottom.

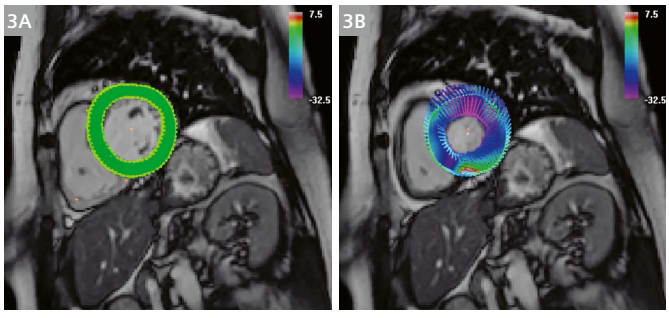

3 Single short axis slice in a healthy volunteer in **(3A)** diastole and **(3B)** systole with time point related strain result overlay; the colored lines on the systolic display visualize the direction and magnitude of endo- as well as epicardial motion from diastole to systole.

Changes in myocardial T1 as well as ECV values have also been demonstrated in patient studies. As in many other cardiomyopathies, pre-contrast T1 values as well as ECV increase after chemotherapy, likely related to development of interstitial fibrosis [20]. However, hyperacute reactions within the myocardium may result in an initial T1 value decrease possible indicating worse outcome [21]. Currently, there is still limited data from prospective longitudinal studies available to clearly describe potential differences in quantitative cardiac relaxometry in patients with and without development of functional deterioration after chemotherapy. Similar to functional analysis, likely sequential longitudinal imaging, including pre-therapy assessment of T1 and T2 data, is required to identify and differentiate true tissue changes from imaging related variability. A possibly even more promising use of cardiac relaxometry techniques may again relate to patients under ICI therapy with possible autoimmune myocarditis changes (Fig. 5). Similar to recent recommendations regarding the diagnosis of myocarditis in general, changes in quantitative tissue markers may help earlier and more accurate diagnosis [22].

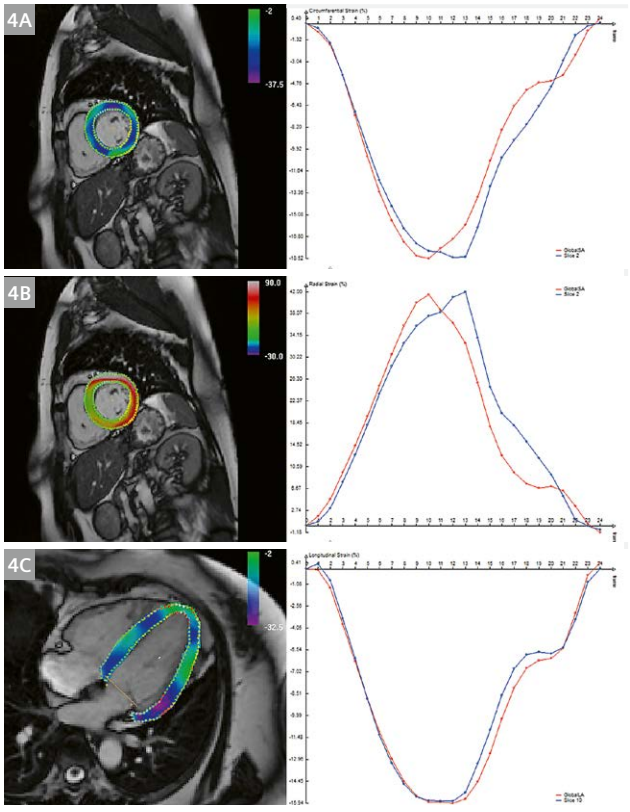

4 Demonstration of three major directions/orientations of myocar dial strains typically evaluated; **(4A)** circumferential strain, **(4B)** radial strain and **(4C)** longitudinal strain. As strain is a measure of length changes in relation to an applied force, the typical shortening in evaluation on circumferential and longitudinal strain result in negative strain values while the thickening during systole results in positive values for radial strain.

Conclusion

While the playing field of potentially cardiotoxic tumor therapy generally hasn't substantially changed, decades of study results have helped to better understand risk factors and relationships between tumor therapy and cardiac failure. Furthermore, there is a much-increased awareness of the potential interaction between tumor therapy and heart failure resulting in the new subspecialty of 'Cardio-Oncology'. While imaging has long played a role in cancer patients undergoing chemotherapy, CMR is rapidly entering the field and is more frequently being employed. The accuracy and precision of CMR functional assessment proves beneficial in early identification of functional deterioration. Added information might be gathered from cine CMR based strain analysis and quantitative myocardial tissue markers (T1/T2/ECV mapping). However, the timing and specific application of CMR during the course of cancer therapy, especially in

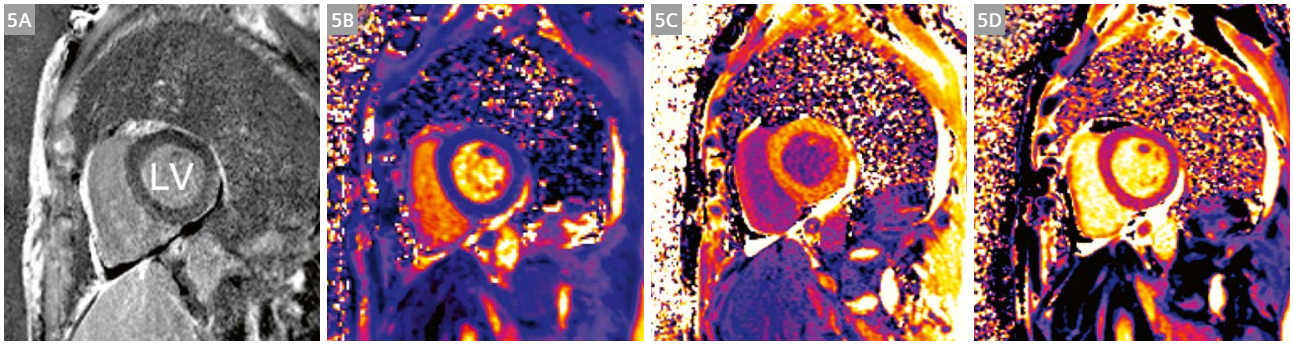

5 Patient undergoing immune checkpoint inhibitor (ICI) cancer therapy with troponin elevation and suspicion of immune myocarditis. While **(5A)** LGE imaging possible demonstrates very faint diffuse enhancement, cardiac relaxometry with T1 and T2-mapping (1.5T) provides further information. **(5B)** T2 mapping reveals a T2 time of 55 ms while **(5C)** pre-contrast T1 values were 1184 ms and **(5D)** post-contrast T1 values 519 ms (0.15 mmol/kg Gadobutrol). Based on the patient's hematocrit the ECV is calculated to 38%.

patients at risk, has yet to be determined. For a better understanding of that role, additional data on the general test-retest variability of such quantitative markers is still required. Furthermore, society guidelines and definitions of cardiotoxicity would need to further extend beyond the sole criteria of cardiac function.

References:

1 Smith LA, Cornelius VR, Plummer CJ et al. (2010) Cardiotoxicity of anthracycline agents for the treatment of cancer: systematic review and meta-analysis of randomised controlled trials. BMC Cancer 10:337.
2 Armenian SH, Hudson MM, Mulder RL et al. (2015) Recommendations for cardiomyopathy surveillance for survivors of childhood cancer: a report from the International Late Effects of Childhood Cancer Guideline Harmonization Group. Lancet Oncol 16:e123-136.
3 Cardinale D, Colombo A, Bacchiani G et al. (2015) Early detection of anthracycline cardiotoxicity and improvement with heart failure therapy. Circulation 131:1981-1988
4 Armenian SH, Lacchetti C, Barac A et al (2017) Prevention and Monitoring of Cardiac Dysfunction in Survivors of Adult Cancers: American Society of Clinical Oncology Clinical Practice Guideline. J Clin Oncol 35:893-911.
5 Escudier M, Cautela J, Malissen N et al. (2017) Clinical Features, Management, and Outcomes of Immune Checkpoint Inhibitor-Related Cardiotoxicity. Circulation 136:2085-2087.
6 Grothues F, Smith GC, Moon JC et al. (2002) Comparison of interstudy reproducibility of cardiovascular magnetic resonance with two-dimensional echocardiography in normal subjects and in patients with heart failure or left ventricular hypertrophy. Am J Cardiol 90:29-34.
7 Schwartz RG, McKenzie WB, Alexander J et al. (1987) Congestive heart failure and left ventricular dysfunction complicating doxorubicin therapy. Seven-year experience using serial radionuclide angiocardiography. Am J Med 82:1109-1118.
8 Seidman A, Hudis C, Pierri MK et al. (2002) Cardiac dysfunction in the trastuzumab clinical trials experience. J Clin Oncol 20:1215-1221.
9 Plana JC, Galderisi M, Barac A et al. (2014) Expert consensus for multimodality imaging evaluation of adult patients during and after cancer therapy: a report from the American Society of Echocardiography and the European Association of Cardiovascular Imaging. J Am Soc Echocardiogr 27:911-939.
10 Huang H, Nijjar PS, Misialek JR et al. (2017) Accuracy of left ventricular ejection fraction by contemporary multiple gated acquisition scanning in patients with cancer: comparison with cardiovascular magnetic resonance. J Cardiovasc Magn Reson 19:34.
11 Lamacie MM, Thavendiranathan P, Hanneman K et al. (2017) Quantification of global myocardial function by cine MRI deformable registration-based analysis: Comparison with MR feature tracking and speckle-tracking echocardiography. Eur Radiol 27:1404-1415.
12 Lamacie MM, Houbois CP, Greiser A, Jolly MP, Thavendiranathan P, Wintersperger BJ (2019) Quantification of myocardial deformation by deformable registration-based analysis of cine MRI: Validation with tagged CMR. Eur Radiol. DOI: 10.1007/s00330-019-06019-9.
13 Keller EJ, Fang S, Lin K et al (2017) The consistency of myocardial strain derived from heart deformation analysis. Int J Cardiovasc Imaging 33:1169-1177
14 Jolly MP, Jordan JH, Melendez GC, McNeal GR, D'Agostino RB, Jr., Hundley WG (2017) Automated assessments of circumferential strain from cine CMR correlate with LVEF declines in cancer patients early after receipt of cardio-toxic chemotherapy. J Cardiovasc Magn Reson 19:59.
15 Barreiro-Perez M, Curione D, Symons R, Claus P, Voigt JU, Bogaert J (2018) Left ventricular global myocardial strain assessment comparing the reproducibility of four commercially available CMR-feature tracking algorithms. Eur Radiol. 10.1007/s00330-018-5538-4.
16 Cummings KW, Bhalla S, Javidan-Nejad C, Bierhals AJ, Gutierrez FR, Woodard PK (2009) A pattern-based approach to assessment of delayed enhancement in nonischemic cardiomyopathy at MR imaging. Radiographics 29:89-103.
17 Friedrich MG, Sechtem U, Schulz-Menger J et al. (2009) Cardiovascular magnetic resonance in myocarditis: A JACC White Paper. J Am Coll Cardiol 53:1475-1487.
18 Hong YJ, Park HS, Park JK et al. (2017) Early Detection and Serial Monitoring of Anthracycline-Induced Cardiotoxicity Using T1-mapping Cardiac Magnetic Resonance Imaging: An Animal Study. Sci Rep 7:2663.
19 Farhad H, Staziaki PV, Addison D et al. (2016) Characterization of the Changes in Cardiac Structure and Function in Mice Treated With Anthracyclines Using Serial Cardiac Magnetic Resonance Imaging. Circulation Cardiovascular imaging 9:e003584.
20 Jordan JH, Vasu S, Morgan TM et al. (2016) Anthracycline-Associated T1 Mapping Characteristics Are Elevated Independent of the Presence of Cardiovascular Comorbidities in Cancer Survivors. Circulation Cardiovascular imaging 9
21 Muehlberg F, Funk S, Zange L et al. (2018) Native myocardial T1 time can predict development of subsequent anthracycline-induced cardiomyopathy. ESC Heart Fail. 10.1002/ehf2.12277.
22 Ferreira VM, Schulz-Menger J, Holmvang G et al. (2018) Cardiovascular Magnetic Resonance in Nonischemic Myocardial Inflammation: Expert Recommendations. J Am Coll Cardiol 72:3158-3176.

Contact

Bernd J. Wintersperger, MD EBCR FAHA
Department of Medical Imaging
Toronto General Hospital, 1 PMB-273
585 University Avenue
Toronto, Ontario, M5G 2N2
Canada
Tel.: 416-340-4800 ex. 8593
Bernd.Wintersperger@uhn.ca


Bernd Wintersperger


Christian Houbois


P. Thavendiranathan

Overview of Magnetic Resonance Fingerprinting

Simone Coppo[1]; Bhairav B. Mehta[1]; Debra McGivney[1]; Dan Ma[1]; Yong Chen[1]; Yun Jiang[2]; Jesse Hamilton[2]; Shivani Pahwa[1]; Chaitra Badve[1]; Nicole Seiberlich[1]; Mark Griswold[1,2]; Vikas Gulani[1]

[1]Department of Radiology, Case Western Reserve University, University Hospitals Case Medical Center, Cleveland, OH, USA
[2]Department of Biomedical Engineering, Case Western Reserve University, University Hospitals Case Medical Center, Cleveland, OH, USA

Introduction

Magnetic Resonance Imaging (MRI) is a powerful diagnostic, prognostic and therapy assessment tool due to its versatile nature as compared to other imaging modalities, as MRI allows the user to probe and measure various kinds of information (T1, T2, B_0, diffusion, perfusion, etc.). However, MRI has the drawback of being slow compared to other diagnostic tools, and is generally qualitative, where the contrast between tissues, rather than absolute measurements from single tissues, is the primary means of information that is used to characterize an underlying pathology. While this information has proven extremely valuable for diagnosis, prognosis, and therapeutic assessment, the lack of quantification limits objective evaluation, leads to a variability in interpretation, and potentially limits the utility of the technology in some clinical scenarios.

To overcome this limitation, significant effort has been put into developing quantitative approaches that can measure tissue proprieties such as T1 and T2 relaxation times. Quantifying tissue proprieties allows physicians to better distinguish between healthy and pathological tissue [1] in an absolute sense, makes it easier to objectively compare different exams in follow-up studies [2], and could be more representative of the underlying changes at the cellular level [3, 4] than standard weighted imaging. Quantitative imaging is crucial in the assessment of disease settings presenting subtle features such as cardiac diffuse fibrosis [5], iron [6] or fat deposition in the liver [7]. Additionally, there are various clinical settings in which multiple features such as T1, T2, diffusion, etc. add up synergistically to drastically improve the information for diagnosis, prognosis and/or therapeutic assessment.

While quantitative imaging has been a long-standing goal of the MR community, a drawback encountered in early conventional quantitative imaging was the reduced time efficiency compared to qualitative imaging. Early conventional approaches for T1 and T2 mapping involved measuring one parameter at a time. These techniques relied on the acquisitions of several images, each with one specific acquisition parameter that varies for each image while the others were kept constant (Fig. 1A). The obtained images were subsequently fitted with a mathematical model to estimate the one parameter of interest, for example the relaxation time (T1) [8] or the time of signal decay (T2) [9] (Fig. 1B). This process had to be repeated for each parameter of interest. The need for keeping all except one sequence parameter and

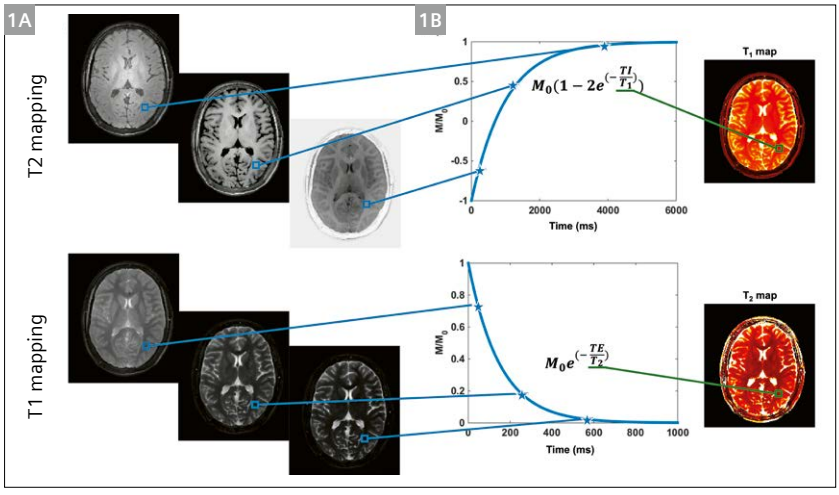

1 Conventional parametric mapping approaches. Example of conventional T1 (above) and T2 (below) mapping techniques. **(1A)** Several fully sampled images are acquired one after the other with different inversion time (for T1) or echo time (for T2). **(1B)** An exponential fitting is performed using the multiple values of each voxel and the relaxation or decay time is the one that provides the best fit.

signal state constant and the limitation of assessing one parameter at a time made these approaches extremely time-inefficient because of the prolonged scan time and thus not suitable for a clinical environment where inter-scan motion can render such approaches infeasible. In recent times, several approaches have been proposed to shorten the acquisition time [10–13] or to provide combined T1 and T2 measurements [14–18] within a single acquisition. However, major barriers remain to clinical adoption, most notably a simultaneous need for rapid and accurate quantification.

To overcome the common drawbacks of quantitative imaging, Magnetic Resonance Fingerprinting (MRF)[1] [19–21] has been recently developed. This technique aims at providing simultaneous measurements of multiple parameters such as T1, T2, relative spin density, B_0 inhomogeneity (off-resonance frequency), etc., using a single, time-efficient acquisition. MRF completely changes the way quantitative MRI is performed with an entirely different approach from that of conventional techniques. Instead of performing an acquisition with all but one sequence parameter constant, MRF relies on deliberately varying acquisition parameters in a pseudorandom fashion such that each tissue generates a unique signal evolution. It is possible to simulate signal evolutions from first principles using different physical models for a wide variety of tissue parameter combinations, which are collected together in a database called dictionary. After the acquisition, a pattern recognition algorithm is used to find the dictionary entry that best represents the acquired signal evolution of each voxel. The parameters that were used to simulate the resulting best match are then assigned to the voxel. This process is analogous to the fingerprinting identification process used by forensic experts to identify persons of interest. The acquired signal evolution is unique for each tissue and can be seen as the collected fingerprint that has to be identified. The dictionary is equivalent to the database where all the known fingerprints are stored, together with all the information relative to each person. In the forensic case, each fingerprint points to the feature identification of the associated person such as name, height, weight, eye color, date of birth, etc. Similarly, in the case of MRF, each fingerprint in the dictionary points to the MR related identification features of the associated tissue such as T1, T2, relative spin density, B_0, diffusion, etc. After the acquisition, the fingerprint contained in a voxel is compared with all the entries in the dictionary. The dictionary entry that best matches the acquired fingerprint is considered a positive match, meaning that the tissue represented in the voxel has been identified. All the known parameters relative to that fingerprint can then be retrieved from the dictionary and assigned to the voxel. The uniqueness of the different signal components and the accuracy with which the dictionary is simulated are two crucial components for the correct estimation of the tissue parameters. This paper attempts to describe the basic concepts of MRF and illustrate some clinical applications.

[1] *The product is still under development and not commercially available yet. Its future availability cannot be ensured. As this is a research topic in predevelopment, all results shown are preliminary in nature and do not allow for generalizations or conclusions to be drawn. Product realization and features therein cannot be assured as the product may undergo futher design iterations.*

Acquisition sequence

Standard quantitative MR imaging approaches require several acquisitions, each one of which constantly repeats the same acquisition pattern, such as radiofrequency excitation angle (flip angle, FA), repetition time (TR) and gradient patterns, until all required data in the Fourier domain (also called *k*-space) are obtained. Each image is then reconstructed using the Fourier transform and a nonlinear fitting process is applied to each voxel. With MRF, instead, the flip angle, the TR and the trajectory (Fig. 2A, B) vary in a pseudorandom fashion throughout the acquisition; when implemented properly, this generates uncorrelated signals for each tissue, providing the unique fingerprints that are used to recognize the tissue. The initial implementation of MRF [19] was based on a balanced steady-state free-precession (bSSFP or TrueFISP) sequence because of its sensitivity to T1, T2 and off-resonance frequency, and because the steady-state signal generated by this sequence has been thoroughly studied [22]. The FA (Fig. 2A) varies in a sinusoidal fashion to smoothly vary the transient state of the magnetization, ranging from 0° to 60° and from 0° to 30° alternatively, with a period of 250 time points, or images. On top of this signal, a random variation is added to induce differences in the time evolutions from tissues with similar parameters. After each half period (250 images), 50 flip angles are set to 0° to allow for signal recovery. The TR variations, instead, are based on Perlin noise [23] which ranges from 9.34 ms to 12 ms. These are only examples of how the parameters can be randomly varied. Other random patterns have been tested [19, 24] showing that MRF is not limited to one specified set of parameters.

An inversion recovery pulse is played out at the beginning of the acquisition sequence to enhance T1 differences between tissues (Fig. 2B). For each TR, a heavily undersampled image is reconstructed (Fig. 2C). It can be noticed how the base image series are not useful by themselves, but each voxel contains a signature fingerprint that will be used later on for the matching (identification). The total number of images acquired (also referred to as 'time points') can vary from acquisition to acquisition, ranging from 1000 [19] to 2500 [21] as function of the image resolution, the undersampling ratio, the matching

approach used, etc. In most cases, we have used a variable-density spiral trajectory [25] designed to have a minimum time gradient and zero moment compensation for the acquisition. For example, we have successfully used a trajectory for a 128 x 128 matrix size that requires one interleaf to fully sample the center of *k*-space and 48 interleaves to fully sample the outer region of *k*-space. In the case of a 256 x 256 matrix, a trajectory requiring 24 interleaves to fully sample the inner region and 48 interleaves to fully sample the outer region can be used instead. Within each TR, one interleaf is acquired and used to reconstruct an image (or time point). The interleaf in the following TR is then rotated by 7.5° (≈ 2π/48) compared to the previous one.

The MRF framework is not only limited to a TrueFISP-based acquisition, but can be virtually applied to any kind of sequence. As an example, the MRF framework has been applied to a steady-state precession sequence (FISP) [20] to avoid the banding artifacts that can appear in wide field-of-view scans or in a high-field-strength scanner. The FISP sequence is still sensitive to T1 and T2 components but is less sensitive to off-resonance frequency. This is caused by the unbalanced gradient within every TR which results in the signal to be the sum of the spins within a voxel, making the sequence immune to banding artifacts. The unbalanced gradient, though, leads the FISP sequence to have a shorter transient state compared to the TrueFISP. For this reason, the pseudorandom FA variation needs to be generated slightly differently than in the case of the TrueFISP sequence, in order to keep incoherence between the signal and under-sampling artifacts and to be able to identify the underlying fingerprint. The FA variation is thus generated based on sinusoidal variation in which the maximum reached FA for each half period randomly

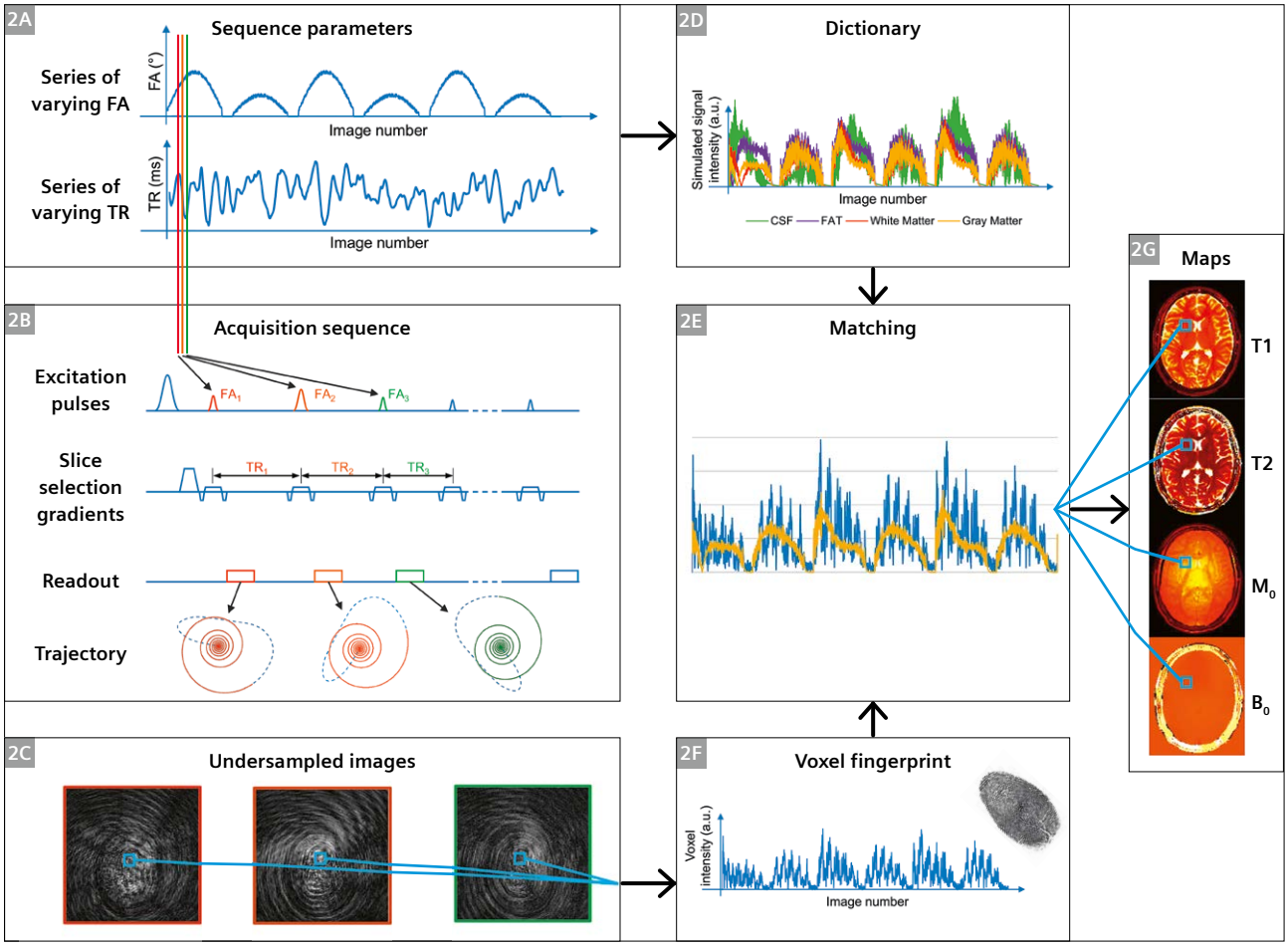

2 Flow chart of the MRF framework. **(2A)** Example of variable FA and TR used for a TrueFISP acquisition. **(2B)** Sequence diagram showing the excitation pulses, slice selection gradients, readout and *k*-space trajectory for each TR; **(2C)** Example of three undersampled images acquired in three different TR. **(2D)** Examples of four dictionary entries representing four main tissues: cerebrospinal fluid (CSF) (T1 = 5000 ms, T2 = 500 ms), fat (T1 = 400 ms, T2 = 53 ms), white matter (T1 = 850 ms, T2 = 50 ms), gray matter (T1 = 1300 ms, T2 = 85 ms); **(2E)** Matching of a voxel fingerprint with the closest entry in the dictionary, which allows to retrieve the tissue features represented by that voxel; **(2F)** intensity variation of a voxel across the undersampled images (fingerprint); **(2G)** parameter maps obtained repeating the matching process for each voxel.

changes, ranging from 5° to 90°. The TR variation is always based on a Perlin noise pattern which ranges from 11.5 ms to 14 ms.

Dictionary generation

The dictionary can be seen as the heart of the MRF framework; it is the database that contains all physiologically possible signal evolutions that may be observed from the acquisition and that makes it possible to recognize the tissue within each voxel. MRF, like the forensic fingerprinting identification process, is effective only when a database large enough to contain all the potential candidates is available. In MRF, the dictionary is generated on a computer using algorithms that simulate the spin behavior during the acquisition and thus predict the realistic signal evolution. In case of a TrueFISP-based acquisition, the Bloch equations [26] are used to simulate the various effects of the acquisition sequence on the spins, given a set of tissue parameters of interest (Fig. 2D). The information that can be retrieved with MRF is thus related to how and what physical effects are simulated. In the initial stages of development, MRF includes the simulation of T1, T2 and off-resonance, but more tissue features can be simulated and extracted, such as partial volume [19], diffusion [27] and perfusion [28].

A critical aspect of the dictionary is its size: to ensure the identification of any possible tissue parameter present in the acquisition, a wide combination of T1, T2 and off-resonance frequency need to be simulated. A standard TrueFISP dictionary with the parameter ranges as shown in Table 1 leads to a total of 363,624 possible combinations and includes the parameter values that are commonly found in the human body. The computation of such a dictionary for 1000 time points takes about 2.5 minutes on a standard desktop computer using a C++ based script and reaches 2.5 GB of memory size. A further increase in the dictionary size and/or resolution would increase the accuracy of the obtained maps at the expenses of an increase in the reconstruction time and memory requirements [19].

The simulation of a FISP acquisition is computed differently compared to the one described above. Since the FISP acquisition requires the simulation of multiple isochromats at different frequencies, which are then combined together, the simulation process through Bloch equations can be time consuming. An alternative time-efficient simulation is the extended phase graph (EPG) formalism [29], where a spin system affected by the sequence can be represented as discrete set of phase states, ideal to simulate the signal evolution of spins strongly dephased by unbalanced gradients. The FISP sequence is less sensitive to off-resonance effects compared to the TrueFISP acquisition, so the corresponding dictionary includes only the T1 and T2 relaxation times (Table 1) as the parameters of interest. This leads to 18,838 dictionary entries that can be computed in about 8 minutes on a standard desktop computer, and that generates a dictionary of about 1.2 GB. Regardless of which sequence is used, the dictionary needs to be computed only once beforehand. It can then be used on the scanner, where it is used to reconstruct each MRF acquisition acquired with the sequence parameters that were simulated.

Matching

After the data acquisition, the fingerprint of each voxel (Fig. 2F) is normalized to unit norm and compared with all the normalized dictionary entries to identify the tissue in a given voxel (Fig. 2E). The simplest version of the matching is performed by taking the inner product between the voxel signal and each simulated fingerprint signal; the entry that returns the highest value is considered to be the one that best represents the tissue properties, and the respective T1, T2 and off-resonance values are assigned to the voxel (Fig. 2G). The relative spin density

	TrueFISP			FISP		
Parameter	Min value	Max value	Step size	Min value	Max value	Step size
T1 (ms)	100	2000	20	20	3000	10
	2000	5000	300	3000	5000	200
T2 (ms)	20	100	5	10	300	5
	100	200	10	300	500	50
	200	1900	200	500	900	200
Off-resonance (Hz)	-250	-190	20			
	-250	50	1			
	190	250	20			

Table 1: Ranges and step sizes used for the dictionary creation in case of a TrueFISP sequence (left) or FISP sequence (right).

(M_0) map, instead, is computed as the scaling factor between the acquired and the simulated fingerprints. The inner product has been demonstrated to be a robust operation and is able to correctly classify the tissues even in case of low SNR due to undersampling or even in the presence of a limited amount of motion artifacts [19].

This approach has also the potential of distinguishing different tissue components present within a single voxel (partial volume effect) thanks to the incoherence between different signal evolutions. The fingerprint (S) of a voxel containing different tissue can be seen as the weighted sum (w) of the different components (D): S = Dw. It has been shown [19] that, if the different components are known a priori, the appropriate inverse solution of the previous equation – $(D)^{-1}S = w$, where $(D)^{-1}$ represents the pseudoinverse of D – will provide the weight of each different tissue for each voxel [19,31].

The pattern recognition algorithm is performed on the scanner for every acquisition, so it is crucial for the clinical usefulness of the MR framework that this operation is performed in a reasonable time. While the direct matching using the inner product is accurate, it can take up to about 160 seconds to match a 2D slice of 128 x 128 base resolution, 1000 time points with a dictionary counting 363 624 entries. Similarly it takes about 30 seconds to match a 2D image with 256 x 256 voxels, 1000 time points and 18,838 dictionary entries for a FISP reconstruction.

The matching can be potentially accelerated by compressing the dictionary either in the time dimension or in the parameter combinations dimension, thus reducing the total number of comparisons that need to be performed. It has been shown [31] that the singular value decomposition (SVD) can be applied to compress the dictionary in the time dimension and reduce the matching time by a factor of 3.4 times for a TrueFISP dictionary and up to a factor of 4.8 times for a FISP dictionary. The SVD-based dictionary compression has less than 2% of reduction in the accuracy of the estimated parameters. In this approach, the dictionary is projected into a subspace of lower dimension spanned by the first 25–200 singular vectors obtained from the SVD. The acquired fingerprint is projected onto the same subspace, and the matching is performed using the projected signal and the compressed dictionary. This framework reduces the number of calculations, thus reducing the final computation time despite the added operation of data projection on the subspace.

An alternative approach for reducing computational time for matching is by reducing the parameter combination dimension. A fast group matching algorithm [32] has been developed, where dictionary entries that have strong correlations are grouped together and a new signal that best represents the group is generated. The matching is thus subdivided in two steps; at first the acquired fingerprint is matched with the representing signal of each group, and only groups that return the highest correlation are kept in consideration. Then matching is used to find the best fit between the fingerprint and the remaining dictionary entries for the assignment of the parameters. This algorithm reduces the matching computation speed of one order of magnitude compared to the SVD compression and two orders of magnitude compared to the direct matching with no significant loss in the quality of the match. Techniques such as this make it feasible to implement MRF in a clinical manner.

Undersampling and motion

In MRF, the obtained parameter maps are the result of a pattern recognition algorithm as opposed to conventional reconstruction techniques, which allows MRF to be more robust to various image artifacts. This effect is strengthened by the random variation of FA, TR and trajectory which not only aim at differentiating the fingerprints from different tissues, but also aim at increasing the incoherence between the fingerprints. The matching can recognize the underlying signal evolutions even in low signal-to-noise or accelerated conditions as long as the noise or undersampling artifacts are incoherent with the signal. Additionally, just like in forensic fingerprinting, a correct identification is possible even with the use of blurry or partial fingerprints, the MR counterpart is also capable of providing parametric maps without any residual motion artifacts in case of a fingerprint partially corrupted by motion [19].

Volunteer acquisitions

MRF acquisitions have been tested in volunteers in 2D brain, abdominal, and cardiac scans. All *in vivo* experiments were performed under the Institutional Review Board guidelines and each subject signed informed consent prior to the data acquisition. The scans were performed on a 3T MAGNETOM Skyra system with a 20-channel head coil or a phased array 18-channel body coil plus spine coil. For the brain scans, the variable acquisition parameters (FA and TR) were set as described above and 3000 time points were acquired; the FOV was 300 x 300 mm, the slice thickness was 5 mm and the matrix size was 256 x 256. The acquisition time was 38 s for a 2D TrueFISP slice and 41 s for the FISP acquisition. The cardiac MRF scans were acquired using a modified pulse sequence with ECG triggering to restrict data collection to

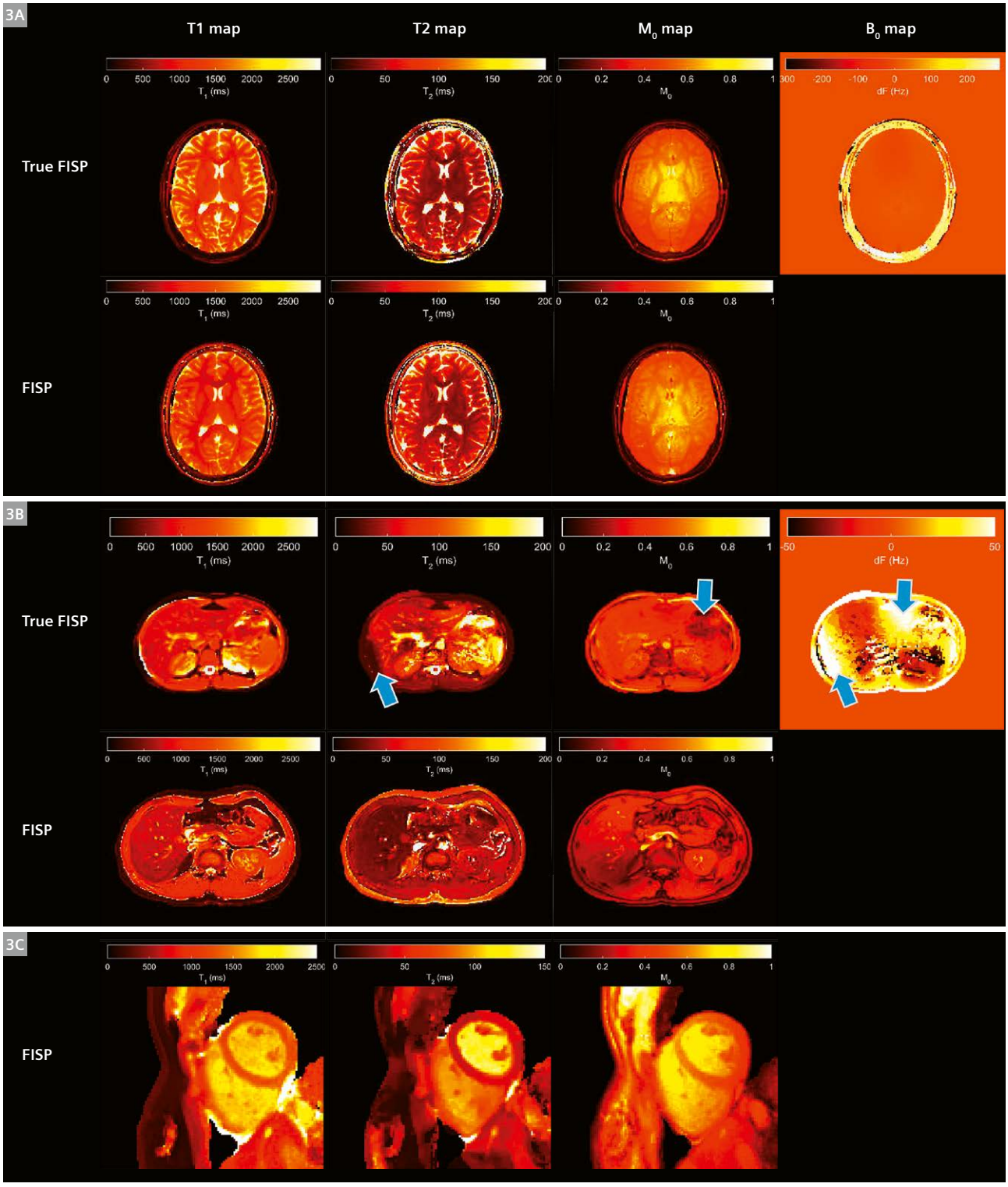

3 Examples of T1, T2, relative spin density (M_0) and off-resonance (B_0) maps acquired in two volunteers with a TrueFISP and a FISP acquisition. **(3A)** Single 2D slice of a head scan. **(3B)** Single 2D slice of an abdominal scan. **(3C)** Single 2D slice of diastolic cardiac scan in short axis view. In the T2 and B_0 map obtained from the TrueFISP acquisition, banding artifacts due to field inhomogeneity are visible (blue arrows).

	T1 (ms)		T2 (ms)	
Tissue	MRF	Literature	MRF	Literature
White matter	685 ± 33 [19]	608–756 [34, 40–42]	65 ± 4 [19]	54–81 [34, 40–42]
	781 ± 61 [20]	788–898 [43]	65 ± 6 [20]	78–80 [43]
Gray matter	1180 ± 104 [19]	998–1304 [34, 40–42]	97 ± 5.9 [19]	78–98 [34, 40–42]
	1193 ± 65 [20]	1286–1393 [43]	109 ± 11 [20]	99–117 [43]
Cerebrospinal fluid	4880 ± 379 [19]	4103–5400 [34, 40–42]	550 ± 251 [19]	1800–2460 [34, 40–42]
Liver	745 ± 65 [21]	809 ± 71 [44]	31 ± 6 [21]	34 ± 4 [44]
Kidney medulla	1702 ± 205 [21]	1545 ± 142 [44]	60 ± 21 [21]	81 ± 8 [44]
Kidney cortex	1314 ± 77 [21]	1142 ± 154 [44]	47 ± 10 [21]	76 ± 7 [44]
Skeletal muscle	1100 ± 59 [21]	1017 ± 78 [45]	44 ± 9 [21]	50 ± 4 [46]
Fat	253 ± 42 [21]	343 ± 37 [45]	77 ± 16 [21]	68 ± 4 [44]

Table 2: List of T1 and T2 relaxation times measured with MRF for different tissues and comparison with the value available in literature.

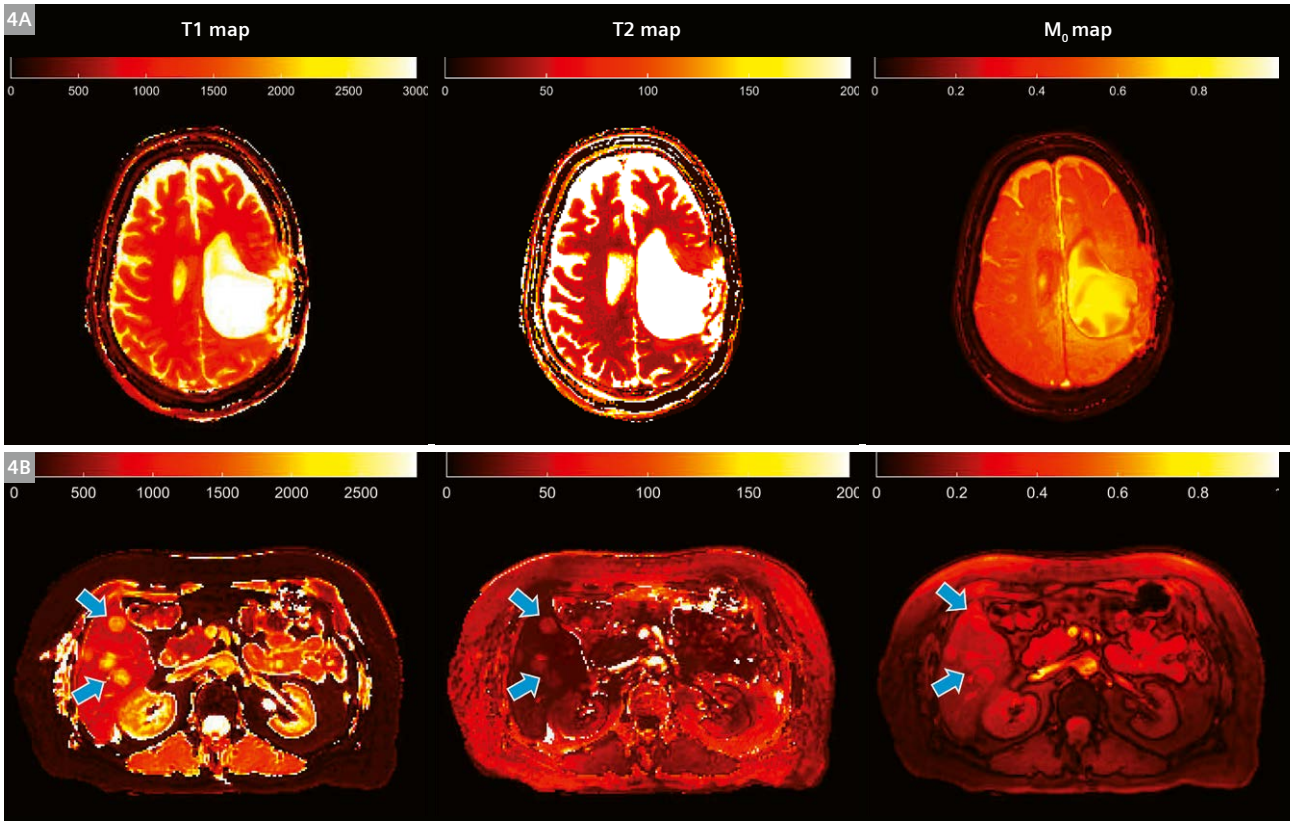

4 Example of patient results. Quantitative T1, T2 and relative spin density (M_0) maps obtained using the FISP protocol for brain [16] and abdomen acquisitions [20]. **(4A)** Maps of a patient with a brain tumor; **(4B)** 69-year-old patient with metastatic breast cancer. The metastasis (blue arrows) presents an increase in all tissue parameters, compared to the surrounding tissues.

mid-diastole [35]. A total of 768 time points were acquired over a 16-heartbeats breath-hold using a scan window of 250 ms with FOV 300 x 300 mm, slice thickness 8 mm, and matrix size 192 x 192 [35]. For the abdominal and cardiac imaging, the trajectory and acquisition protocols were adapted as described in references [21, 35] respectively. The dictionaries were computed as described above and SVD based matching was used for parameter estimation.

Figure 3 shows the maps obtained from volunteer scans in the brain (Fig. 3A), abdomen (Fig. 3B), and heart (Fig. 3C). Both FISP and TrueFISP MRF provide comparable high resolution multiparametric tissue maps. The FISP acquisition has the drawback of not providing the off-resonance information, but it has the advantage of being insensitive to banding artifacts. Therefore, FISP MRF is advantageous for body imaging, where the sharp susceptibility transitions and the need for a large field-of-view would lead to banding artifacts with a balanced SSFP acquisition.

The values obtained with MRF maps are generally in good agreement with the standard mapping techniques [20] and with the literature value of tissue parameters [19, 24], as shown in table 2. It can be noticed, though, that there is a mismatch in the values of CSF and fat. The CSF T2 discrepancy between MRF and literature value can be explained by through-plane motion of the fluid that was not taken into account in the dictionary simulation [19]. The fat T1 discrepancy, instead, is mainly due to the intentionally low T1 dictionary resolution (100 ms) for the range 100–600 ms used for that study [21].

The MRF efficiency is extremely high compared to traditional mapping approaches [19–21] as well as rapid combined T1 and T2 mapping methods like DESPOT [19, 36]. The high efficiency and accuracy of the MRF framework enable parametric mapping to be performed in a clinically relevant acquisition time without loss of information. In this way, multiparametric mapping can be translated to the clinical environment.

Patient acquisitions

The MRF framework has also been successfully tested on patients. Figure 4 shows the feasibility of brain and abdominal MRF in a clinical environment. Data were acquired with the previously described FISP acquisitions on patients with a brain tumor and breast cancer metastatic to the liver (Fig. 4). Longer T1 relaxation time can be observed in the metastatic lesions compared to the surrounding tissues. It has been shown in six patients with metastatic adenocarcinoma that the mean T1 and T2 values in the metastatic adenocarcinoma were on the order of 1673 ± 331 ms and 43 ± 13 ms, respectively. Those values are significantly higher than the ones of the surrounding tissues (840 ± 113 ms and 28 ± 3 ms, respectively) [21].

Recent studies investigate the possibility of predicting response of tumor to treatment using tissue relaxation times; e.g. the T1 relaxation time can potentially be an indicator of chemotherapy response [35, 36]. Fast multiparametric mapping can thus open the path to the creation of a multi-property space that might allow a deeper characterization and understanding of the conditions and evolutions of determined pathologies.

Synthetic weighted images

It is also possible to retrospectively calculate and estimate 'standard' weighted images from the multiple parameter maps obtained from an MRF scan. Figure 5 shows an example of T1-weighted and T2-weighted acquisition calculated from the FISP T1 and T2 maps of the volunteer and patient head scan shown above.

Conclusions

Magnetic resonance fingerprinting is a novel framework for MRI, where the pulse sequence design is not aimed at acquiring images, but at directly measuring tissue properties. In MRF, the sequence generates unique signal evolutions, or fingerprints, for each different tissue and matches it with a set of theoretical signal evolutions to measure several tissue properties within a single acquisition. Once the tissue features are measured, it is possible to directly

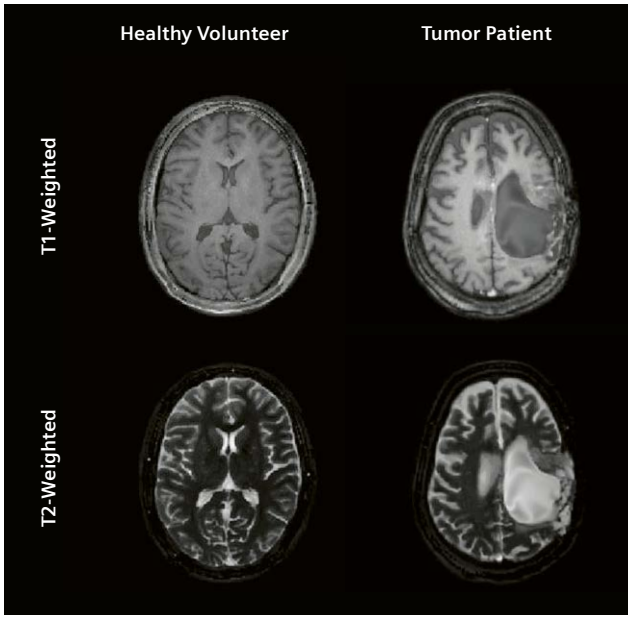

5 Synthetic generation of conventional images. Example of T1-weighted and T2-weighed images from a healthy volunteer and a patient with brain tumor, reconstructed starting from the T1, T2 and M_0 maps obtained from the FISP MRF maps of Figure 3 and 4.

know several tissue-specific properties that can synergistically provide all the information to improve diagnosis, prognosis and/or therapeutic assessment. In this work, only two MRF implementations have been shown, but the MRF framework has the potential to allow more freedom in the sequence design compared to standard MRI sequences, since the parameters can be randomly varied. Thanks to this freedom, a whole new world of possibilities of acquisition and reconstruction strategies that can probe and measure new features have been opened up for our community to explore.

This paper focused on T1, T2, M_0 and B_0 characterization, but the MRF is not limited to that. Several work are being performed to exploit the potential of MRF including: diffusion [27], arterial spin labeling [28, 42, 43] and chemical exchange [44].

The pattern recognition nature of MRF makes the acquisition robust to artifacts like undersampling and motion, yielding high efficiency, accuracy and robustness that are critical for the successful integration of a multiparametric mapping technique into the clinical environment. Moreover, the increased efficiency and robustness to artifacts compared to standard MR imaging approaches could potentially reduce the time and thus the costs of MRI exams, making it more affordable and more competitive in comparison to other imaging modalities.

References

1 Larsson H, Frederiksen J. Assessment of demyelination, edema, and gliosis by in vivo determination of T1 and T2 in the brain of patients with acute attack of multiple sclerosis. Magn Reson Med [Internet]. 1989;348:337–48. Available from: http://onlinelibrary.wiley.com/doi/10.1002/mrm.1910110308/abstract

2 Usman AA, Taimen K, Wasielewski M, et al. Cardiac magnetic resonance T2 mapping in the monitoring and follow-up of acute cardiac transplant rejection: a pilot study. Circ Cardiovasc Imaging [Internet]. 2012;5(6):782–90. Available from: http://www.ncbi.nlm.nih.gov/pubmed/23071145

3 Payne AR, Berry C, Kellman P, et al. Bright-blood T 2-weighted MRI has high diagnostic accuracy for myocardial hemorrhage in myocardial infarction a preclinical validation study in swine. Circ Cardiovasc Imaging. 2011;4(6):738–45.

4 Van Heeswijk RB, Feliciano H, Bongard C, et al. Free-breathing 3 T magnetic resonance T2-mapping of the heart. JACC Cardiovasc Imaging [Internet]. 2012 Dec;5(12):1231–9. Available from: http://www.ncbi.nlm.nih.gov/pubmed/23236973

5 Iles L, Pfluger H, Phrommintikul A, et al. Evaluation of Diffuse Myocardial Fibrosis in Heart Failure With Cardiac Magnetic Resonance Contrast-Enhanced T1 Mapping. J Am Coll Cardiol. 2008;52(19):1574–80.

6 Hernando D, Levin YS, Sirlin CB, Reeder SB. Quantification of liver iron with MRI: state of the art and remaining challenges. J Magn Reson Imaging [Internet]. 2014 Nov;40(5):1003–21. Available from: http://www.pubmedcentral.nih.gov/articlerender.fcgi?artid=4308740&tool=pmcentrez&rendertype=abstract

7 Reeder SB, Cruite I, Hamilton G, Sirlin CB. Quantitative assessment of liver fat with magnetic resonance imaging and spectroscopy. J Magn Reson Imaging [Internet]. 2011 Oct;34(4):729–49. Available from: http://www.ncbi.nlm.nih.gov/pubmed/21928307

8 Look DC, Locker DR. Time saving in measurement of NMR and EPR relaxation times. Rev Sci Instrum. 1970;41(2):250–1.

9 Huang TY, Liu YJ, Stemmer A, Poncelet BP. T2 measurement of the human myocardium using a T 2-prepared transient-state trueFISP sequence. Magn Reson Med. 2007;57:960–6.

10 Mehta BB, Chen X, Bilchick KC, Salerno M, Epstein FH. Accelerated and navigator-gated look-locker imaging for cardiac T1 estimation (ANGIE): Development and application to T1 mapping of the right ventricle. Magn Reson Med. 2015;73(1):150–60.

11 Zhu DC, Penn RD. Full-brain T1 mapping through inversion recovery fast spin echo imaging with time-efficient slice ordering. Magn Reson Med. 2005;54(3):725–31.

12 Cheng H-LM, Wright GA. Rapid High-Resolution T1 Mapping by Variable Flip Angles: Accurate and Precise Measurements in the Presence of Radiofrequency Field Inhomogeneity. Magn Reson Med. 2006;55:566–76.

13 Doneva M, Börnert P, Eggers H, Stehning C, Sénégas J, Mertins A. Compressed sensing reconstruction for magnetic resonance parameter mapping. Magn Reson Med. 2010;64(4):1114–20.

14 Deoni SCL, Rutt BK, Peters TM. Rapid combined T1 and T2 mapping using gradient recalled acquisition in the steady state. Magn Reson Med. 2003;49(3):515–26.

15 Blume U, Lockie T, Stehning C, et al. Interleaved T1 and T2 relaxation time mapping for cardiac applications. J Magn Reson Imaging. 2009;29:480–7.

16 Warntjes JBM, Dahlqvist O, Lundberg P. Novel method for rapid, simultaneous T1, T2*, and proton density quantification. Magn Reson Med. 2007;57(3):528–37.

17 Schmitt P, Griswold MA, Jakob PM, et al. Inversion recovery TrueFISP: quantification of T(1), T(2), and spin density. Magn Reson Med. 2004;51(4):661–7.

18 Ehses P, Seiberlich N, Ma D, et al. IR TrueFISP with a golden-ratio-based radial readout: Fast quantification of T1, T2, and proton density. Magn Reson Med. 2013;69(1):71–81.

19 Ma D, Gulani V, Liu K, et al. Magnetic resonance fingerprinting. Nature [Internet]. 2013;495(7440):187–92.

20 Jiang Y, Ma D, Seiberlich N, Gulani V, Griswold M a. MR fingerprinting using fast imaging with steady state precession (FISP) with spiral readout. Magn Reson Med [Internet]. 2014;. Available from: http://www.ncbi.nlm.nih.gov/pubmed/25491018

21 Chen Y, Jiang Y, Pahva Shivani, et al. MR Fingerprinting for Rapid Quantitative Abdominal Imaging. Radiology. 2016;000(0):1–9.

22 Schmitt P, Griswold MA, Gulani V, Haase A, Flentje M, Jakob PM. A simple geometrical description of the TrueFISP ideal transient and steady-state signal. Magn Reson Med. 2006;55(1):177–86.

23 Perlin K. An image synthesizer. ACM SIGGRAPH Comput Graph. 1985;19(3):287–96.

24 Ma D, Pierre EY, Jiang Y, et al. Music-based magnetic resonance fingerprinting to improve patient comfort during MRI examinations. Magn Reson Med [Internet]. 2015; Available from: http://doi.wiley.com/10.1002/mrm.25818

25 Lee JH, Hargreaves B a., Hu BS, Nishimura DG. Fast 3D Imaging Using Variable-Density Spiral Trajectories with Applications to Limb Perfusion. Magn Reson Med. 2003;50(6):1276–85.

26 Bloch F. Nuclear induction. Phys Rev. 1946;70:460–85.

27 Jiang Y, Wright KL, Seiberlich N, Gulani V, Griswold MA. Simultaneous T1, T2, diffusion and proton density quantification with MR fingerprinting. In: In proceedings of the 22nd annual meeting of ISMRM meeting & exhibition in Milan, Italy. 2014. p. 28.

28 Wright KL, Ma D, Jiang Y, Gulani V, Griswold MA, Luis H-G. Theoretical framework for MR fingerprinting with ASL: simultaneous quantification of CBF, transit time, and T1. In: In proceedings of the 22nd annual meeting of ISMRM meeting & exhibition in Milan, Italy. 2014. p. 417.
29 Weigel M, Schwenk S, Kiselev VG, Scheffler K, Hennig J. Extended phase graphs with anisotropic diffusion. J Magn Reson. 2010;205(2):276–85.
30 Deshmane AV, Ma D, Jiang Y, et al. Validation of Tissue Characterization in Mixed Voxels Using MR Fingerprinting. In: In proceedings of the 22nd annual meeting of ISMRM meeting & exhibition in Milan, Italy. 2014. p. 0094.
31 McGivney D, Pierre E, Ma D, et al. SVD Compression for Magnetic Resonance Fingerprinting in the Time Domain. IEEE Trans Med Imaging. 2014;0062(12):1–13.
32 Cauley SF, Setsompop K, Ma D, et al. Fast group matching for MR fingerprinting reconstruction. Magn Reson Med [Internet]. 2014;00. Available from: http://dx.doi.org/10.1002/mrm.25439
33 Hamilton JI, Jiang Y, Chen Y, et al. MRF for Rapid Quantification of Myocardial T1, T2, and Proton Spin Density. Magn Reson Med. 2016;In press.

Contact

Vikas Gulani, M.D.
Department of Radiology
Case Western Reserve University
University Hospitals Case Medical Center
11100 Euclid Ave
Bolwell Building, Room B120
Cleveland, OH 44106
USA
vxg46@case.edu

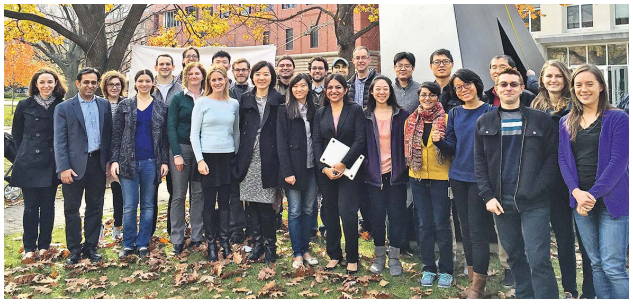

34 Deoni SCL, Peters TM, Rutt BK. High-resolution T1 and T2 mapping of the brain in a clinically acceptable time with DESPOT1 and DESPOT2. Magn Reson Med. 2005;53(1):237–41.
35 Jamin Y, Tucker ER, Poon ES, et al. Evaluation of Clinically Translatable MR Imaging Biomarkers of Therapeutic Response in the TH- MYCN Transgenic Mouse Model of Neuroblastoma. Radiology. 2012.
36 Weidensteiner C, Allegrini PR, Sticker-Jantscheff M, Romanet V, Ferretti S, McSheehy PM. Tumour T1 changes in vivo are highly predictive of response to chemo-therapy and reflect the number of viable tumour cells - a preclinical MR study in mice. BMC Cancer. 2014;14(1):88.
37 Christen T, Pannetier NA, Ni WW, et al. MR vascular fingerprinting: A new approach to compute cerebral blood volume, mean vessel radius, and oxygenation maps in the human brain. Neuroimage [Internet]. 2014 Apr 1 [cited 2015 Nov 19];89:262–70. Available from: http://www.pubmedcentral.nih.gov/articlerender.fcgi?artid=3940168&tool=pmcentrez&rendertype=abstract
38 Pan S, Mao D, Peiying L, Yang L, Babu W, Hanzhang L. Arterial Spin Labeling without control/label pairing and post-labeling delay: an MR fingerprinting implementation. In: In proceedings of the 23rd annual meeting of ISMRM meeting & exhibition in Toronto, Canada. 2015. p. 0276.
39 Hamilton JI, Deshmane AV, Stephanie H, Griswold MA, Seiberlich N. Magnetic Resonance Fingerprinting with Chemical Exchange (MRF-X) for Quantification of Subvoxel T1, T2, Volume Fraction, and Exchange Rate. In: In proceedings of the 23rd annual meeting of ISMRM meeting & exhibition in Toronto, Canada. 2015. p. 0329.
40 Vymazal J, Righini A, Brooks RA, et al. T1 and T2 in the Brain of Healthy Subjects, Patients with Parkinson Disease, and Patients with Multiple System Atrophy: Relation to Iron Content. Radiology. 1999;211(2):489–95.
41 Whittall KP, MacKay AL, Graeb DA, Nugent RA, Li DK, Paty DW. In vivo measurement of T2 distributions and water contents in normal human brain. Magn Reson Med. 1997;37(1):34–43.
42 Poon CS, Henkelman RM. Practical T2 quantitation for clinical applications. J Magn Reson Imaging. 1992;2(5):541–53.
43 Wansapura JP, Holland SK, Dunn RS, Ball WS. NMR relaxation times in the human brain at 3.0 tesla. J Magn Reson Imaging. 1999;9(4):531–8.
44 de Bazelaire CM, Duhamel GD, Rofsky NM, Alsop DC. MR imaging relaxation times of abdominal and pelvic tissues measured in vivo at 3.0 T: preliminary results. Radiology. 2004;230(3):652–9.
45 Chen Y, Lee GR, Aandal G, et al. Rapid volumetric t1 mapping of the abdomen using three-dimensional through-time spiral GRAPPA. Magnetic Resonance in Medicine. 2016 Apr;75(4):1457-65.
46 Stanisz GJ, Odrobina EE, Pun J, et al. T1, T2 relaxation and magnetization transfer in tissue at 3T. Magn Reson Med [Internet]. 2005/08/09 ed. 2005;54(3):507–12. Available from: http://www.ncbi.nlm.nih.gov/pubmed/16086319.

syngo Virtual Cockpit – Your Software for Remote Scanning Assistance and More Flexible Workforce Management

Petra Kraft; Janis Dummet

Siemens Healthineers, Forchheim, Germany

Growing financial pressure and increasingly assertive patients are pushing imaging providers toward finding ways to deliver high-quality care while at the same time keeping costs low. As a relevant cost and quality factor, healthcare personnel have a considerable bearing on tackling these challenges. But as qualified staff is expensive and hard to come by in some markets, optimal deployment of human resources is key to success. New working methods are required that will enable hospitals to deal with the increasing workload and quality expectations despite having a smaller workforce at their disposal.

syngo Virtual Cockpit[1], our new software solution, allows medical staff to connect remotely to scanner workplaces to assist personnel at a different location, especially where more sophisticated examinations are required. *syngo* Virtual Cockpit can be used with CT, MR, and MR PET scanners from Siemens Healthineers. The ability to deploy experienced technologists across multiple locations allows healthcare providers to manage their workforce more flexibly and thus ease tight human resources.

Connecting clinical teams beyond physical boundaries

For radiological examinations, experienced colleagues can "tune in" quickly and in real time via headsets, conference speakers, chat or video functions. That means that the steering technologists[2] can remain at their own location and provide guidance to the modality technologist[3] operating the scanner at another location, e.g., to adjust protocol parameters.

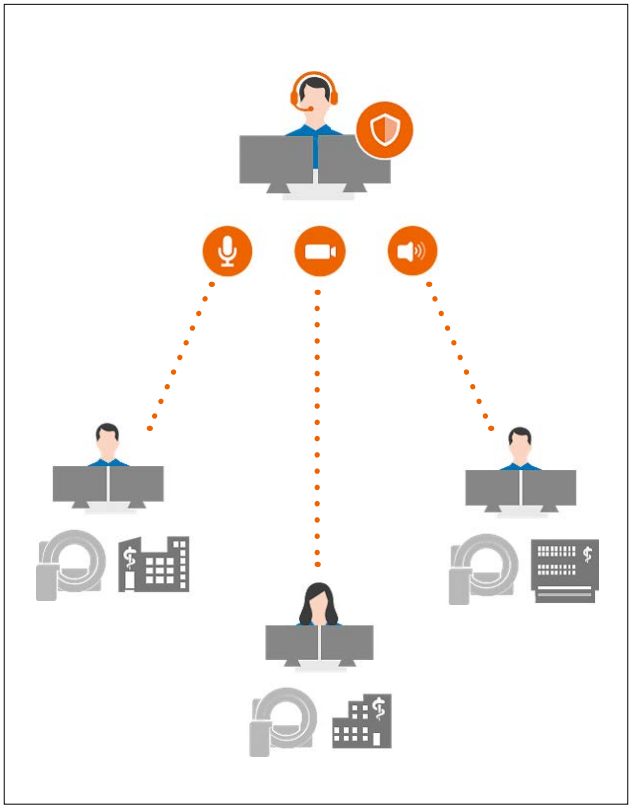

1 *syngo* Virtual Cockpit allows medical staff to provide comprehensive scanning assistance to imaging personnel via video, audio, and chat functions. Up to three scanners at different locations can be supported simultaneously by one steering technologist.

[1]*syngo Virtual Cockpit is not commercially available in all countries. For regulatory reasons, its future availability cannot be guaranteed. Precondition: Expert-i enabled modality from Siemens Healthineers.*
[2]*Steering technologist: An experienced technologist who works with syngo Virtual Cockpit and connects to modalities remotely.*
[3]*Modality technologist: A technologist who works locally at the modality site.*
[4]*The statements by Siemens Healthineers' customers presented here are based on results that were achieved in the customer's unique setting. Since there is no 'typical' hospital and many variables exist (e.g., hospital size, case mix, level of IT adoption), there can be no guarantee that other customers will achieve the same results.*

"We expect the use of syngo Virtual Cockpit to have a significant impact because we will save costs by not sending dedicated steering technologists from one site to the other. We will also be able to better utilize our scanner fleet. Our patients will also benefit, because they no longer have to go to a dedicated site in our network to get a special examination."[4]

Associate Professor Justus Roos, M.D., Head of Radiology and Nuclear Medicine
Lucerne Cantonal Hospital (LUKS), Switzerland

Improving workforce productivity

With this software tool, the steering technologist can perform scans at one location while offering remote support to up to three colleagues in parallel. This makes the best possible use of resources and can lead to an increase in the total number of scans performed. Having the support of a steering technologist on hand can also positively affect the efficiency of scan procedures. Experience from Alliar Médicos à Frente, a large radiology network in Brazil, showed that with *syngo* Virtual Cockpit, the scan time could be reduced by 33%. Furthermore, long commutes between different sites are no longer necessary as steering technologists can guide exams performed by on-site technologists with *syngo* Virtual Cockpit from anywhere, which in turn saves time and costs. Also, in this way it is easy to overcome bottlenecks due to vacation periods, sick leave, nightshifts or other reasons.

Achieving a higher level of standardization

Especially when it comes to complex examinations, expert knowledge is critical. With *syngo* Virtual Cockpit, less-experienced staff can always call on a colleague for live support. This remote collaboration helps reduce the number of unwarranted variations in reports, resulting in consistent image quality across the healthcare enterprise and more accurate diagnoses. With the introduction of *syngo* Virtual Cockpit Alliar Médicos à Frente in Brazil was able to reduce the number of rescans to less than 1% of cases.

Increasing patient satisfaction

Patient satisfaction is becoming an increasingly relevant factor in the reimbursement of healthcare services. *syngo* Virtual Cockpit can have a positive impact on the productivity of medical institutions. Furthermore, making

MR workplace

Chat window on additional PC (e.g., RIS client)

2 The modality technologist is sitting at the modality console. To start a supported session, the chat tool of *syngo* Virtual Cockpit can be opened on another Windows PC, for example, the PC used for the RIS.

expert knowledge available independent of location means that specialized examinations can be offered at any site in a healthcare network. As a result, patients receive appointments more quickly for examinations at their preferred location. In this way, *syngo* Virtual Cockpit improves patient convenience and provides access to healthcare to more patients, in particular those requiring complex examinations.

The *syngo* Virtual Cockpit workflow – easy and intuitive

Imagine a complex examination is planned at an MR scanner. Due to a lack of onsite knowledge, a decision is made to support the examination remotely.

Step 1: Establishing a connection between modality and steering technologist
The modality technologist is sitting at the MR workplace and logs onto the *syngo* Virtual Cockpit software at a Windows PC next to the modality console. In a chat window, the modality technologist can see a list of all available steering technologists. The modality technologist can now choose one of those colleagues and start a chat. Later the steering technologist can connect and assist remotely at the MR console.

Step 2: Logging on securely to the scanner workplace
To establish a connection via *syngo* Virtual Cockpit, the steering technologist needs to enter a one-time password provided by the modality technologist.

The modality technologist clicks the Expert-i icon on the modality workplace and a one-time password is displayed. The modality technologist types this password in the chat window of *syngo* Virtual Cockpit.

The steering technologist now has full access to the modality workplace. Two IP cameras can be set up at the modality to show e.g. the patient on the table and the monitor of the contrast injector.

Step 3: Performing the scan with remote assistance
The modality technologist positions the patient on the exam table. As soon as all workflow steps such as coil positioning have been completed, the modality technologist leaves the room.

Now the steering technologist assists in the scanning procedure. Both colleagues keep in constant contact by communicating via speakerphone, headset, or chat. If contrast media has to be injected, it is the task of the modality technologist to start injection on site. If a CT examination is being performed, it is also the modality technologist's task to start the radiation or move the table.

syngo Virtual Cockpit is compatible with most Siemens Healthineers scanners

syngo Virtual Cockpit software can be used with all MR systems equipped with software version MR VA or later that support Expert-i. For CT, *syngo* Virtual Cockpit is compatible with all Somaris 7-based scanners with software version VB20[5], all Somaris 5-based scanners with software version VC50, as well as all Somaris X-based scanners (.go platform) with software version VA30[5]. For details, please contact your local Siemens Healthineers organization.

3 Each modality is displayed in a dedicated segment of the screen on the steering technologist's workplace with its own chat window. The steering technologist can see all the necessary information on his or her workplace: Contact list, chat, modality camera and contrast monitor overview. Moreover, the user name of each technologist is always visible.

"If you really have a shortage of technicians and you have to decide every morning whether you have to close a machine, yes or no, that's not really convenient. I mean we totally reduced that down to zero."[4]

Professor Michael Forsting, M.D., Director, Institute of Diagnostic and Interventional Radiology and Neurology, University Hospital Essen, Germany

Technical requirements for *syngo* Virtual Cockpit

syngo Virtual Cockpit requires the following hardware and software equipment:

- The steering technologist workplace requires one PC (Windows 10), two monitors, and a communication device.
- The modality technologist workplace needs to be equipped with one PC (Windows 7/8/10) with one monitor, one to two IP cameras, and a communication device (with headset or speakerphone).
- For a stable connection, a minimum bandwidth of 60 Mbps[6] is needed between the steering client and the modality.[7]

Summary

Our new software solution *syngo* Virtual Cockpit has been designed to assist scan procedures remotely from any location. By making expert knowledge available across sites in real time, *syngo* Virtual cockpit addresses the challenge of the shortage of experienced technologists while at the same time ensuring high-quality care.

[5] *Both software versions VB20 and VA30 are under development. Not available for sale. Future availability cannot be guaranteed.*
[6] *For connecting one scanner and no IP cameras.*
[7] *Server requirements can be stated only after the server has been implemented and after system testing results are known.*

Contact

Petra Kraft
Siemens Healthineers
DI SY M&S M
Siemensstr. 3
91301 Forchheim
Germany
+49 (174) 3144075
petra.kraft@siemens-healthineers.com


Petra Kraft


Janis Dummet

Meet Siemens Healthineers

Siemens Healthineers: Our brand name embodies the pioneering spirit and engineering expertise that is unique in the healthcare industry. The people working for Siemens Healthineers are totally committed to the company they work for, and are passionate about their technology. In this section we introduce you to colleagues from all over the world – people who put their hearts into what they do.

Hi there, my name is Stuart Calder

and I am an MRI applications specialist in Australia. I started my career over 30 years ago when I started studying diagnostic radiography in Edinburgh, Scotland. I graduated in 1991 and after almost four years of working in Edinburgh I went on an adventure to Australia, originally for a year – however 24 years later I'm still here! When I look back I think I was either crazy or brave to do such a thing. I don't think that I would have the nerve for such an adventure these days – having said that I haven't regretted my move. When you move country to work I think you make a real effort to be social and meet new people and as such it doesn't take long to create a group of friends and feel like home. Australia also didn't seem too foreign for a British person as the Queen is still on the money, they drive on the left side of the road, and they speak English.

Melbourne, Australia

How did you first come in contact with MRI?
Working as a radiographer in a private hospital in Melbourne gave me my first exposure to MR. Amazingly, when I left Scotland there were no clinical MRI machines – how times have changed. In 2000 I became an MRI Supervisor and in 2005 I became the MRI State Coordinator for the company I worked for. Over those years I worked on four different magnets across all vendors. I distinctly remember our double echo sequence for 19 transverse slices in the brain used to take 9:02 minutes and I also remember kneeling at the end of the scanner to manually tune the extremity coil before we could start scanning. The younger generation always laugh when I tell them such stories. In 2010 after 15 years of service at Epworth Hospital in Melbourne I felt I needed a change and hence started with Siemens.

What is most fascinating about your job?
I distinctly remember my first day with Siemens Australia. I was sent to Adelaide to shadow a colleague who was installing a MAGNETOM Trio. A staff member at this hospital asked how long I'd been with Siemens and I replied: „About 45 minutes". She laughed and said, „Excellent! It's my first day, too". Back then our MR applications team was very small, we had three applications specialists, a product specialist, and a marketing manager. Now, nine years later the success of the MR business in this region, its research possibilities, and the quality and support that Siemens offer speak for themselves. I find the main part of my role is to provide outstanding customer service. We get to ensure that the professionals we teach are well equipped and up-to-date on the use of their equipment. This ultimately filters down to the patient so they can have the best possible outcome with a high level of patient care.

Being an applications specialist has given me the opportunity to learn so much. Not only from the excellent courses we attend but also from a cross section of the radiographers we teach and the colleagues we get to work with. No two weeks are ever the same and most Mondays it feels like you're starting a new job with the fears of – what will the customers be like?; where should I park?; what are their expectations of me?; where's the toilet?; where's a good place for coffee?

What do you think are the most important developments in MRI and in healthcare?
MR is also far more accessible now than it was when I first started in MR. MRI used to only be available in major hospitals in major cities. People are living longer and with this aging population comes the need for more screening scans and therefore preventing diseases before they occur. Nowadays, even the smallest private practise often has an MR scanner and patients can now also have the convenience of not having to travel so far for an examination or wait so long for it. This of course has its own challenges as it gets more difficult to find experienced MRI radiographers to staff these scanners. Siemens have the ability

now however to utilize Siemens Remote Service (SRS) and provide assistance in real time. This again has been implemented since I started with Siemens – the Applications helpdesk in the Australia / New Zealand region is a full-time job which is shared between all of us.

The speed of MR development astounds me too. Again when I started we were on either *syngo* MR A or B software and worked on MAGNETOM Espree, Avanto, Trio, and Verio systems. Then along came *syngo* MR C, D, E software, *syngo*.via, and now *syngo* MR XA platforms. There's never a dull moment and with each software release R&D come up with better solutions for customer ease of use and the ability to scan more patients which ultimately leads to shorter waiting lists and a better outcome for the patient which is our main focus. SMS acceleration techniques are only just beginning. It's amazing how fast scanning is becoming maintaining excellent image quality.

Outside of work ...
Being an applications specialist is not just a job, it's a lifestyle. I have been able to see so much of Australia, New Zealand, China, and Europe working with Siemens. I think if I could have a month off I would still use it to travel. Travel is a passion of mine and always has been. Having said that priorities change and now that I'm partnered with 2 dogs I love staying at home. Perhaps with a month off we could hire a campervan and explore without heading to the airport!

Melbourne, Australia

I'm Emily Lucchese,

one of the MRI applications specialists in Australia. This February was my four-year anniversary with Siemens and I can't believe how quickly time has gone. I've learnt an incredible amount in this role – not only about MR physics and our *syngo* platforms, but about how best to teach individuals. Everyone learns differently and it's my job to teach the staff how to use the system to the best of its ability after I've gone – that's my aim at the end of handover applications. Finding the best way to do that can be challenging. I was exposed to a very passionate MRI mentor early on in my radiography career and I credit him for my love of the imaging modality. Not everyone is as lucky as I was, so educating people about MRI is something I love.

How did you first come in contact with MRI?
I began working in MRI in a private hospital in Melbourne on a very old GE scanner and then began working in a public hospital for less than a year, where I was introduced to Siemens' MAGNETOM Symphony and MAGNETOM Verio, before moving to a different private company and worked solely on Siemens scanners. I really loved where I worked and the people I worked with, but was looking for a challenge. When I heard about the job with Siemens at a Siemens user group meeting in Australia, it sounded like a great opportunity to meet new people, learn a lot, and travel the world – I was single and fairly free, so thought it was the perfect time for a change.

What is most fascinating about your job?
One of the best things about my job is the training that we receive at our headquarters in Erlangen, Germany. I've had many trips over and made friends with other MR application specialists all over the world. I've been able to learn from them how differently people around the world perform MRI and have shared different tips and tricks between us.

Being an applications specialist definitely comes with its challenges. Living in such a big country with a high number of magnets means that we spend a lot of time travelling. I've missed numerous family functions and birthdays over the last four years but thankfully, they still love me! Getting to know people for a short period and then moving on can be tough – I've become so fond of the customers I've come across and had such fun with them, it's sometimes hard to say goodbye.

What do you think are the most important developments in MRI?
Luckily, the good definitely outweighs the bad. I'm constantly learning new things about this job and MRI in general. The technology is growing so fast and it's exciting being a part of a company that is in the forefront of research and development. Compressed Sensing and its applications absolutely blows my mind. The quality we're able to achieve with images free of motion, even when the patient is breathing and then being able to achieve such fast temporal resolution is a game-changer. Not all patients are able to comply with our strict conditions and time constraints – acceleration techniques are now readily available to help with this, ensuring that all patients are able to receive the best care.

The entire editorial staff at University Hospital Heidelberg and at Siemens Healthineers extends their appreciation to all the radiation oncologists, radiologists, technologists, physicists, experts, and scholars who donate their time and energy – without payment – in order to share their expertise with the readers of MAGNETOM Flash and the MReadings.

MAGNETOM Flash – Imprint

Publisher:
Siemens Healthcare GmbH
Magnetic Resonance,
Karl-Schall-Str. 6, D-91052 Erlangen, Germany

Editor-in-chief:
Antje Hellwich
(antje.hellwich@siemens-healthineers.com)

Guest editor:
Professor Jürgen Debus, M.D., Ph.D.
Chairman Department of Radiation Oncology,
University Hospital Heidelberg, Germany

Editorial Board:
Rebecca Ramb, Ph.D.; Sunil Kumar S. L., Ph.D.;
Wellesley Were; Gary R. McNeal, MS (BME)

Review Board:
Elena Nioutsikou, Ph.D.; Matthias Drobnitzky, Ph.D.;
Daniel Fischer; Glen Roberts; Efrén Ojeda;

Copy Editing:
Sheila Regan, Jen Metcalf, UNIWORKS,
www.uni-works.org
(with special thanks to Kylie Martin)

Layout:
Agentur Baumgärtner,
Friedrichstr. 4, D-90762 Fürth, Germany

Production:
Norbert Moser,
Siemens Healthcare GmbH

Printer:
G. Peschke Druckerei GmbH,
Taxetstr. 4, D-85599 Parsdorf b. Munich, Germany

We welcome your questions and comments about the editorial content of MAGNETOM Flash. Please contact us at magnetomworld.team@siemens-healthineers.com

Manuscripts as well as suggestions, proposals and information are always welcome; they are carefully examined and submitted to the editorial board for attention. MAGNETOM Flash is not responsible for loss, damage, or any other injury to unsolicited manuscripts or other materials. We reserve the right to edit for clarity, accuracy, and space. Include your name, address, and phone number and send to the editors, address above.

MReadings: MR in RT is also available online:

www.siemens.com/magnetom-world-rt

Not for distribution in the US

On account of certain regional limitations of sales rights and service availability, we cannot guarantee that all products included in this brochure are available through the Siemens sales organization worldwide. Availability and packaging may vary by country and is subject to change without prior notice. Some/All of the features and products described herein may not be available in the United States.

The information in this document contains general technical descriptions of specifications and options as well as standard and optional features which do not always have to be present in individual cases, and which may not be commercially available in all countries.

Due to regulatory reasons their future availability cannot be guaranteed. Please contact your local Siemens organization for further details.

Siemens reserves the right to modify the design, packaging, specifications, and options described herein without prior notice. Please contact your local Siemens sales representative for the most current information.

Note: Any technical data contained in this document may vary within defined tolerances. Original images always lose a certain amount of detail when reproduced.

Siemens Healthineers Headquarters
Siemens Healthcare GmbH
Henkestr. 127
91052 Erlangen, Germany
Phone: +49 9131 84-0
siemens-healthineers.com

Published by Siemens Healthcare GmbH · Order No. A91MR-1100-100C-7600 · Printed in Germany · 7125 04191. ·

siemens.com/magnetom-world-rt